# Constant-Temperature Constant-Voltage Charging Method for Lithium-ion Battery Technology

by

Vinicius Albanas Marcis

A Thesis Submitted in Partial Fulfillment
of the Requirements for the Degree of
Masters of Applied Science

in

Faculty of Engineering and Applied Science

Department of Electrical, Computer, and Software Engineering

Ontario Institute of Technology (Ontario Tech University)
Oshawa, Ontario, Canada

September 2020

# Thesis Examination Information

Submitted by: **Vinicius Albanas Marcis**

| |
|---|
| Constant-Temperature Constant-Voltage Charging Method for Lithium-ion Battery Technology |

An oral defense of this thesis took place on August 28, 2020 in front of the following examining committee:

**Examining Committee**:

| | |
|---|---|
| Chair of Examining Committee | Dr. Ying Wang |
| Research Supervisor | Dr. Sheldon Williamson |
| Examining Committee Member | Dr. Vijay Sood |
| Thesis Examiner | Dr. Martin Agelin-Chaab |

The above committee determined that the thesis is acceptable in form and content and that a satisfactory knowledge of the field covered by the thesis was demonstrated by the candidate during an oral examination. A signed copy of the Certificate of Approval is available from the School of Graduate and Postdoctoral Studies.

# Abstract

Lithium-ion batteries are the Electrical Vehicles' (EVs) best choice of Energy Storage Systems (ESS) on account of their energy density, power density, and life cycle. In order for the EVs to compete with conventional vehicles, they need faster-charging methods to have equivalent refueling time. However, fast-charging can hamper the life cycle due to higher currents applied to the battery because of the Li-ion battery's uncontrolled temperature increase.

This thesis evaluates the Constant-Temperature and Constant-Voltage (CT-CV) charging methodology for three different Li-ion batteries over a temperature range of 0°C-50°C. Similarly, the conventional Constant-Current and Constant-Voltage (CC-CV) charging methodology is assessed for comparison. Moreover, a Battery Automated System (BAS) is developed to acquire the charging time, coulombic efficiency, and life cycle. Finally, a model capable of predicting the charging time, battery voltage, and surface temperature is described.

**Keywords**: Lithium-ion, Fast-Charging, Electrical Vehicles, Charging Methods.

# Acknowledgements

I would like to express my gratitude and thankfulness to my supervisor, Dr. Sheldon S. Williamson for his guidance and support throughout the course of this work. Without his encouragement to pursue graduate studies I would not find myself where I am today, and I am very thankful for that. Due to his continued pursuit for novel and relevant research work, I have been able to learn from him and be a part of the astounding Ontario Tech STEER group. I would like to thank him for the knowledge, perseverance, and leadership qualities that he has taught me in the time that I have been part of the team.

I would also like to thank my peers and friends in the STEER group and at Ontario Tech. Also, Dr. Jaya Sai Praneeth, who is a member of the STEER group and defended his PhD in 2019. I am thankful for his guidance in assisting me with support and knowledge to help me complete my work. To my peers and friends at Ontario Tech I would like to say thanks for helping me to make my time with the team one that I will never forget and will always cherish.

Finally, I would like to thank my family, whose support was essential for my perseverance throughout the decision to come to Canada to pursue my studies. Thank you very much.

# Author's Declaration

I hereby declare that this thesis consists of original work of which I have authored. This is a true copy of the thesis, including any required final revisions, as accepted by my examiners.

I authorize the University of Ontario Institute of Technology to lend this thesis to other institutions or individuals for the purpose of scholarly research. I further authorize University of Ontario Institute of Technology to reproduce this thesis by photocopying or by other means, in total or in part, at the request of other institutions or individuals for the purpose of scholarly research. I understand that my thesis will be made electronically available to the public.

_____ Vinicius Albanas Marcis

# Statement of Contributions

Part of the work described in Chapter 3 has been published as:

Marcis, Vinicius Albanas, et al. "Analysis of CT-CV Charging Technique for Lithium-ion and NCM 18650 Cells." 2020 IEEE International Conference on Power Electronics, Smart Grid and Renewable Energy (PESGRE2020). IEEE, 2020.

Marcis, Vinicius Albanas, et al. "Analysis of CT-CV Charging Technique for Lithium-ion and NCM 18650 Cells Over Temperature Range." 2020 IEEE International Conference on Industrial Technology (ICIT). IEEE, 2020.

I have performed the majority of analytical, simulation, and experimental tests, as well as the writing of the manuscripts.

# Summary

# List of Figures

# List of Tables

# Abbreviations and Symbols

| | |
|---|---|
| AC | Alternating Current. |
| Ah | Amper-hour [Ah]. |
| BAS | Battery Automated System. |
| BMS | Battery Management System. |
| BUT | Battery Under Test. |
| C | Capacitance [F]. |
| CC | Constant Current. |
| CC-CV | Constant-Current and Constant-Voltage. |
| CE | Coulombic Efficiency. |
| CEI | Cathode Electrolyte Interphase. |
| CO | Carbon Monoxide. |
| $CO_2$ | Carbon Dioxide. |
| CSV | Comma Separated Values. |
| CT | Constant Temperature. |
| CT-CV | Constant-Temperature and Constant-Voltage. |
| CV | Constant Voltage. |
| DAQ | Data Acquisition System. |
| DC | Direct Current. |
| DoD | Depth-of-Discharge. |
| ECM | Electric Circuit Model. |
| EDT | Electric Drive Train. |
| EIS | Electrochemical Impedance Spectroscopy. |
| EM | Electrical Machine. |
| EoC | End of Charge. |
| EoL | End of Life. |
| ESS | Energy Storage System. |
| EV | Electric Vehicle. |
| EVs | Electric Vehicles. |

| | |
|---|---|
| FEV | Full Electric Vehicle. |
| HEV | Hybrid Electric Vehicle. |
| Hz | Frequency [Hz]. |
| I | Current [A]. |
| $I_{bat}$ | Battery Current. |
| ICE | Internal Combustion Engine. |
| ILP | Integer Linear Programming. |
| IM | Induction Machine. |
| LCA | Life Cycle Assessment. |
| LEAM | Loss of Electrode Active Material. |
| LLI | Loss of Lithium Inventory. |
| LUT | Look Up Table. |
| MAE | Mean Absolute Error. |
| MSCC | Multi Stage Constant Current. |
| NCA | Nickel Cobalt Aluminum $LiNiCoAlO_2$. |
| NCM | Lithium Nickel Cobalt Manganese Oxide $LiNiCoMnO_2$. |
| OCV | Open Circuit Voltage. |
| PHEV | Plug-in Electric Vehicle. |
| PID | Proportional Integral Derivative. |
| PMSM | Permanent Magnetic Synchronous Machine. |
| R | Resistance [Ω]. |
| $R^2$ | Squarred Correlation Coefficient. |
| RMSE | Root Mean Square Error. |
| RPM | Revolution Per Minute. |
| SAE | Society of Automotive Engineers. |
| SCPI | Standard acronyms for Programmable Instruments. |
| SEI | Solid Electrolyte Interphase. |
| SoC | State-of-Charge. |
| SoH | State of Health. |
| SRC | Sinusoidal Ripple Current. |
| STEER | Smart Transportation Electrification and Energy Research. |
| $T_a$ | Ambient Temperature. |

| | |
|---|---|
| $T_s$ | Surface Temperature. |
| TC | Trickle Charging. |
| TTW | Tank-to-Wheel. |
| USB | Universal Serial Bus. |
| V | Voltage [V]. |
| $V_{bat}$ | Battery Voltage. |
| VCD | Varying Current Decay. |
| WTT | Well-to-Tank. |
| WTW | Well-to-Wheel. |

# Chapter 1

# Introduction

This chapter begins with a brief history of Electric Vehicles (EVs), followed by their environmental impact. Subsequently, different types of EVs are presented, with their different topologies and main components. A detailed explanation of the battery pack is presented, with attention to Battery Management System (BMS), battery cell, battery aging, and cell chemistry. Finally, a literature review on charging methods is presented as well as a summary of charging methods, and the scope and objectives of this thesis are defined.

## 1.1 Brief History

The history of EVs traces back to the 19th century. From 1890 to 1929, the Electric Vehicle (EV) fleet was higher than Internal Combustion Engine (ICE) vehicles and steam-powered vehicles [8]. In the 1900s, the advantages of steam-powered vehicles were low. However, their disadvantages were long engine start-up duration and recurrent refueling. Steam-powered vehicles functioned based on the principle of pressurized water vapor supplying power to the wheels. On the other hand, fuel-

powered cars were becoming mainstream with superior speed and travel range above all their competitors. However, their higher price, challenging start-up process, and smog produced during operation kept costumers away from ICE technology. The transportation best option was EV, which was silent and cleaner. However, they were expensive due to the battery pack cost.

ICE vehicles started to be adopted by the general public after the invention of the electric start-up device, which reduced the car turn-on time. This device replaced the need for the hand crank operation, which was time-consuming and inefficient. Furthermore, there was a need for extended range and higher speed. Thus, the acceptance for ICE cars increased because of this new technology, leading the research and development towards combustion engines.

Over the past 100 years, ICE vehicles have dominated the automotive sector. They left the legacy of culture, reliability, robustness, and elegance. However, ICE technology hurts the environment, with Carbon Monoxide (CO) pollution and greenhouse gases increasing the earth's average temperature. For this reason, nowadays ICE vehicles need to be replaced by EVs to reduce greenhouse gases and help control the effects of global warming.

## 1.2 Environmental Background

The emissions produced by vehicles are measured using Life Cycle Assessment (LCA), where the energy consumption and Carbon Dioxide ($CO_2$) emissions of a specific region are analyzed. LCA measures the fuel-chain, from production to consumption, in a method called Well-to-Wheel (WTW). This method has two parts: one examines the fuel generation, and the second analyzes fuel consumption.

Well-to-Tank (WTT) analyzes energy consumption and $CO_2$ emission to produce

energy for the car. The region's energy mix is important, where renewable sources (i.e., hydro, solar, wind, and geothermal) reduce the WTT index. Nonetheless, fossil fuel sources (i.e., black coal, brown coal, natural gas, and oil) will increase the WTT index. For example, in an ideal scenario, the energy mix should be 100% from renewable energy resulting in zero $CO_2$ generation, and WTT index equaling to zero [9] [10] [10] [11].

Tank-to-Wheel (TTW) analyzes the environmental impact of the vehicles to deliver power to the wheels. The ICE engine uses fossil fuel (gasoline, diesel, and methanol), and the energy conversion is inefficient and ranges from 20% to 35% [9] [12]. Meanwhile, the EV energy conversion efficiency ranges between 71% to 89% [13], and there is no emission of $CO_2$ to the atmosphere.

Consequently, the introduction of EVs is important to reduce global warming and greenhouse gases. Therefore, many EVs are under development or are already deployed to the roads with different configurations, like Hybrid Electric Vehicle (HEV), Plug-in Electric Vehicle (PHEV), and Full Electric Vehicle (FEV).

## 1.3 Electric Vehicles Configurations

The public has become self-aware of the benefits of EV in their daily lives. The general public sees the environment and economy as the main factors to choose an EV [9]. The main advantages of EV over ICE vehicles are economy, comfort, the environment, fuel independence, and efficiency [9]. However, the main disadvantages are in autonomy, infrastructure, and cost [9]. Autonomy is one of the main factors that drive people away from EV, due to lower distances traveled on a single charge than in conventional vehicles. Also, the charging time is another barrier to the EV introduction to the market. The charging times vary from 20 minutes with fast

chargers up to 17 hours with slow charge [14]. Therefore, these factors combined result in major drawbacks for EV customers.

Research and development are introducing new infrastructure topologies, new charging stations, new traveling, and refueling cultures. New topologies of EV configuration came along to overcome these disadvantages. There are three main topologies employed in the EV: HEV, PHEV and FEV.

### 1.3.1 Hybrid Electric Vehicles

HEV combine the advantages of the two different power sources to overcome the disadvantages of ICE vehicles. The existence of an Electrical Machine (EM) and a battery pack makes HEV more fuel-efficient while having a good performance due to the electrical systems being more efficient than the mechanical systems. Also, the HEV integrates regenerative braking to the system, where mechanical energy is converted to electricity while the car is braking. Furthermore, the HEV is charged solely by the ICE or regenerative braking; thus, it cannot charge through external sources. For instance, the electrical system added to the ICE drivetrain can improve the range up to 1200km [15] with one single tank.

The hybridization ratio represents the power share between ICE and EM. A high hybridization index means a more powerful electric system and modest ICE. On the other hand, a low hybridization ratio results in a less powerful electric system and a more comprehensive ICE. The way these power sources are combined will result in a trade-off of efficiency, cost, and control complexity. Series and parallel combination of ICE and electric systems are the two main topologies in the HEV. These topologies also contain other power train elements, like gearbox, clutch, power electronics, communication systems, etc.

The series conversion has the advantage of being able to turn-off the ICE. An HEV

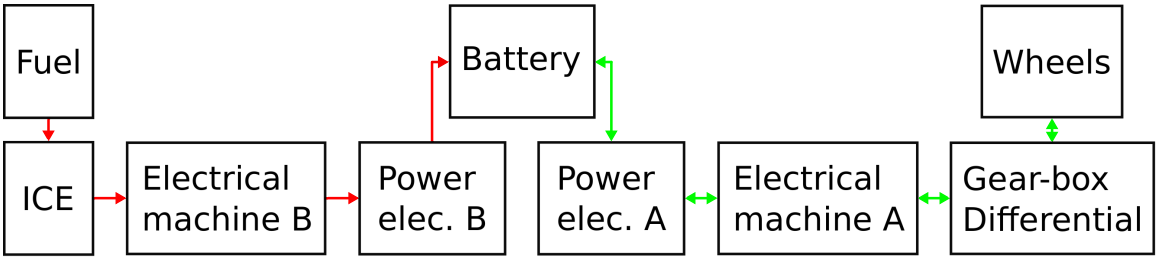


Figure 1.1: HEV series configuration.

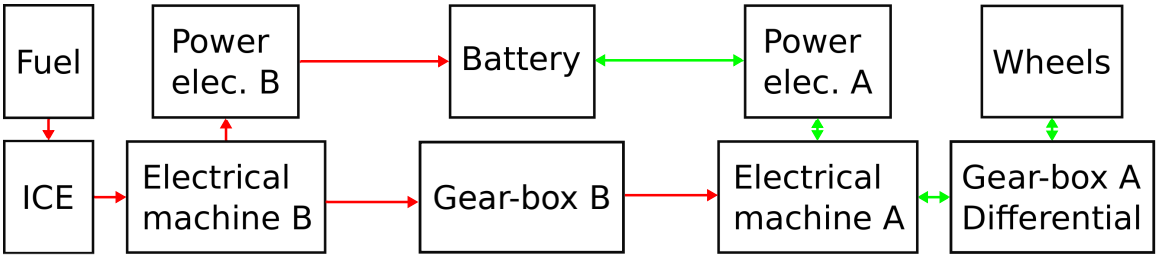


Figure 1.2: HEV parallel configuration.

with series topology diagram is shown in Figure 1.1. With the series topology, only the EM A (i.e., traction machine) provides power to the wheels. The ICE is used to charge the battery through EM B (i.e., charge machine). The battery has two interfaces to connect two different power electronics devices. First, a unidirectional device controls the charging flow from the ICE to the battery, and it has to maintain the maximum efficiency of the ICE. Second, a bidirectional device controls the power flow for the traction machine and the regenerative braking. Finally, the traction gearbox provides the necessary conversion from the traction machine to the wheels.

The series topology can have the traction machine assembly in another location from the charging machine and the ICE. This characteristic makes the car assembly easier and provides a lower floor [16], maintaining the car structure similar to the conventional ICE vehicles. However, this topology presents lower efficiency than other HEV topologies due to the number of energy conversions needed from ICE to the wheel.

The parallel topology has the advantage of providing power to the wheels from

ICE and EM at the same time. A HEV parallel topology is shown in Figure 1.2. Also, it is possible to have electric or ICE operation solely. This range of configurations results in higher efficiency than series configuration. It also provides the powertrain multiple choices for the best efficiency or performance depending on the drive cycle. However, the parallel topology's complexity is higher than the series topology due to the different user-cases.

The series and parallel topologies are the base for other high complexity HEV configurations, which apply clutches, planetary gearboxes, CVT, ISG [16]. The operation takes place in a series and parallel, with automatic algorithms intended for best performance and efficiency. The topology in which the traction power path is longer (i.e., with more elements) will be less efficient. For instance, a series configuration has five transformation elements; thus, it provides a worse efficiency than parallel topology.

Consequently, the main complexity of these mixed components topologies is the trade-off between performance and efficiency. The control strategy's design focuses on maintaining each power source's best overall performance for a determined situation. For example, the efficiency of ICE during start-up is known to be very low; thus, the electric machines are used during start-up and acceleration periods, and the ICE are used during cruising and constant speed situations [15].

Even though the battery pack is not significant, it is the most sensitive component of the HEV. The battery maintains 40%-60% SoC range [15] to extend battery life; and to have room for regenerative braking. Thus, as the battery charges/discharges with peak power frequently, it results in the battery pack degradation and life cycle reduction. In the parallel topology, the battery can be unemployed, since the traction power can flow directly from ICE to the wheels. However, it accepts regenerative breaking. As a result, the battery must take into consideration the performance and

its State of Health (SoH).

### 1.3.2 Plug-in Hybrid Electric Vehicles

Plug-in hybrid vehicles are the next generation of HEV, and they have higher capacity batteries. They have an on-board charger making them capable of charging from a connection with the AC mains or an external charger. With these new characteristics, the PHEV has become more independent of the ICE, thus having a higher hybridization ratio, which provides a longer Electric Drive Train (EDT) range. PHEV topologies follow the HEV, with series, parallel, and mixed topologies. However, due to higher battery pack capacity, the electric propulsion is used more often than in HEV cars resulting in a more efficient and environmentally friendly operation.

The difference in batteries pack sizes are significant between PHEV and HEV. Depth-of-Discharge (DoD) is the measurement of how much capacity is drained from the battery pack. HEV has DoD range from 10 to 20% [15], and this low DoD range enhances the battery life; yet, it is more ICE dependent. On the other hand, PHEV can handle up to 80% of DoD [15], considerably reducing the life cycle of the battery pack. However, larger DoD range reduces the dependency on ICE. Thus, the design of the battery bank must account for these extended DoD ranges.

Furthermore, PHEVs can charge the batteries from residential AC outlets or external charger, which results in fewer CO2 emissions. Usually, the on-board chargers installed are Society of Automotive Engineers (SAE) level one chargers [17]. For example, the average charging time of PHEV is 4:30h [17]. The battery pack capacity of conventional PHEV in the market are: Ford Escape (PHEV) has a battery pack of 10kWh [17], Volvo V70 PHEV has a battery pack of 11kWh, and Toyota Prius PHEV has a 5.2kWh battery pack [17].

### 1.3.3 Full Electric Vehicles

The FEV has a simpler and more efficient configuration than HEV and PHEV in the market. The main reason is the absence of ICE, which is the least efficient engine in these hybrid topologies. Also, they are the elements that produce greenhouse gases that harm the environment. Thus, because they have only an EM to power the car, the emissions are generated only in the electricity generation plants, where pollution is dependent on the energy mix of the region, as seen in Chapter 1.2. Another considerable difference is the battery's size, where FEV are equipped with higher capacity batteries packs to enable longer travel distances. Also, they have an on-board charger, which might be compatible with fast charging technologies. Therefore, the FEV powertrain is composed only by an electrical system that has to be reliable, safe, and provide performance simultaneously. The mechanical system provides the conversion necessary from the EM to the wheels.

The FEV powertrain is composed of a battery pack, a power converter, an EM, a gear box and a differential [7], as shown in Figure 1.3.

## 1.4 Full Electric Vehicles Main Components

The FEV topology is simple, robust, and efficient. Figure 1.3 shows its main components. The series connection provides a bidirectional energy flow, depending on the throttle and brake user inputs.

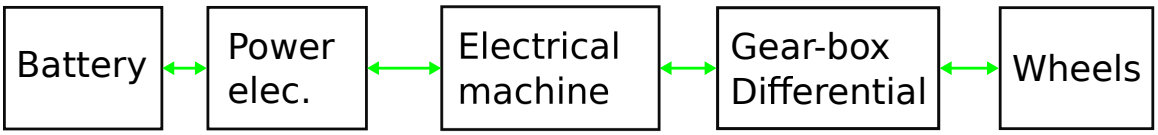


Figure 1.3: FEV configuration.

### 1.4.1 Electrical Machine

Electrical Machines transform AC or DC power into rotational energy. DC machines offer easier control and simpler converter topologies [7]. However, DC machines require additional elements like commuting poles and compensation windings, increasing their size and weight [7]. Moreover, their brushes and commutator need maintenance, decreasing overall EV life cycle, reducing efficiency, and increasing internal temperature; thus, complex cooling systems would be necessary.

The other option is AC machines with mainly two types: Induction Machine (IM) and Permanent Magnetic Synchronous Machine (PMSM). IM machines are well known for their low price, reliability, and efficiency compared to DC machines. IM efficiency is lower than PMSM machines due to the magnetization current and copper losses in the rotor at nominal speed, which results in heat generation, limiting its stable operating range [7]. The air gap has to be very small to reduce magnetization currents, thus adding fabrication costs due to very low tolerances needed to reduce this air gap.

The PMSM is used to increase efficiency and reduce the volume of the EM. Since the rotor has a fixed permanent magnet, there is no excitation current, which allows higher energy densities and efficiency over IM. However, as the magnetic material comes from natural resources, like NdFeB, it is expensive and is limited by natural resources. Additionally, PMSM efficiency is very high at nominal speeds. However, the PMSM use outside of the designed range leads to an efficiency drop and demagnetization of the machine.

Table 1.1 compares the power density and efficiency from three different motors, with an average power of 30 kW. It is evident the high performance of PMSM, with a power density of 6.1 kW/L and 97% efficiency; thus, many automakers are moving for EVs design with PMSM [7].

Table 1.1: Comparison between electrical machines (DC, IM and PMSM [7]).

| | DC | IM | PMSM |
|---|---|---|---|
| Power [kW] | 30.72 | 30.25 | 29.89 |
| Power Density [kW/L] | 1.6 | 2.5 | 6.1 |
| Volume [L] | 19.2 | 12.1 | 4.9 |
| Efficiency | 84% | 89% | 97% |

### 1.4.2 Power Electronics

The AC EM interfaces with the battery through a power electronic device (i.e., 3 phase inverter), which transforms the Direct Current (DC) Voltage [V] (V) of the battery to three-phase Alternating Current (AC). These inverters utilize solid-state devices, capacitors, and inductors that are prone to switching and conduction losses. Hence, the reduction of these losses is essential to improve the overall inverter efficiency and reduce the inverter's size.

The inverter uses a closed-loop control scheme to transfer power from the battery to the EM accordingly. The user's input via throttle pedal displacement is measured, and a resulting electrical signal is delivered to the motor controller to provide power from the battery to the motor. Moreover, the inverter has to be bidirectional for regenerative braking so that the energy can flow from the EM back to the battery safely.

### 1.4.3 Gear/Differential

As the EM have high efficiency in low, medium, and high Revolution Per Minute (RPM), only one gear is needed, which is different from ICE that requires multiple gears to operate in the narrow high-efficiency RPM window of the engine. This advantage considerably reduces the gearbox weight and volume. There are gearboxes with two gears, like the new electric Taycan from Porsche, which add travel range,

top speed, and complexity. Additionally to the powertrain, the gearbox connects to the differential, allowing different speeds at the left and the right wheels [18].

### 1.4.4 Battery Pack

The battery is used as Energy Storage System (ESS) in FEV. Multiple battery cells are connected in series and parallel to form a battery pack [19] to achieve higher capacities, current rating, and voltages. In series connection, the battery voltage ($V_s$) and the energy stored ($E_s$) are summed, while the capacity ($Cap_s$) is kept constant, as shown in equations 1.1 to 1.3. Meanwhile, the parallel connection keeps the battery voltage constant, adding the energy stored and capacity, as shown in equations 1.4 to 1.6. Therefore, by building series strings and connecting multiple strings in parallel, it is possible to design the battery pack accordingly to the application specifications. Usually the nomenclature is given by "**n**s**m**p" where **n** represents the number of cells in the series string, and **m** represents the number of strings connected in parallel. For example, Tesla Model S has 96s74p configuration, which represents 96 series connections, and 74 strings connected in parallel. These results in a battery pack terminal voltage around 403.2 V (considering single cell voltage of 4.2 V) [20]. Equations 1.1 to 1.6 are used to calculate the capacity, voltage, current and energy when working with cell batteries series and parallel connections.

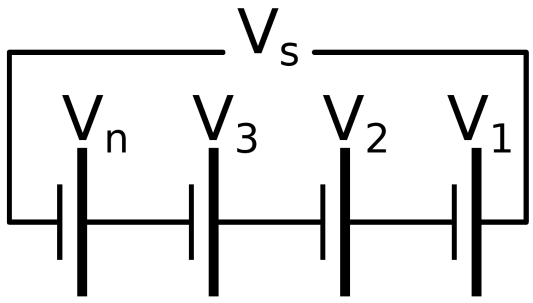


Figure 1.4: Series string connection.

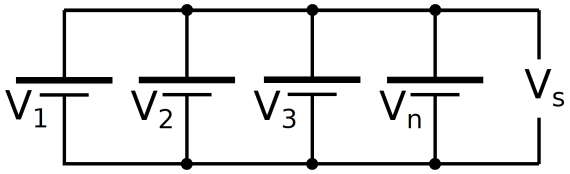


Figure 1.5: Parallel string connection.

$$Cap_s = Cap_n \tag{1.1}$$

$$V_s = V_1 + V_2 + ... + V_n \tag{1.2}$$

$$E_s = E_1 + E_2 + ... + E_n \tag{1.3}$$

$$Cap_s = Cap_1 + Cap_2 + ... + Cap_n \tag{1.4}$$

$$V_s = V_1 = V_2 = V_n \tag{1.5}$$

$$E_s = E_1 + E_2 + ... + E_n \tag{1.6}$$

Different battery voltages will result in different inverter circuit design, losses, and heat sinks. Thus, most of the battery packs applied in EVs have voltages in the range of 250 V to 450 V [7] for commercial cars. For example, Tesla Model S has 400 V battery packs [7], Nissan Leaf uses 360 V [7], Toyota iQ EV uses 277.5 V [7].

### Battery Management System

The BMS is used to maintain the battery cells in a series string under manufacturing specification. Even though the battery cells may come from the same manufacturing and have the same batch, they are not 100% equal, where differences in voltage and capacities due to manufacturing can be present. Also, aging is not equal among cells; different locations along the battery pack assembly [1] have different temperature distribution, resulting in further life degradation within the battery pack. One example of BMS application is: cell A has a slightly different capacitance and will reach the end of discharge faster than cell B. Therefore, the BMS will discharge cell B to keep both cells at the same SoC.

The BMS is the battery pack's monitoring system, and it is capable of taking voltage, Current [A] (I), and temperature measurements of individual cells or regions of the battery pack. Furthermore, in some cases, it can balance the cells either by passive balancing or by active balancing. Passive balancing discharges the over-charged cells using a resistive element. On the other hand, active-balancing regenerates the energy by transferring the over-charged cell energy to the weak li-ion cell. The BMS is also used to handle the battery thermal management for either protection or optimum battery operation temperature.

### Battery Pack at Cell Level

A battery cell comprises a positive electrode, a negative electrode, separator, electrolyte, and terminals. The electrodes are called anode and cathode. Depending on the battery operating mode, charge or discharge, they change the sign from positive to negative. For example, during the battery's discharge, the negative electrode is the anode, where the oxidation occurs, releasing electrons to flow to the cathode. On the contrary, during charge, the negative electrode is the cathode, where the oxida-

tion happens, releasing electrons to flow to the positive electrode, the anode in this charging mode [1]. For convention, the positive electrode will be called cathode, and the negative electrode will be called anode.

A metallic film composes the cathode, and the anode is formed of a carbon structure. A separator electrically isolates the electrodes, and they are immersed in the electrolyte. The electrolyte is composed of lithium salt and organic solvents [1]. Figure 1.6 shows the representation of a lithium-ion cell battery structure, with electrons (e-) and ions (Li+) moving accordingly with charge and discharge.

The transfer of electrons and ions happens in a diffusion process. It is a slow process due to the finite number of galleries in the electrodes [1], limiting the spaces available for the ion intercalation with the electron in the electrode. Figure 1.7 shows the charge transfer process during charge and discharge. During charge, the de-intercalation happens at the cathode, where the lithium releases one electron. The lithium is then transported through the Cathode Electrolyte Interphase (CEI), where it becomes solvated by the electrolyte solvents and transported in the anode's

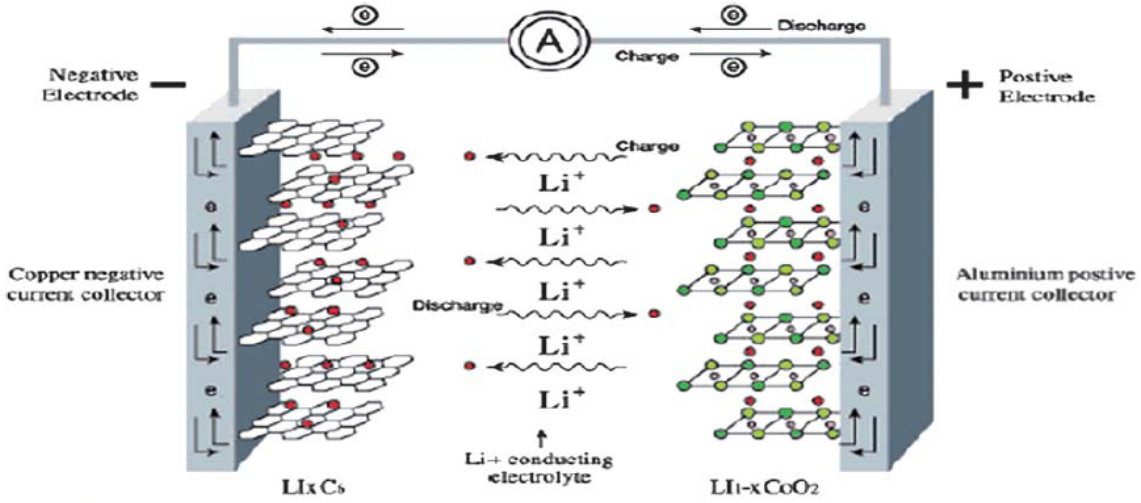


Figure 1.6: Lithium-ion cell battery structure and electrochemical processes [1].

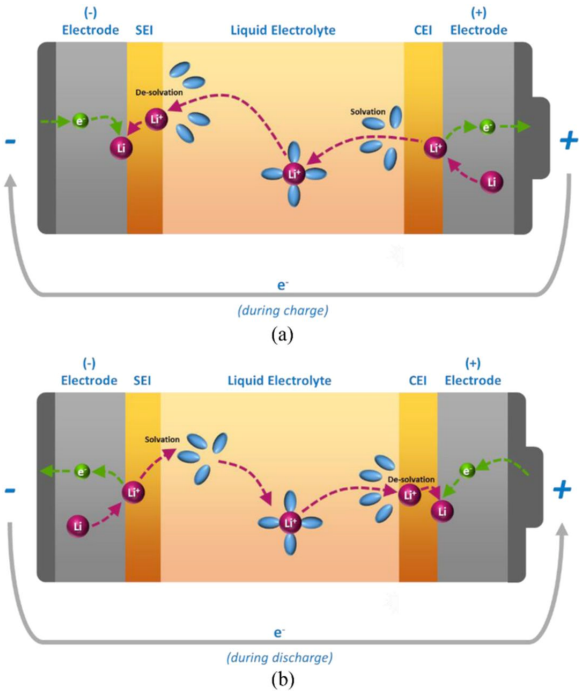


Figure 1.7: Lithium-ion and electron diffusion process [2].

direction. Before intercalation with the anode, the solvated lithium-ion goes through the Solid Electrolyte Interphase (SEI) layer where it is dissolved. The lithium-ion is ready to retake the electron at the anode and intercalate with the carbon structure.

### Battery Aging

The aging of lithium-ion cells is related with Loss of Lithium Inventory (LLI) and Loss of Electrode Active Material (LEAM) [21]. LLI occurs because parasitic reaction consumes cyclable lithium, where SEI layer consumes active material during the first cycles to be built. However, it also consumes lithium whenever the SEI layer is damaged throughout its life. Also, lithium platting consumes active lithium, which is plated to the negative electrode when there is an excess of lithium to be intercalated to the electrode. The SEI layer growth and lithium plating are the two main phenomena that reduce the cycle and calendar life of a battery. Moreover, SEI layer growth is

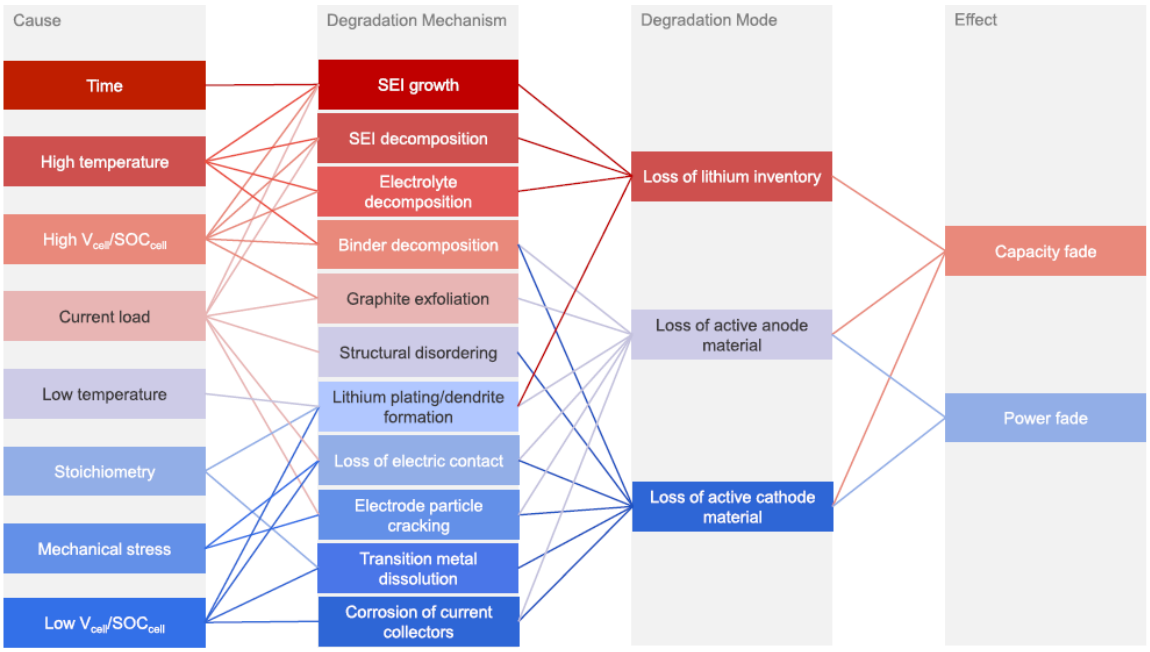


Figure 1.8: Most important tradeoffs in the battery chemistry [3].

more susceptible to happen above 25°C and lithium plating is prone to happen with temperatures below 25°C [22].

Figure 1.8 depicts a cause-effect study showing the degradation mechanism leading to capacity fade and power fade. Capacity fade happens due to the loss of active materials and lithium inventory, so lithium's quantity to cycle is lower than before; thus, the capacity is lower [4]. Nevertheless, the power fade is related to internal resistance growth, SEI layer growth, and lithium plating [4]. Additionally, the intercalation is a diffusion process, where the ions need to find a gallery in the electrode to intercalate with an electron. The higher currents will lead to more ions to be intercalated in the queue, increasing the electrode potential, which causes the lithium to plate at the electrode surface. The electrode's surface area is reduced with this lithium plated, increasing the resistance, and losing lithium inventory [22]. It is essential to mention that the lithium plating may be reversible during the discharge, reallocating the lithium back to the electrolyte and the cathode [22].

The diffusion process is dependent on the battery temperature of operation, and it can be calculated by the Arrhenius law as shown in Equation 1.7.

$$D = D_r e^{(E_a/R(1/T_r\ -1/T))} \tag{1.7}$$

D is the diffusion transfer energy, $D_r$ is the diffusion transfer energy referenced at the reference temperature ($T_r$), R is the universal gas constant, T is the battery temperature, and $E_a$ is the activation energy. Thus, by lowering the battery temperature, the diffusion transfer energy goes higher, resulting in higher potential on the electrode due to a long queue of ions to be intercalated. With this analysis, the lithium plating tends to happen at lower temperatures, reducing the battery life with an exponential trend [22]. However, at higher temperatures, the SEI layer growth is the leading degradation factor and happens into a square-root trend [22]. As the lithium plating occurs throughout the battery cell life, the aging mechanisms move from SEI layer growth to lithium plating. Thus, as the aging mechanisms are related to temperature, there is an optimal operating temperature for the cell where the lithium plating does not occur and the SEI growth is minimum.

### Cell chemistry

Nowadays, various chemistry types exist with different cathode and anode materials, which provides different trade-off to be considered accordingly with the application, as shown in Figure 1.9.

Safety factors have higher priority for EV application, where any issue may harm human life and may draw the public opinion very badly regarding EVs. For example, if any cell goes in thermal-runaway, it may propagate to the next cell and so on, resulting in a catastrophe fire. Thus, the entire battery pack design, with BMS,

casing, cooling system, and monitoring, should account first for safety.

Since the battery pack cost is very high, the life span may come as the second main priority [23]. The lifespan of a battery can be measured in two terms, the cycle life and calendar life. The cycle life estimates how many cycles the batteries have to undergo before reaching 80% of its initial capacity, thus reaching its End of Life (EoL) [24] [25]. The calendar life predicts the battery life accordingly with time. Most battery packs are designed to last ten years, but this depends on storage temperature and stored SoC [26].

The battery specific energy is limiting the driving range today. It is around 170 Wh/kg, where only part of this energy is considered usable energy since there are limitations on the lower and higher end of SoC [26]. Also, the specific power is the measurement of the amount of power the battery can deliver per kilogram (W/kg). This factor is not an issue for battery technology today. These factors are

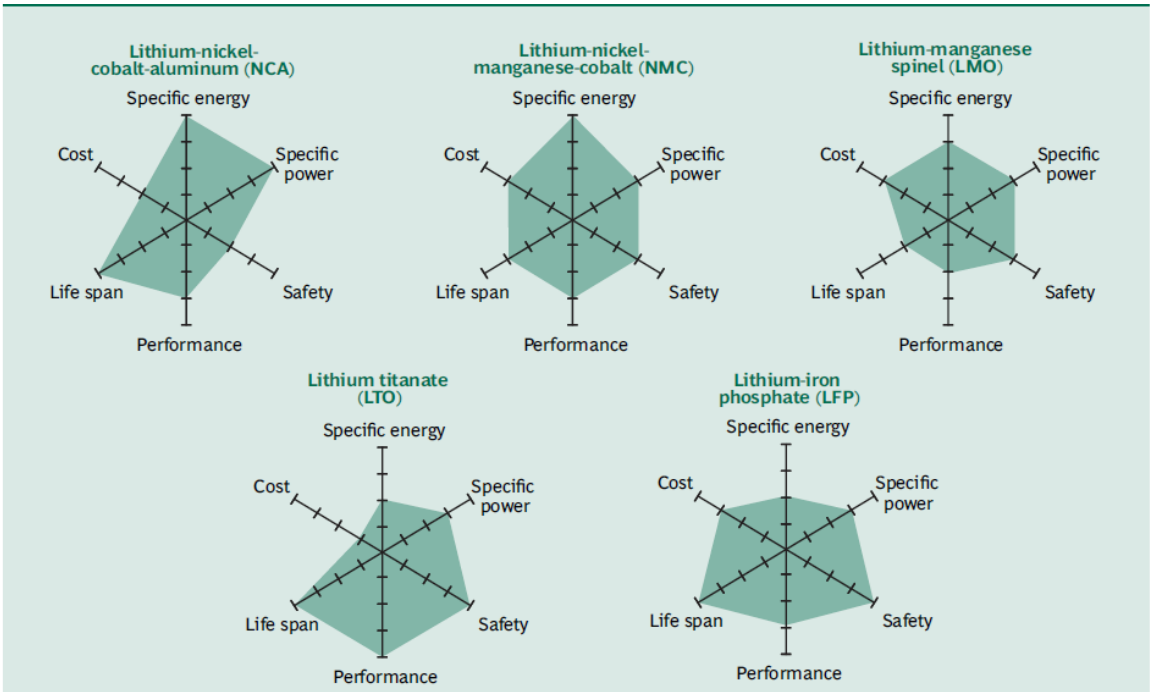


Figure 1.9: Degradation mechanisms linked to capacity fade and power fade [4].

dependent on temperature, SoH and define the overall performance of the battery, which has much to improve in terms of specific energy, specific power at lower and higher temperatures, and to maintain its characteristics during its entire life span.

The solution of all these factors is under constant development by universities and manufacturers. However, when all these factors are analyzed, it becomes evident that the battery cost increases, which is already one of the most expensive components of an EV. Thus, all this effort must be addressed, and the manufacturing of the battery packs must be accessible and cost-effective.

### 1.4.5 Conclusion

The ESS is a key element for any EV technology today, and batteries are the most popular and affordable technology for this purpose; thus, it is evident that the effort of producing better battery products is needed. The different specifications of EV bring a wide range of battery operations, while the battery life cycle and performance must be excellent. The charging techniques play a major role in maintaining the SoH of the battery, with voltage, current, and temperature controls as the main factors to be considered. Therefore, the charging techniques are constantly evolving to provide the battery with the best charge profile for the specific battery pack characteristics.

## 1.5 Literature Review

After reviewing the EVs in detail from history, environmental background, construction, and main elements, the importance of the battery pack remains evident. Even though the EVs have multiple well-established components in the powertrain, the battery pack is the most sensitive one. It is under development to overcome the two main drawbacks: life cycle and charging time.

An optimal charging method is needed to increase the life cycle and reduce the charging time. There is a trade-off between charging time and life cycle, where the higher charging currents lead to higher life degradation [26]. Furthermore, the temperature plays a significant role, as seen in Chapter 1.4.4, where there is an optimal operating temperature to avoid lithium plating and have minimum SEI layer growth [27]- [28].

Hence, a literature review on the charging techniques is presented, with details on how they are implemented, with details on life cycle degradation, charging current, and cell temperature.

### 1.5.1 Constant-Current Constant-Voltage Charging Method

The most common charging technique is the CC-CV method. This method offers great flexibility on charging specifications, with a straightforward algorithm and easy implementation. However, this charging method is conservative, which reduces overall charging speed [29].

CC-CV charging method is used in most scientific work as a benchmark for life cycle and charging efficiency evaluations. It is also used to compare charging time from other charging techniques due to its simplistic nature and reliability. Furthermore, the manufacturer datasheet is based on this charging technique, where maximum charging current, maximum and minimum voltages, and temperature boundaries are specified.

The beginning of the charging profile starts with a Constant Current (CC) phase, in which the current is limited accordingly and the battery reaches the cut-off voltage ($V_{cut-off}$), typically 4.2 V. Then, the charging profile transfers to the CV phase, where the voltage is limited to $V_{cut-off}$ and the current drops until it reaches the cut-off current ($I_{cut-off}$) [29] [30]. The CC-CV has three main protection modes.

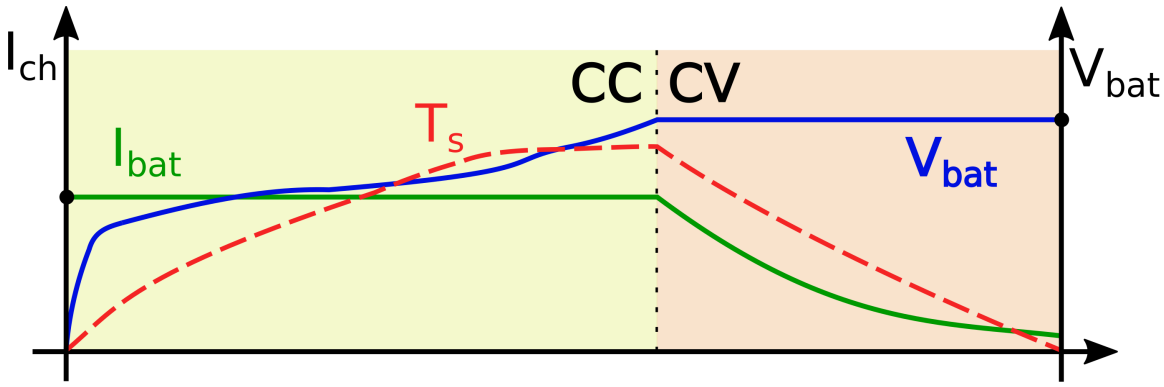


Figure 1.10: Characteristic curve for CC-CV charger.

First, it measures the battery pack temperature $T_{bat}$ and compares the temperature to lower and upper temperature limits. Second, it measures the initial $V_{bat}$ to check for over-charge, and third, it checks $V_{bat}$ to detect under-charge. If an under-charge is present, it will enable a Trickle Charging (TC), which charges at a rate equal to the self-discharge of the cell. Once the minimum $V_{bat}$ is reached, the CC phase can start [29] [30]. Figure 1.11 is a flowchart representation of this charging technique. Also, Figure 1.10 shows the I-V characteristic curve vs time of a CC-CV charge from 0% to 100% SoC.

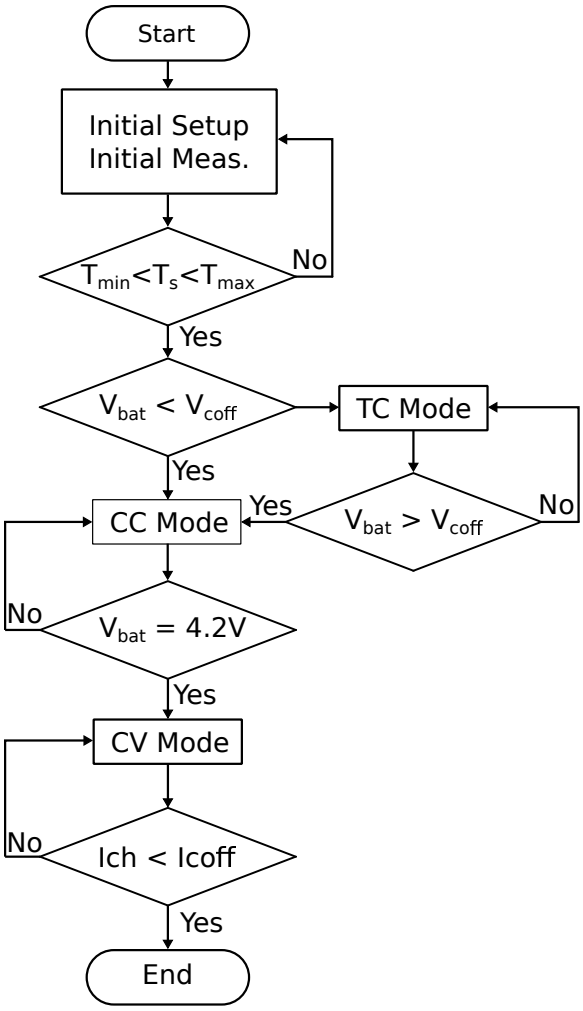


Figure 1.11: CC-CV charger flowchart.

### 1.5.2 Multi Stage Constant-Current Charging Method

The Multi Stage Constant Current (MSCC) charging method is based on CC-CV charging method. However, it replaces the CV phase by a multistage current steps, thus achieving a higher average charging current. Figure 1.12 shows the voltage and current profiles of MSCC charging method. This method starts with a CC stage $I_{bat}$, and once $V_{cut-off}$ is reached, $S_1$ begins. The charging current is reduced resulting in a voltage drop, as charging continues $V_{bat}$ increases while charging current

remains constant at the new set point until $V_{cut-off}$ is reached. This technique is implemented for the remaining stages until $V_{cut-off}$ is reached with the respective $I_{cut-off}$ as determined by the battery limitations [31]- [32].

The challenging part of this charging method is how to choose the adequate current drop for each stage and the number of stages. Further analysis is found in the literature. First, the fuzzy logic controller is implemented. It uses current, voltage, and temperature as input for the controller to decide the current amplitude for each step, resulting in faster charging time with a lower temperature rise compared to CC-CV [31]. Second, the Taguchi method is implemented and tested, which uses charging time, charge efficiency, and charging current to perform the cost function and acquire the optimal charging profile, reducing the charge time and reducing cell temperature [31]. Third is MSCC implementation Integer Linear Programming (ILP), where it uses different currents at each SoC subdivision (0-10%, 10-20%, etc) accordingly with charging efficiency. The proposed study has shown charge time improvement up to 21% [32].

Figure 1.12 shows the characteristic curve I-V curve vs time of a MSCC. Figure 1.13 shows the basic flowchart for MSCC charging methods.

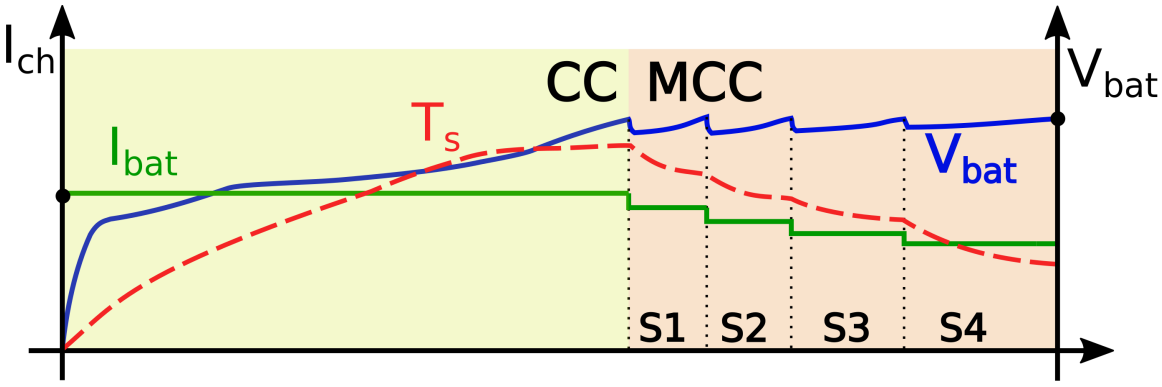


Figure 1.12: I-V curve characteristic of MSCC charging method.

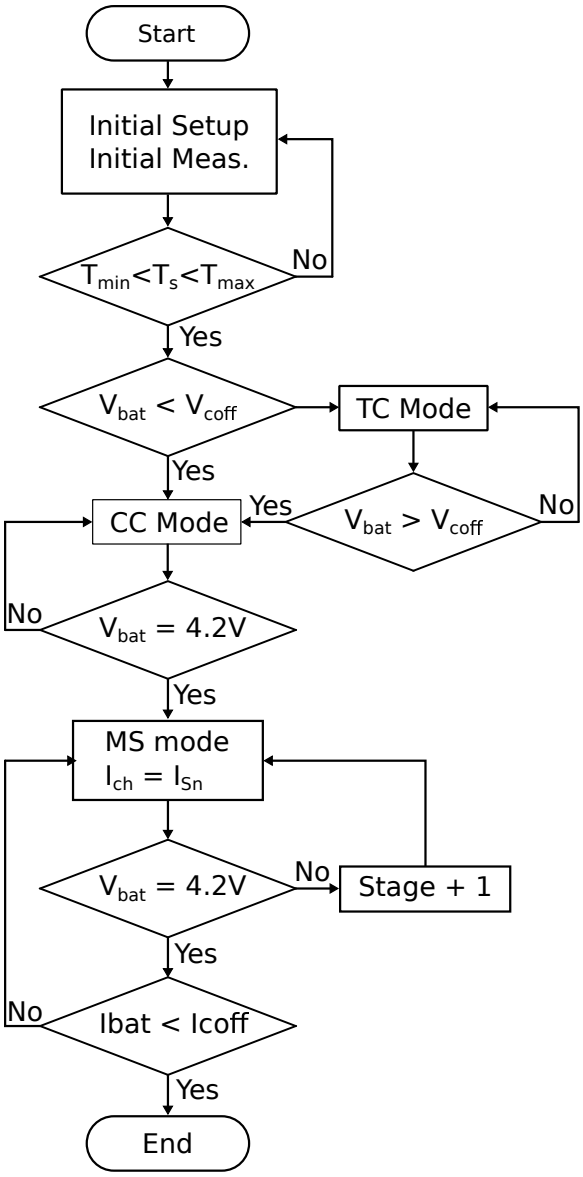


Figure 1.13: MSCC charger flowchart.

### 1.5.3 Boost Charging Method

The boost charging method uses a high current at the beginning of charging, followed by a standard CC phase, and finally, a CV phase. Due to the high current at the beginning of charging, this method is tended to reduce charge time, with low computational effort. Therefore, as lithium plating tends to occur with the higher current

on fast charging techniques [4] [33], this boost charging technique avoids the lithium plating to occur by limiting the fast charge only for a limited time at the beginning of charge.

The boost charging method was implemented by [34], where a lithium polymer cell was studied, and cycle analysis was performed. It introduces three stages: first, the boost charging stage, as shown in Figure 1.14, where the first stage current is 4C. Second, the constant current, and finally the CV stage. The first stage ends when the battery voltage reaches $V_{cut-off}$ 3.6 V; the second stage reduces the current, and the battery voltage drops. Once the battery voltage reaches $V_{cut-off}$ again, the CV starts. This method enhances charging time by approximately 70% when compared to CC-CV [34], and also maintained 4500 full cycles with capacity retention above 80% [34]. In contrast, another study shows higher life cycle degradation when compared to CC-CV [30]. Thus, it is well defined if a boost charge can maintain a good life cycle and fast charge.

Figure 1.14 shows the characteristic curve I-V curve vs time of a boost charger. Figure 1.15 shows the basic flowchart for boost charger charging methods.

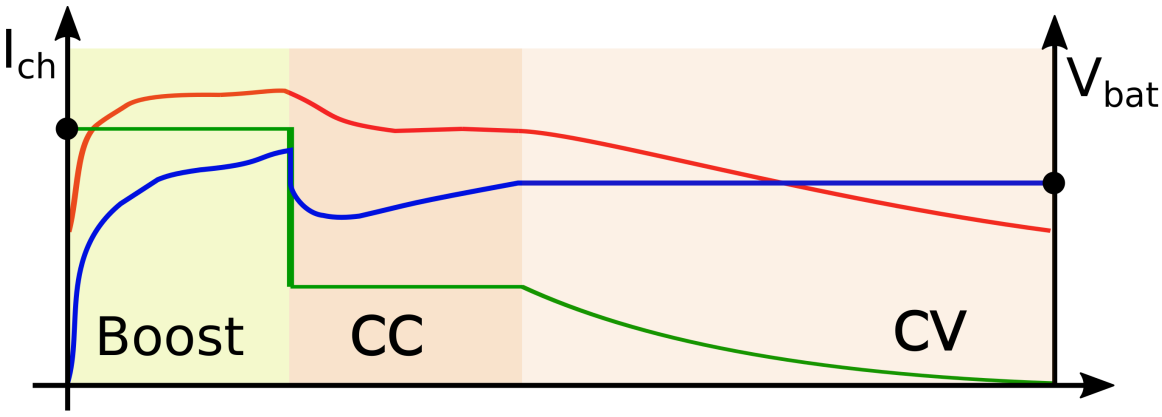


Figure 1.14: Boost charging profile.

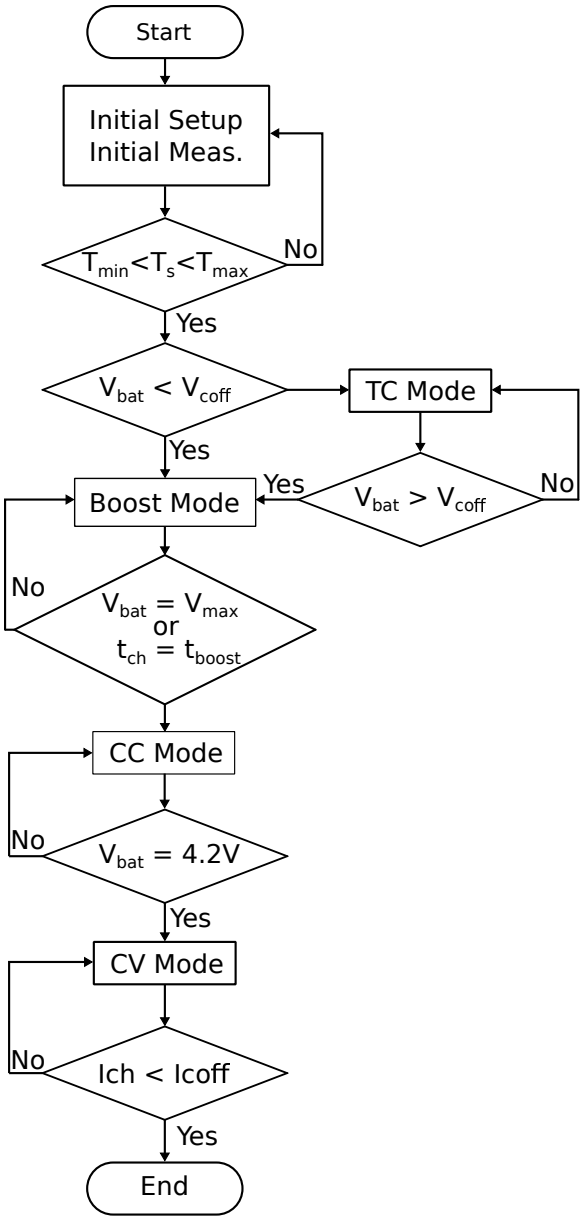


Figure 1.15: Boost charger flowchart.

### 1.5.4 Varying Current Decay Charging Method

The Varying Current Decay (VCD) method is based on the CV charging method, where the only limiting factor for charging is the voltage, thus resulting in very high currents during the entire SoC range of the battery. As seen before, these high currents

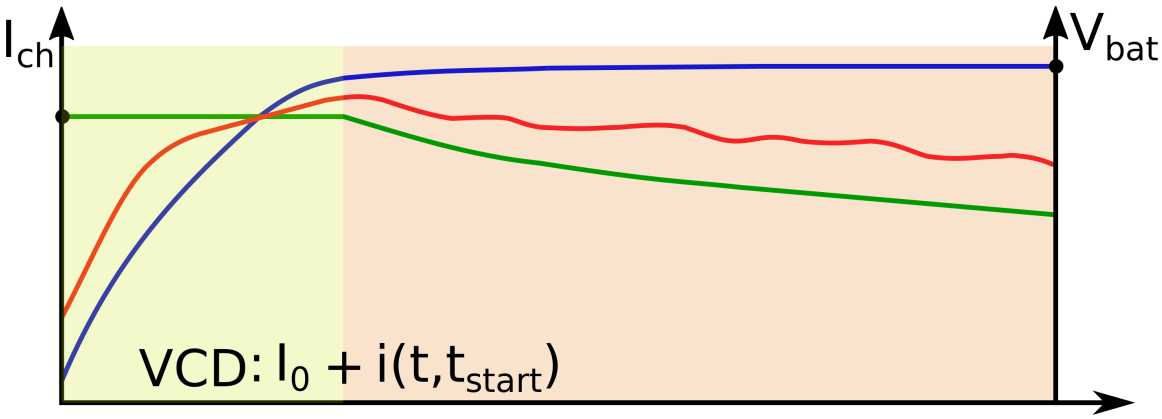


Figure 1.16: VCD charging current profile.

affect electrode potential. They produce overheating, leading to lithium plating, SEI layer growth, electrolyte oxidation, and active material degradation [4], so a current limit is needed while maintaining the battery voltage constant [35].

The current decay follows an equation, the parameters of which have to be tuned accordingly with the experimental results [35]. The tuning goal is to reach the $V_{cut-off}$ as soon as the charging starts; thus, the initial current is high, and it starts to decay slowly to maintain the battery voltage at $V_{cut-off}$. The cycling of the battery with the VCD method increases the internal battery resistance due to an increase in the electrode's potential, which leads to lithium plating. Therefore, the evolution of internal resistances leads to a varying charge profile throughout the cycles of the battery [35].

Figure 1.16 shows the characteristic curve I-V curve vs time of a VCD charger. Figure 1.17 shows the basic flowchart for boost charger charging methods.

### 1.5.5 Pulse Charging Method

The pulse charging technique generates a train of pulses with controlled magnitude and on-off time, as shown in Figure 1.18. These pulses can either be positive, followed

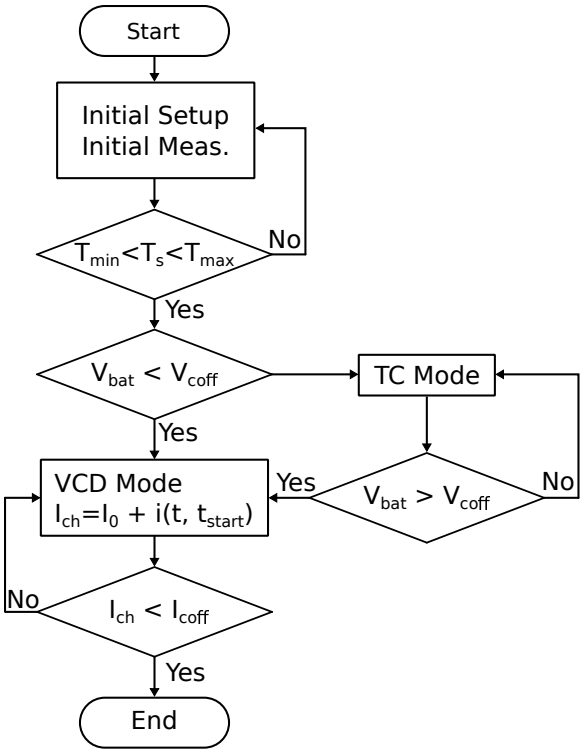


Figure 1.17: VCD charger flowchart.

by an off state, or a positive pulse followed by a negative pulse; the Frequency [Hz] (Hz) can also change according to the optimal charging current and SoC.

Since the battery is a chemical element, lithium ions move from one electrode to another in a diffusion process; the higher current of fast charges causes electrode polarization and ion gradient to increase due to the process's intrinsic transport limitations [30] [36]. Therefore, the pulse charging let the diffusion process accommodate the ions evenly in the electrode, allowing ion concentration to an average level [30] [36]. However, studies presented by [36] show no advantage in charging time or aging of the cells with this charging method. Also, the algorithm to generate the pulses is complicated, where it needs to find the optimum charging profile for each battery.

Figure 1.18 shows the characteristic curve I-V curve vs. time of a pulse charger. Figure 1.19 shows the basic flowchart for pulse charger charging methods.

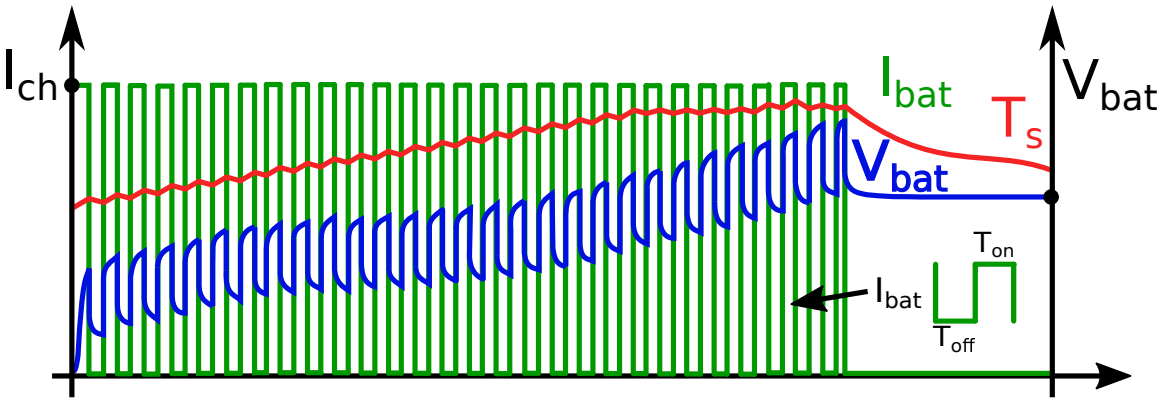


Figure 1.18: Pulse charging current profile.

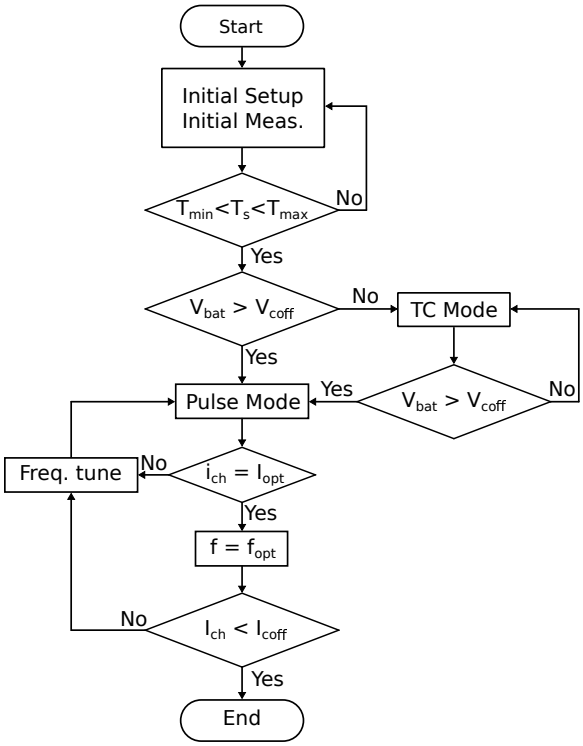


Figure 1.19: Pulse charger flowchart.

### 1.5.6 Sinusoidal Ripple Current Charging Method

The battery model can be modeled into electrical circuit models, where passive elements like resistors, capacitors, and inductors can be used to model the I-V

curves [37]. The AC impedance model is used as motivation for Sinusoidal Ripple Current (SRC) [38]. This model has the Walburg impedance, which influences the total battery AC impedance only when below 1 Hz [38]. Performing an electric circuit model analysis, it is possible to derive an optimal charging frequency for each SoC range, as shown in Figure 1.20, where the AC impedance is minimum.

The study performed in [38] tested SRC charging method with various frequencies and compared to pulse charging and CC-CV charging at the same average charging currents. It resulted in faster charging, with lower temperature increase, and enhanced battery life. In contrast, the analysis performed in [39] challenges the findings on [39], and the reason is electrical circuit models are not suited to consider the chemical process and its properties, thus SRC is not capable of reducing the battery impedance. Moreover, experimental results in [39] with different charging frequencies and the same average current did not show the same results, with charging time and temperature rise remaining the same as CC-CV.

Figure 1.20 shows the characteristic curve I-V curve vs time of a SRC charger. Figure 1.21 shows the basic flowchart for SRC charger charging methods.

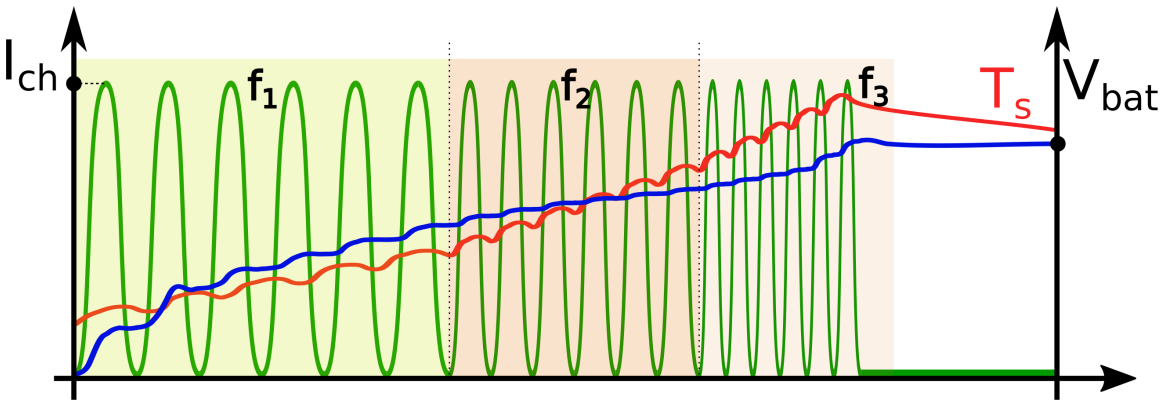


Figure 1.20: SRC charging current profile.

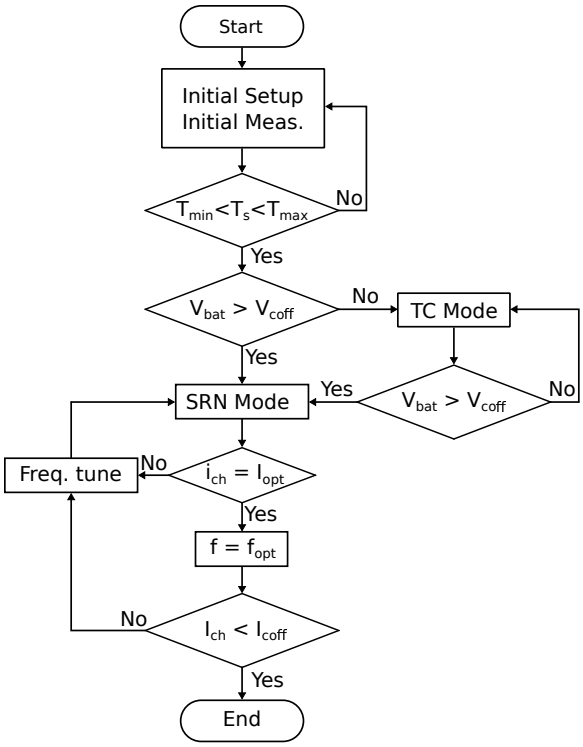


Figure 1.21: SRC charger flowchart.

### 1.5.7 Constant-Temperature Constant-Voltage Charging Method

The CT-CV charging technique was implemented by Smart Transportation Electrification and Energy Research (STEER) group. The basic idea was implemented and is presented in [40], which experimentally tested the charging technique with Nickel Cobalt Aluminum $LiNiCoAlO_2$ (NCA) 18650 cylindrical cells at room temperature. Accordingly, the results showed an improvement of charge time around 20% compared to the CC-CV charging technique. Besides the excellent results, it is still necessary to study the suggested charging methodology at different ambient temperatures and with different cells. Furthermore, it is necessary to study the aging effects of this charging technique.

CC-CV charging technique has a slow rate of $T_s$ rise, reaching the maximum temperature at the end of the CC phase due to constant charging current used. On the other hand, CT-CV ensures a fast $T_s$ rise at the beginning of charging by allowing higher current rates. With control of the charging current, it maintains the temperature constant until the end of the Constant Temperature (CT) phase. Consequently, it results in a larger average current with the same $T_s$, compared to a CC-CV charging technique with the same ambient temperature.

The $T_s$ of the cell is maintained constant during the entire CT phase with the control of the battery heat generation through charging current. A PID controller is used, whose feedback is generated by a temperature sensor attached to the cell's surface. Figure 1.22 shows the characteristic curve I-V curve vs time of a CT-CV charger. And, figure 1.23 shows the basic flowchart for CT-CV charger charging methods.

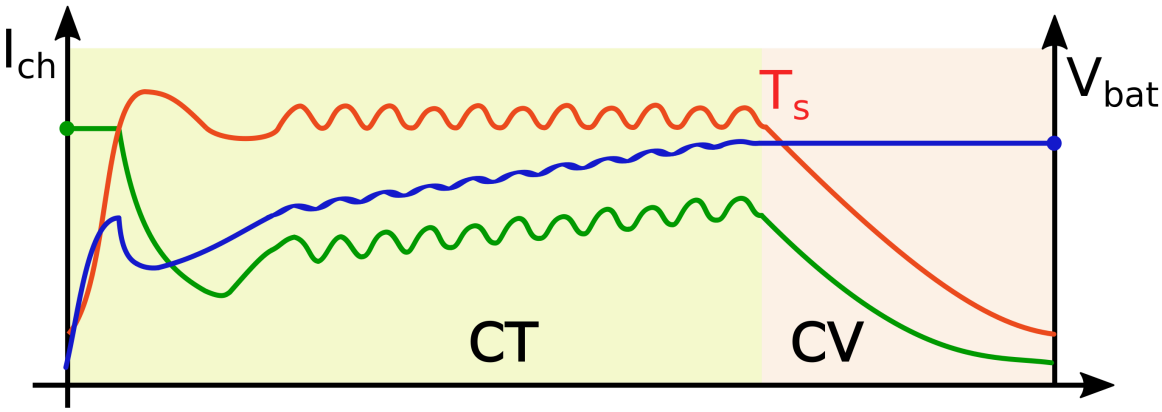


Figure 1.22: CT-CV charging current profile.

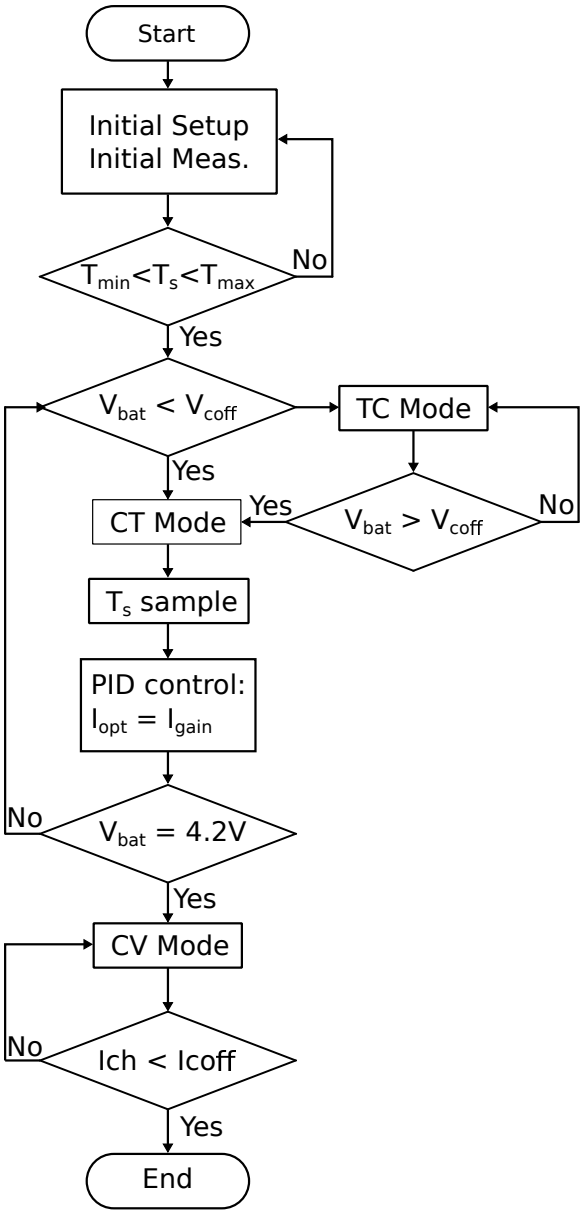


Figure 1.23: CT-CV charger flowchart.

### 1.5.8 Summary of Charging Methods

There are essential factors that need to be investigated before choosing the best charging technique for the EV design [41]. For fast chargers, the most critical factors are charging time, aging, temperature rise, and charge efficiency along the life cycle.

Table 1.2: Important factors of charging techniques.

| Charging technique | Meas. | Temp. | Eff. | Charge Time | Comp. | Cycle life |
|---|---|---|---|---|---|---|
| CC-CV | V,I | Prot. | High | High | Low | High |
| MSCC | V,I | Prot. | Med. | Med. | High | Med. |
| Boost | V,I | Prot. | Low | Low | Med. | Low |
| VCD | V,I | Prot. | Low | Low | High | Low |
| Pulse | V,I | Prot. | High* | High* | High | High |
| SRC | V,I | Prot. | High* | High* | High | und |
| CT-CV | V,I, $T_s$ | Ctrl | und | Low | Med. | und |

*V: Voltage, I: Current, $T_s$: Surface temperature, und: undefined, Med: medium, Meas. : Measurements, Temp.: Temperature, Eff.: efficiency, Comp.: complexity.
*charging techniques with dubious results

Also, the implementation complexity is another factor to be accounted for, as higher complexity leads to higher cost and computational burden.

Table 1.2 summarizes the main factors on the charging methods discussed in the literature review. It can be seen that slow charging techniques result in better life cycle and efficiency. On the other hand, fast charging techniques tend to degrade the battery life cycle and have medium to high implementation complexity. Moreover, some charging techniques have dubious results from one study to another, explained by different battery chemistry. It is necessary to perform various tests to have reliable results, for example, charge time, efficiency, and aging tests with different chemistry.

## 1.6 Scope of the Thesis

The demand for EV technology is increasing these days, and the need for fast charging is becoming crucial so that the EV can be comparable to conventional ICE vehicles. However, one cannot simply charge the battery with higher current rates without degrading battery life. The higher current rate increases the temperature rise on battery packs, which will result in a faster capacity fade. This thesis assesses a fast-

charging methodology capable of maintaining the temperature of the battery constant while still maintaining more rapid charge rates when possible; thus, the gap of a faster charging method with uncontrollable temperature rise is assessed.

Throughout the studies on different charging techniques, the goal is to have a fast charging algorithm that is capable of maintaining high life cycle, high efficiency, and lower temperature rise with less complex systems to be implemented. In the journey, CT-CV charging method fulfills the stated requirements to charge the battery packs within safe boundaries. The scope of this thesis is to study in depth the effects of CT-CV charging on three different 18650 cylindrical cells at different ambient temperatures.

The CT-CV results are analyzed and compared with the traditional CC-CV charging method. The parametric variations, like charge time, efficiency, and temperature rise, have been evaluated on three different batteries. Furthermore, the aging effect and temperature rise and life cycle will be assessed for one particular cell at room temperature of approximately 25°C employing the CT-CV and CC-CV charging methods.

## 1.7 Thesis Objectives

The objective of this thesis is to validate CT-CV as a fast charging method while maintaining the similar performance of the CC-CV under various conditions, such as different ambient temperatures and different batteries. In the end, CT-CV charging time is expected to be improved in comparison to CC-CV while equivalent CE and similar life cycle are expected to be found. The thesis has been divided into chapters as outlined below.

- Chapter 1: Introduction with broad information on electric vehicles and its components. Literature review on charging methods and thesis objectives.

- Chapter 2: Main aspects of battery specifications and terminologies seen in the literature. Experimental test methodology to acquire the results necessary for comparison between CT-CV and CC-CV and the methodology for the thermal-electrical modeling.

- Chapter 3: CT-CV and CC-CV charge time, coulombic efficiency, and aging results over a temperature range, and different batteries. Thermal-electrical model results for CT-CV charge method.

- Chapter 4: Concludes the findings and contributions of this thesis. Details for future work are also outlined.

# Chapter 2

# Battery Specifications and Methodology

Lithium batteries are extensively used in portable devices due to their ability to store a good quantity of energy, have low self-discharge, and be recharged. To compare different batteries, a set of standardized variables and terminologies presented in the literature is discussed. Second, a battery automated test system designed for testing batteries is presented, followed by the battery specification for each part number used in this work. Third, a thermal-electrical circuit model is presented, and the parameters acquisition method is shown. Lastly, the CC-CV and CT-CV charging method and implementation are extended with the comparison of relevant charging performance tests.

## 2.1 Battery Terminology

- **Battery classification:** the batteries are divided into non-rechargeable and rechargeable. Primary batteries are not rechargeable, and once the discharge is

complete, they have to be discarded and replaced with a new battery. Secondary batteries are rechargeable with a finite number of cycles. These batteries are used in smartphones, computers, EVs [41].

- **Nominal Capacity:** is the maximum charge the battery can deliver when fully charged. The manufacturer in the datasheet specifies it. The capacity is measured in Amper-hour [Ah] (Ah) [28].

- **C-rate:** is a normalization of electrical current in terms of nominal capacity. For example, a 3 Ah battery will take 1 hour to fully discharge when 1C load is applied; thus, 1C is equivalent to 3 A. Also, if a 0.5C discharge rate is connected to the battery, it will take 2 hours to discharge fully, and the current is 1.5 A [28].

- **State-of-Charge (SoC):** is capacity retained in the battery compared to the nominal capacity, and it is measured in percentage (%) [28] [42].

- **DoD:** is the capacity consumed from the battery based in the SoC, and it is measured in percentage (%) [42].

- **Terminal Voltage:** is the voltage being measured between the battery terminals. This voltage will vary depending on the battery current, SoC, life cycle, and temperature [28].

- **Open Circuit Voltage (OCV):** is the terminal voltage measured with no load condition after the battery is rested for a while. The OCV changes changes with temperature, life cycle, and temperature [28].

- **Charge Current:** is the magnitude of the current flowing into the battery from the charger device [28].

- **Cut-off Current:** is current limit defined by the manufacturer in the datasheet for the End of Charge (EoC), when using CC-CV method.

- **Discharge Current:** is the magnitude of the current flowing out of the battery to the load. The manufacturer defines maximum current to protect the battery from high discharge rates and keep it within a safe operating region.

- **Cut-off Voltage:** is the minimum voltage with which the battery can operate safely. Also, the battery is fully discharged when this voltage is reached.

- **Nominal Energy:** is the energy capability of the battery in Watt-hour (Wh), measured with full discharge, from 100% SoC to cut-off current at a specific C rate [28] [42].

- **Specific Energy:** is the amount of energy per unit of mass (Wh/kg) the battery can deliver. It is used to design the weight of the battery for range specification in EV application [28] [42].

- **Energy Density:** is the amount of energy per unit of volume (Wh/L) of the battery. It is used to calculate the volume of the battery according to range specification in EV application [28] [42].

- **Specific Power:** is the maximum amount of power per unit of mass (W/kg) the battery can deliver. It is used to calculate the weight of the battery pack to achieve specific performance [28] [42].

- **Power Density:** is the maximum amount of power per unit of volume (W/L) the battery can deliver. It is used to calculate the size of the battery pack to achieve specific performance [28] [42].

- **Operating Temperature:** limits the battery for both charging and discharging modes. The temperature specifications are well defined in the battery's datasheet, and they have different ranges for charge and discharge [21].

- **Cycle Life:** is the number of cycles the battery can have before failing. The criteria that EoL is reached when the battery capacity is 80% of the nominal capacity [25].

- **Calendar Life:** represents the aging of the battery when stored and not in use [24].

## 2.2 Battery Automated System

Battery testing is a complex task due to the long charge and discharge duration; it becomes a time-consuming process. Furthermore, the battery is a sensitive component, as seen in Chapter 1, and it is essential to maintain the voltage, current, and temperature under the limits specified in the datasheet. Therefore, these tests can be easily done manually. However, when there are multiple tests to be performed, the automated test is a better option, since they provide higher reliability with data logging. Thus, automated tests are the best options for the scope of this work.

There are automated test rigs ready to use in the market, like battery cyclers. On the one hand, those cyclers are very efficient with the advantage to regenerate the power back to the grid. They are also very reliable, and the same charge and discharge cycle can be repeated for a large number of cycles. On the other hand, they are expensive, and also they usually have proprietary software that does not offer an easy way to implement custom charging techniques. For this reason, a custom BAS is designed to accomplish the scope of this work.

The main advantage of a custom BAS is software flexibility, lower costs, and modularity. First, flexibility allows the user to create any script to be tested. Second, the lower price is possible due to multiple manufacturers providing solutions for the components used in a BAS. Finally, the modularity is likely because many pieces of equipment can be stacked up. Multiple scripts can run in parallel, which decreases the test time for multiple batteries when necessary.

A custom BAS is implemented for testing the charging methodologies in the scope of this thesis. The block diagram shown in Figure 2.1 represents the components used. The power paths are given in solid lines, and they carry the high currents, while the dashed lines are the communication and signal paths for the BAS.

The electronic load is used to simulate the load the battery is powering. It can be constant or variable, and it is connected to the battery through the discharge switch ($SW_{DISC}$). The power supply is used as the charger when the charging switch is connected ($SW_{CHAR}$); it can have constant or variable currents to simulate multiple charging methodologies. The temperature chamber emulates the environmental temperature, while the temperature sensors measure the battery surface and ambient temperatures. The data acquisition system (DAQ) measures the temperature sensor analog output. Finally, a computer is connected to all equipment through Universal Serial Bus (USB) and a serial interface for control purposes and data acquisition.

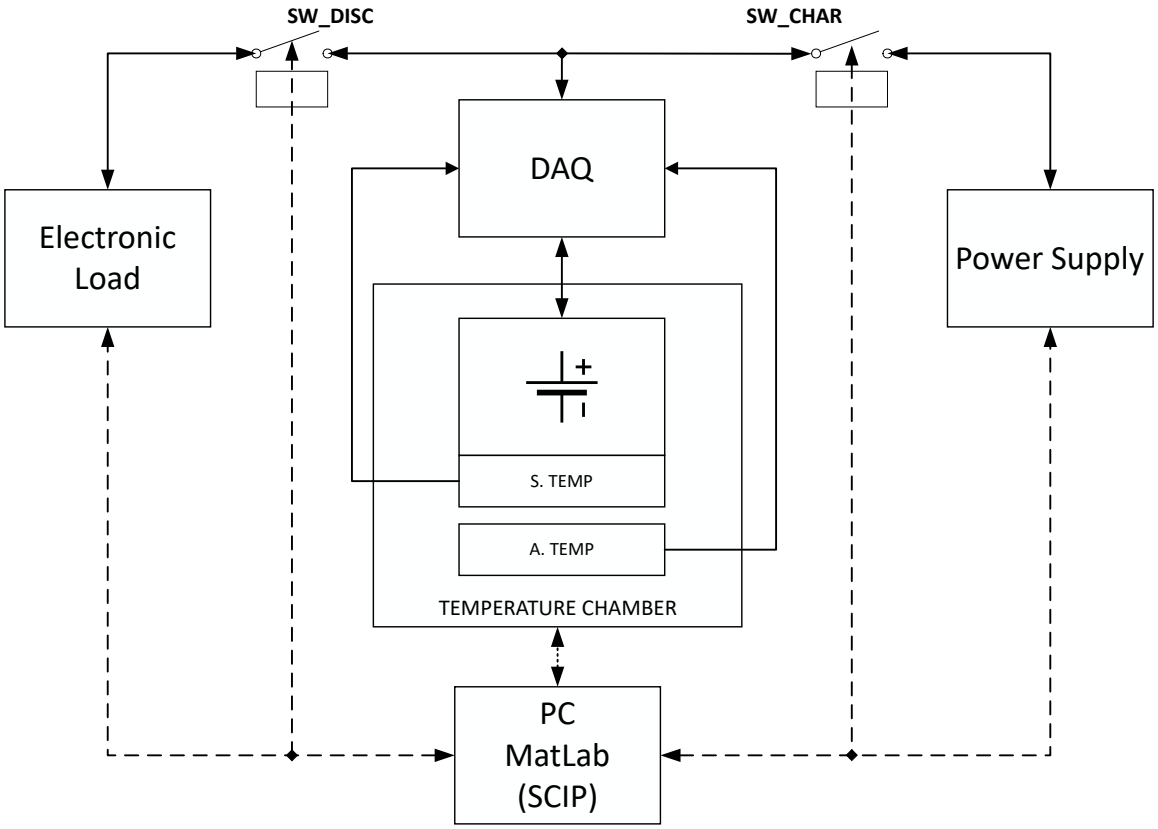


Figure 2.1: Battery Automated System Diagram. Dashed lines are the communication and signals, and the solid lines are the high current paths.

### 2.2.1 Hardware

The instruments on BAS need to be able to test the BUT at maximum characteristics of current, voltage, and temperature. Table 2.1 summarizes the BUT's maximum operating range and the measurement accuracy needed. The BUT specifications are found in the datasheets and introduced at the end of this chapter.

Table 2.1: BUT maximum operating requirements.

| | Range | Accuracy |
|---|---|---|
| Terminal voltage | 0-6 V | ±10 mV |
| Charge current | 4 A | ± 100 mA |
| Discharge current | 20 A | ± 100 mA |
| Ambient temperature | -10°C to +60°C | ±2°C |
| Battery temperature | -10°C to +60°C | ±2°C |

Following the diagram shown in Fig. 2.1, the following instruments were chosen:

- Power Supply: Programmable power supply from Keysight model E3613A, with three channels. Channel 1 is used as the charger due to power capabilities being higher than other channels. Channel 2 is used to command the discharge switch. Finally, channel 3 is used to command the charge switch. A special characteristic is a 4-wire connection, which is used to eliminate the cables' effects, like voltage drop.

- Electronic Load: programmable electronic load from B&K Precision model BK8601. Its only channel is used as a load. A special characteristic is a 4-wire connection, which is used to eliminate the cables' effects like voltage drop.

- Data Acquisition System (DAQ): Programmable DAQ from Manufacturer Chroma model DPM66204. It is used to acquire the voltage from the temperature sensors. These analog readings are converted from voltage to temperature measurements in Kelvin and Celcius by the software.

- Switches: two relays.

- Temperature Chamber: programmable temperature chamber from Manufacturer Associated Environmental Systems.
- Temperature Sensors: precision temperature sensor calibrated to Kelvin temperature scale. Additionally, a calibration using a DDM from the manufacturer Fluke Model is performed. The temperature sensor assembly is studied in more detail in Chapter 2.2.4.
- Power Cables: Lead wire 1050 treads AWG38.

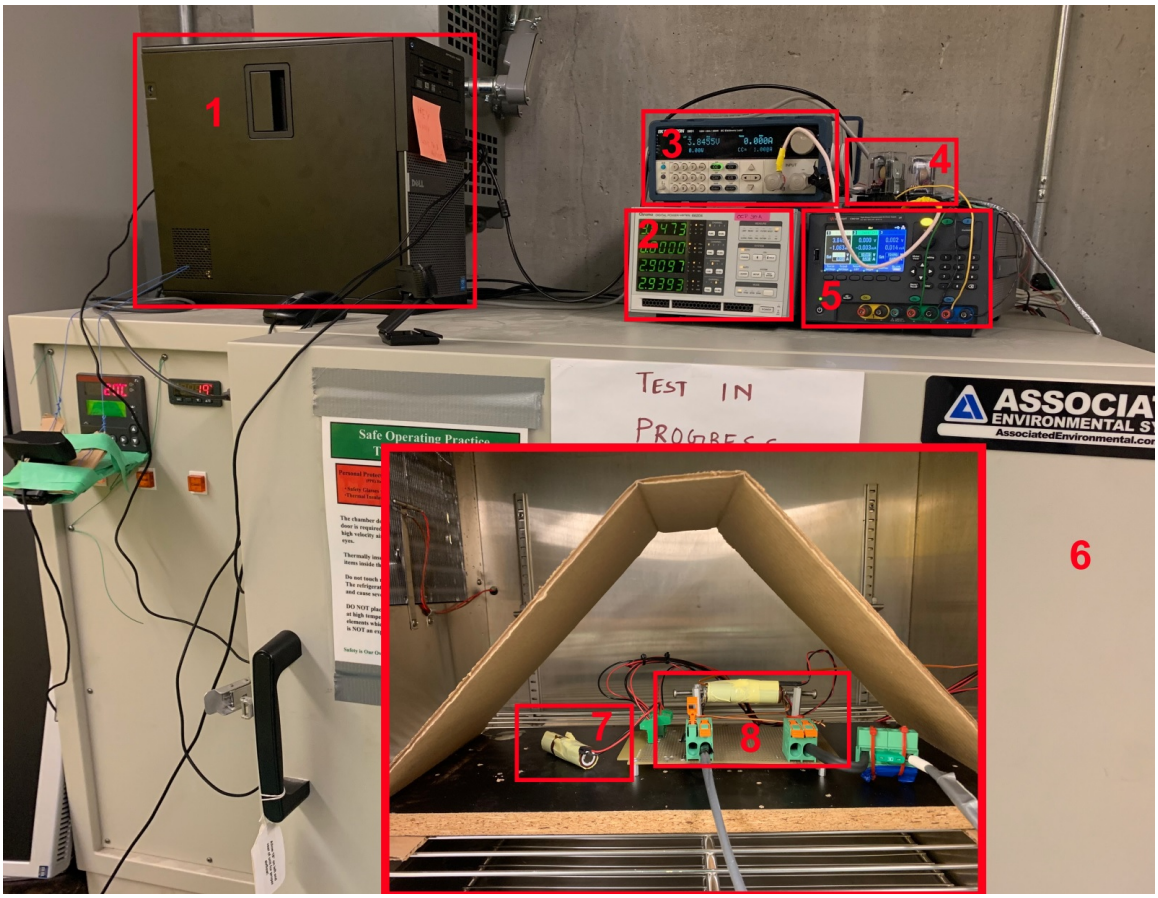


Figure 2.2: BAS external view with the following equipment: 1-Computer, 2-DAQ, 3-Electronic Load, 4-Relays, 5-Charger, 6-Temperature Chamber, 7-Ambient Tempearture Sensor, 8-BUT.

Finally the BAS specifications are shown in Table 2.4. The capabilities are over-

specified in case the BAS is used with other tests, and different BUT used in this work scope.

Table 2.2: BAS specifications.

| | Range | Accuracy |
|---|---|---|
| Terminal voltage | 0-6 V | ±10 mV |
| Charge current | 10 A | ± 3 mA - 80 uA* |
| Discharge current | 60 A | ± 60 mA - 6 mA* |
| Temperature Chamber | -40°C to +125°C | ±2°C |
| Battery temperature | -10°C to +60°C | ±2°C |

*Low voltage/current range.

### 2.2.2 Software

The BAS needs software to run the testing, and it needs to have flexibility, reliability, and modularity. Figure 2.3 shows the framework used for the BAS software. The software is programmed using Matlab enviroment due to excellent compatibility with the instruments through Standard acronyms for Programmable Instruments (SCPI) and a vast number of libraries and online support.

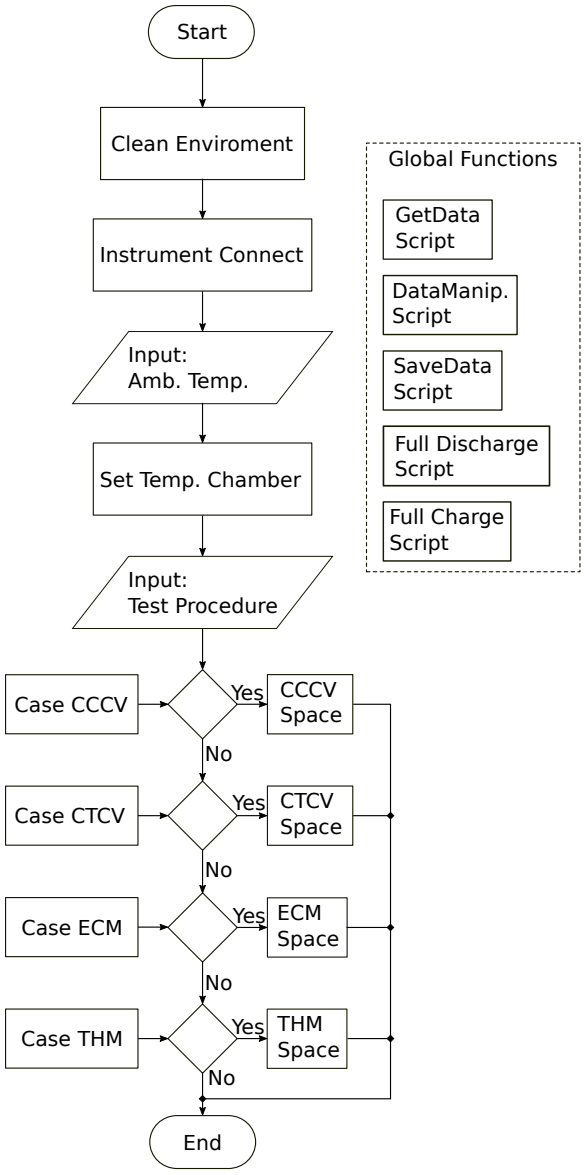


Figure 2.3: BAS Main framework.

The details of the test procedures are covered in the following chapters for better comprehension. There are repeatable tasks that need to be executed in all the test procedures. For example, getting data from instruments, data manipulation, and saving data are used globally. Thus, global functions are written, and they are summarized below:

- Instrument Connect: connects to all instruments through serial communication (USB and RS-232) and initializes communications.
- Set Temperature Chamber: operates through Modbus protocol; thus, a specialized function to communicate with it is needed.
- Get Data: acquire data from instruments using SCPI and store in MatLab workspace.
- Data Manipulation: it does the translation from voltage to temperature readings to Kelvin and Celcius. It also contains the calibration information for the temperature sensors.
- Save Data: get all data from Get-Data function and Data-Manipulation and save it into Comma Separated Values (CSV) file for later data analysis.
- Full Discharge: to initialize the charging tests, the battery needs to be fully discharged. Thus, this function makes the discharge standard, with cut-off voltage and discharge current, as user input.
- Full Charge: to initialize the discharge tests, the battery needs to be fully charged. Thus, this function makes the charge standard CC-CV, with charge current and cut-off current as user input.

### 2.2.3 Battery Under Test

The batteries under test (BUTs) studied in this thesis are new cells, with form factor 18650. They were primed with 10 cycles on CC-CV charge method, at standard charge currents specification, as shown in Table 2.3. The Lithium Nickel Cobalt Manganese Oxide $LiNiCoMnO_2$ (NCM) chemistry was chosen to be tested because

it has high density, providing high specific energy and specific power. This chemistry mix has also been proven to be very efficient, safe, and reliable, as it is being used in EV applications, such as Nissan Leaf, Chevy Volt, and BMW i3 [43].

Table 2.3: BAS specifications.

| | **BUT1** | **BUT2** | **BUT3** |
|---|---|---|---|
| **Manufacturer** | LG Chem | LG Chem | Samsung SDI |
| **Model** | INR18650HG2 | INR18650HE4 | INR18650-30Q |
| **Nominal Voltage** | 3.6 V | 3.6 V | 3.6 V |
| **Nominal Capacity** | 3 Ah | 2.5 Ah | 3 Ah |
| **Standard Charging*** | 1.5 A, 4.2 V<br>Cut-off: 50 mA | 1.25 A, 4.2 V<br>Cut-off: 50 mA | 1.5 A, 4.2 V<br>Cut-off: 150 mA |
| **Fast Charging*** | 4.0 A, 4.2 V<br>Cut-off: 100 mA | 4.0 A, 4.2 V<br>Cut-off: 100 mA | 4.0 A, 4.2 V<br>Cut-off: 100 mA |
| **Max. Discharge** | 20 A | 20 A | 15 A |
| **Discharge Cut-off** | 2.5 V | 2.5 V | 2.5 V |
| **Operating Temperature** | C.: 0 to 50°C<br>D.: -30 to 60°C | C.: 0 to 50°C<br>D.: -30 to 60°C | C.: 0 to 50°C<br>D.: -30 to 60°C |
| **Weight** | 48 g | 47 g | 48 g |

*CC-CV charging

### 2.2.4 Temperature Measurement and Sensor Assembly

The cylindrical types of batteries have the worst-case scenario for the heat dynamics [44]. Its internal layers of a cylindrical cell are not exposed to the air. Therefore, the core temperature is higher than its surface temperature [44]. Furthermore, the 18650 cell enclosure has less surface area than the most common battery types. The radial temperature gradient is larger, with the core having higher temperatures than its surface. However, the longitudinal temperature gradient is uniform due to the current distribution in this dimension being evenly spread [44].

Therefore, only one temperature sensor was used to measure surface area, located in the middle of the cell. Figure 2.3 shows the complete assembly steps from a) to d). The plastic protection was opened in the middle of the sensor. A thermal paste was used to improve heat transfer between the sensor and cell surface, and finally, the sensor was fixed with polyester tape.

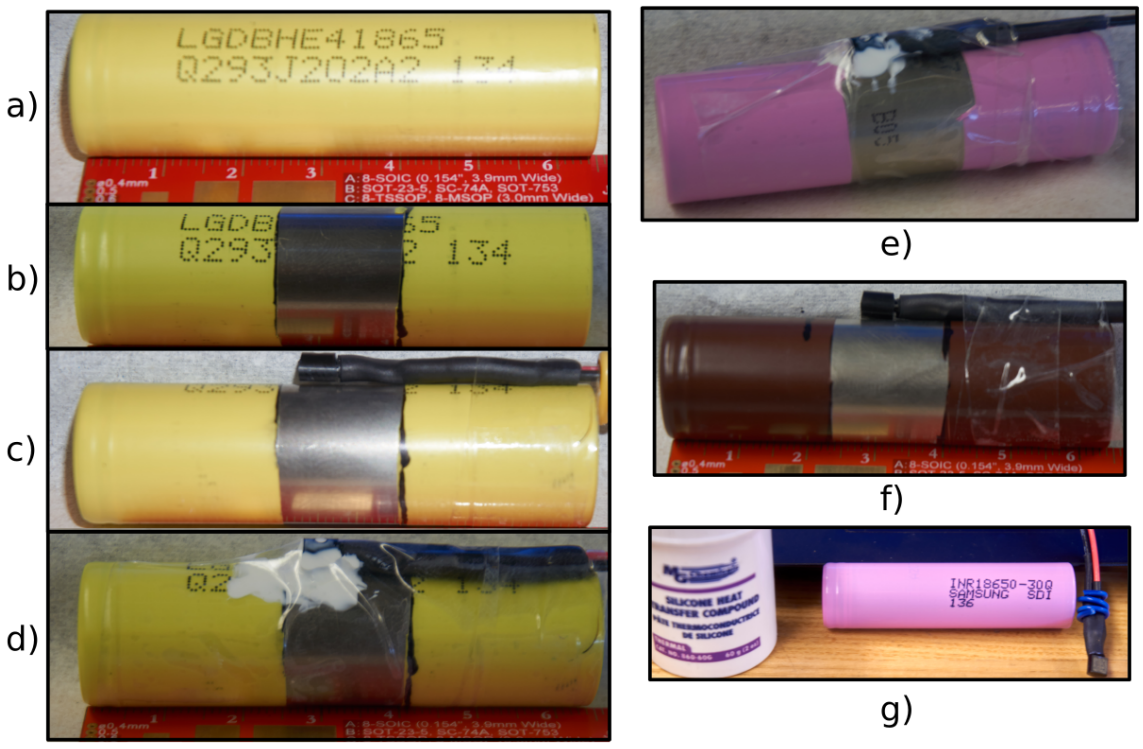


Figure 2.4: Temperature sensor assembly.

$T_a$ and $T_s$ temperatures sensors were assembled the same way, with $T_a$ being assembled spare cell. The LM335 was powered by a constant 12 V supply, and its schematic is shown in Fig. 2.5, with its output (anTs) going to DAQ analog input.

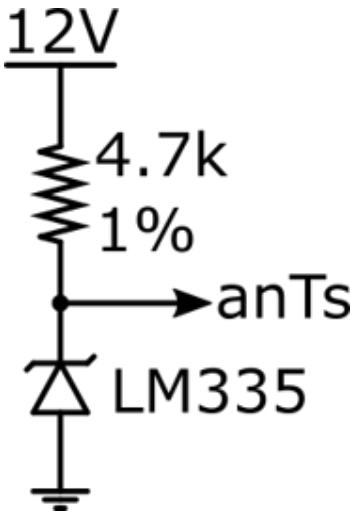


Figure 2.5: Temperature sensor schematic.

## 2.3 Modeling Methodology

The battery testing is time-consuming, sensitive, and needs to be safe. Thus, a model that can provide accurate temperature and voltage results is essential to predict the preliminary performance of new charging methodologies. A battery thermal-electrical circuit model can be implemented by analyzing the outputs to different inputs, and the model parameters can be found using mathematical models. However, these mathematical models can be complex and time-consuming for the scope of this thesis. Thus, the Matlab Parameter Estimation Tool is used instead, with the inputs used as $I_{bat}$, $V_{bat}$, $T_a$, $T_s$, and SoC. In the end, the thermal-electrical circuit model is analyzed with $T_s$, OCV, SoC, $I_{bat}$ and $V_{bat}$ outputs.

### 2.3.1 SoC

The SoC is calculated by the amount of charge left in the battery, and it is measured in Amper-Hour (Ah). Many factors degrade the precision of the SoC, like cell temperature, $I_{bat}$ magnitude, cell aging, and sensor accuracy [45]. However, there are many methods used to calculate SoC, and they range from simpler methods to sophisticated methods, which incorporate the non-ideal system. The simple SoC calculating methods are the OCV-SOC, which predicts the SoC based on OCV recorded points [42], and the Coulomb-Counting method, which integrates how many Amperes the battery received in an amount of time, calculating the charge. The sophisticated methods include the losses and temperature dependencies, like Artificial Neural Networks, Kalman Filters, and Fuzzy Logic [42].

The SoC calculation method used in this thesis is Coulomb-Counting, and it is shown in Equation 2.1 [42]. $SoC(t-1)$ is the last $SoC$ calculated value, $Q_n$ is the nominal capacity, $I(t)$ is the present current reading, and $\Delta t$ is the sampling time.

This method is inexpensive to implement, and as the BAS instruments have great accuracy, it minimizes the instrumentation errors. Also, to avoid initial errors, each test script is primed with a charge and a discharge cycle to reset the SoC calculation.

$$SoC(t) = SoC(t-1) + \frac{I(t)}{Q_n}\Delta t \tag{2.1}$$

The modeling is a very time-consuming task to be performed, so we limited it only for BUT1. Thus, all the modeling test procedures were repeated with 3 different $T_a$: 0°C, 20°C, and 50°C. Moreover, three different currents were used: 150 mA, 1.5 A, and 4.0 A, following datasheet specifications. The SoC is then adjusted by these factors with look-up tables.

### 2.3.2 ECM

The electrical system modeling provides the electrical response of the battery, like OCV, $V_{bat}$, $I_{bat}$, run-time and internal losses. Many models in the literature are capable of providing excellent results. For example, an electrochemical model is a complex approach for battery modeling, where both microscopy and microscope parameters are modeled into a system of differential equations [46]. However, these models are incredibly time-consuming, and their accuracy is dependent on the battery specific details.

The analytical models can give good results when vast data from the battery is used, thus increasing the simulation time. With the minimum input data from the battery, the system limitations increase considerably [47].

The ECM modeling approach has shown promising results, with errors ranging from 1% to 5% [37], and it is suited to give accurate run-time, transient, and losses results; thus, it will be used in this thesis.

The ECM uses electrical elements to represent the battery response, where Resistance [Ω] (R) and Capacitance [F] (C) are used to describe the transients and steady-state characteristics. A controlled voltage source is used to represent OCV characteristics. Also, there are basic and complex models. The basic models are too simple to represent the voltage's transient characteristics, resulting in low accuracy.

Nevertheless, the complex models like the Thevenin-based model have a good response with transients when the parameters can change over SoC, temperature, current, and charge/discharge hysteresis. Another ECM is the impedance-based models. However, they require an Electrochemical Impedance Spectroscopy (EIS) instrument to acquire the frequency response [48] to have the circuit parameters, increasing the experimental cost of the BAS. Hence, a Thevenin-based model is used for this thesis's battery model, and it is shown in Fig. 3.38.

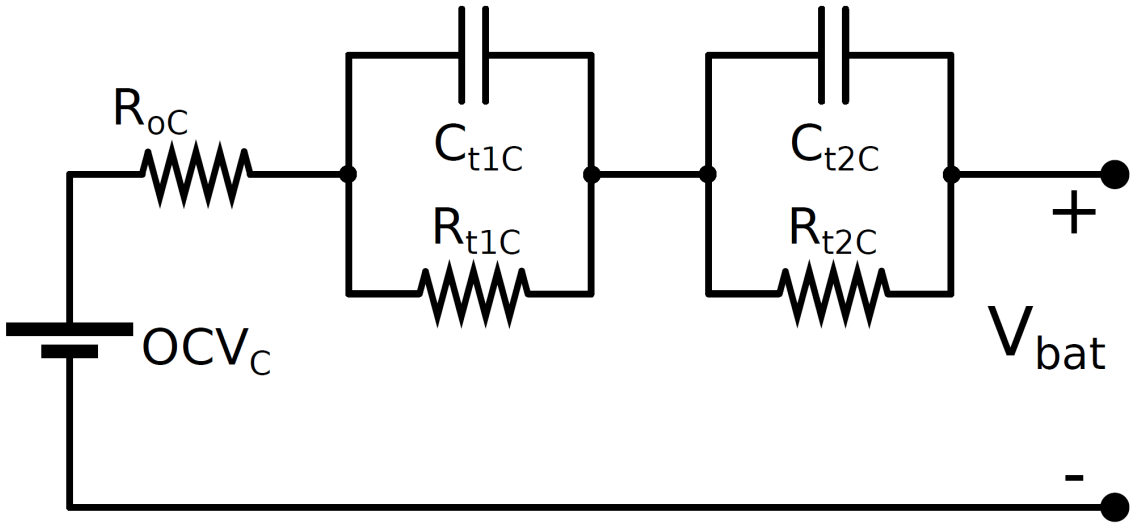


Figure 2.6: ECM diagram.

The two RC networks model was selected due to its optimum performance when compared to error analysis of other quantity of RC networks [49]. First, the DC response is caused by the electrolyte resistance on the lithium-ion transportation,

and it is represented in the ECM by $R_{0C}$. Second, the short transient response is caused by the lithium-ion flow in the SEI and anode electrode, and it is represented in the ECM as $R_{t1C}$ and $R_{t1C}$. Third, the long transient response is caused by double-layer capacitance in both electrodes, and it is represented in the ECM by $R_{t2C}$ and $C_{t2C}$ [50]. These components are modeled with three inputs, SoC, $I_{bat}$ and $T_a$, thus a three-dimension interpolated Look Up Table (LUT) is used. The controlled voltage source is $OCV_C$ represents the OCV, which is influenced only by $T_a$ and SoC, thus it is modeled with a two-dimension interpolated LUT.

Matlab 2019b Parameter Estimator toolbox is used for parameter estimation. The parameters showed in Figure 3.38 are found through a non-linear least squares method using this tool. The parameter estimator needs the experimental data and the simulation data of the tests to be performed. As the parameters are functions of $T_a$, SoC and $I_{bat}$, a series of experiments are needed to acquire the data.

The first task is to build the LUT for the controlled voltage source, with OCV-SoC, for three $T_a$, 0°C, 20°C, and 50°C; Due to the elevated number of testing, the low current method was selected to acquire the OCV-SoC response. The low current method uses a very low current (1/20C). The low current has little effect on electrodes polarization [49], thus the terminal voltage can be considered as the OCV, as shown in Figure 2.7.

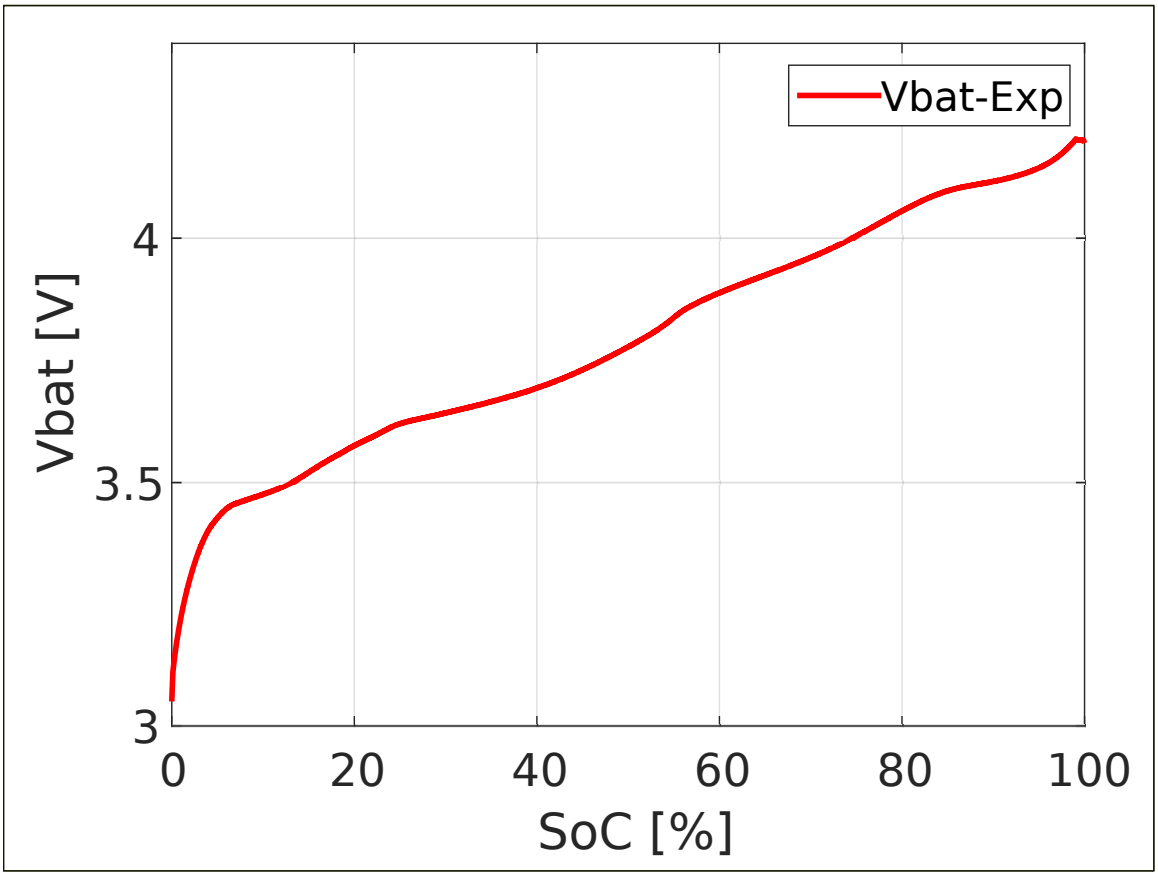


Figure 2.7: OCV-SoC curve response test for charge model.

The second task is to build the LUT for each parameter, $R_{0C}$, $R_{t1C}$ $R_{t2C}$, $C_{t1C}$, $C_{t2C}$. As they are function of SoC, $I_{bat}$ and $T_a$, nine tests are needed. The pulse test methodology was used, and these tests have positive current pulses during charge [37] [51]. The pulses have duration of 5% SoC, and depending on the amplitude of the pulse, they will have different time duration. This fraction of the SoC is needed to achieve an accurate estimation, where the higher fraction will result in better system response for the non-linear response. The pulse test is shown in Figure 2.8, where it is possible to visualize $V_{bat}$, $I_{bat}$ and SoC for charge.

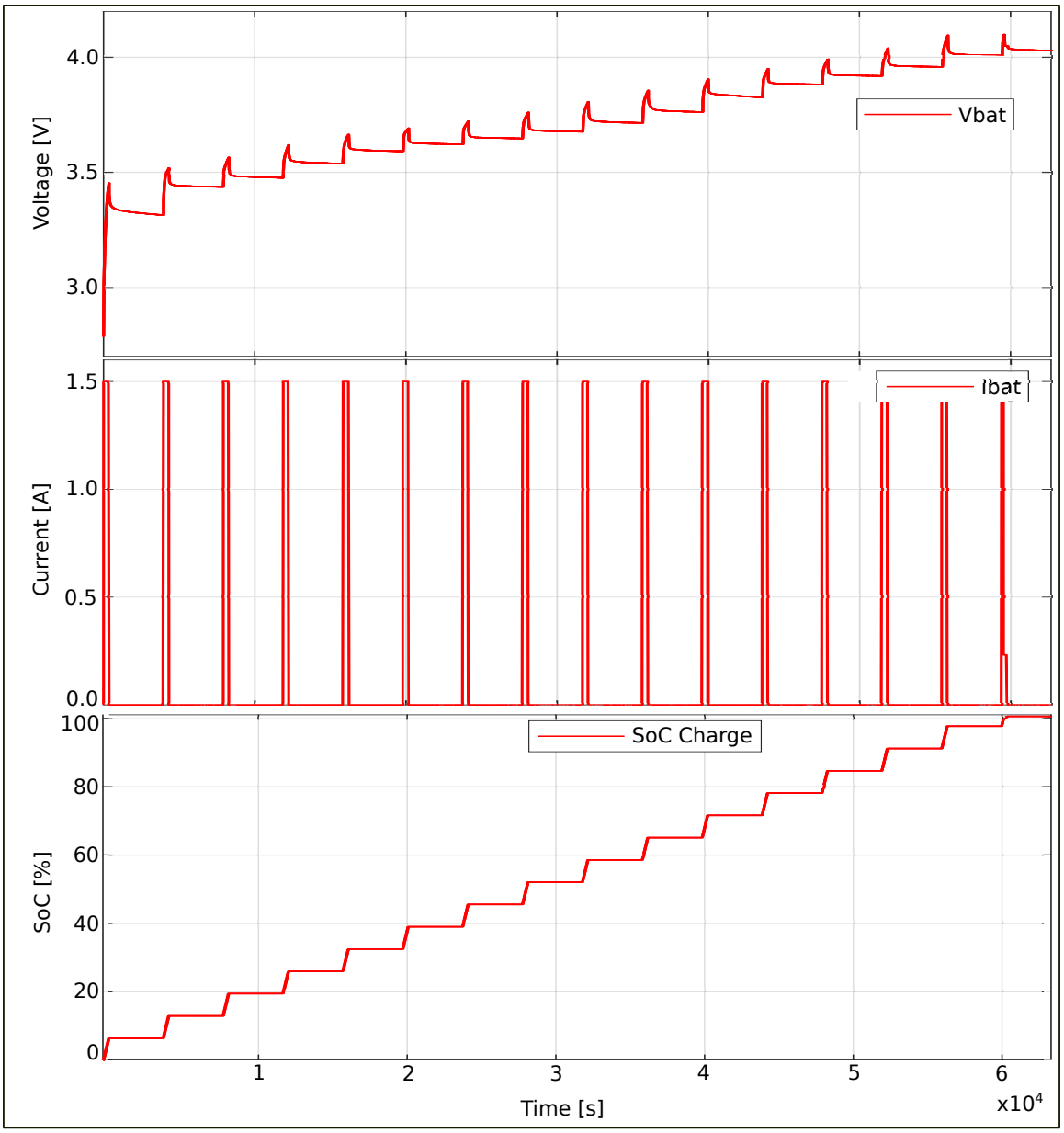


Figure 2.8: Pulse test curve characteristics of $V_{bat}$, $I_{bat}$, and SoC.

The current pulse test generates the voltage response seen in Figure 2.9. First, when the pulse is triggered, the voltage response has a instantaneous voltage drop, which is modeled by $R0_{SoC_a,I,T_a}$ ($R_{0C}$). Second, the voltage response has a relaxation part, which is divided in a short response modeled as $RC_{SoC_a,I,T_a}$ ($R_{t1C}$ $C_{t1C}$), and in a long response modeled as $RC_{SoC_a,I,T_a}$ ($R_{t2C}$ $C_{t2C}$) [37].

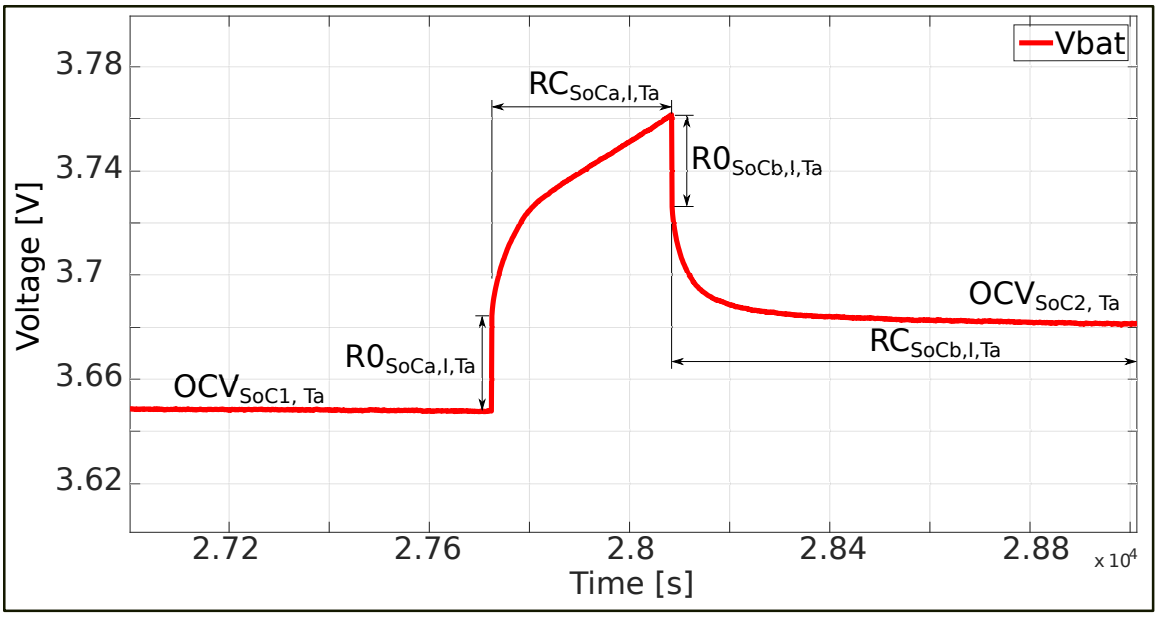


Figure 2.9: $V_{bat}$ response during one pulse for charge model.

In total, there will be 12 tests to be performed to acquire all the experimental responses needed for the parameter estimation of the ECM. Additionally, there will be 12 parameter estimation tasks to be formed by the Parameter Estimator tool.

The ECM acquired using this method will be used to define the heat generation used in the coupled electrical, thermal model, which in the end results in a model capable of predicting electrical and thermal characteristics for the CC-CV and CT-CV charging techniques.

### 2.3.3 Thermal Modeling

Lithium batteries have different form factors like prismatic cells, pouch cells, and cylindrical cells, as shown in Figure 2.10 [5]. They are all formed by a layer stack composed of a copper current collector, negative electrode, separator, positive electrode, and aluminum current-collector. Also these layers are immersed into electrolyte [5] as shown in Figure 2.11.

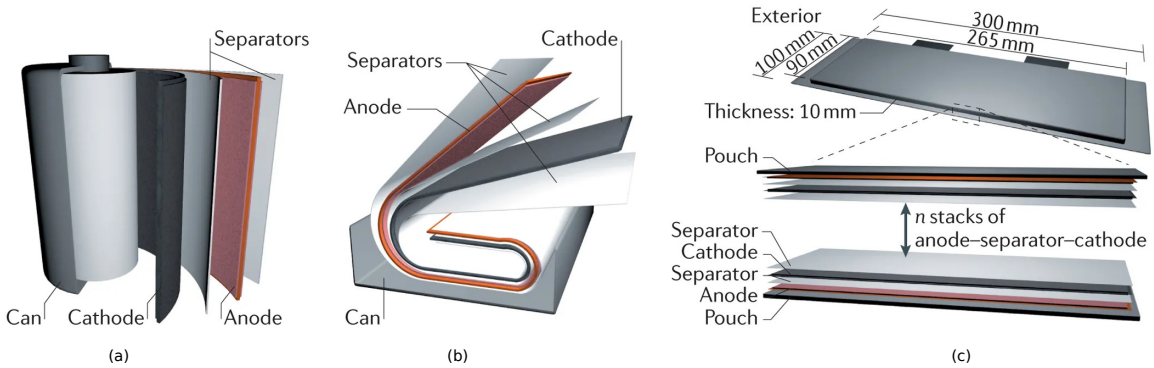


Figure 2.10: Battery cell commercial form factors: (a) Cylindrical, (b) Prismatic, and (c) Pouch [5].

The cylindrical cell has the worst thermal heat dissipation among these form factors due to its layer being arranged in a spiral form. Thus, the layers in the innermost of the cell have higher thermal resistance to the ambient. As shown in Figure 2.11(a). This arrangement leads to a big thermal gradient between internal temperature and surface temperature. This thesis is based on a temperature-dependent charging model. The thermal modeling methodology will be focused on this 18650 form factor, but the idea can be easily transferred to other form factors.

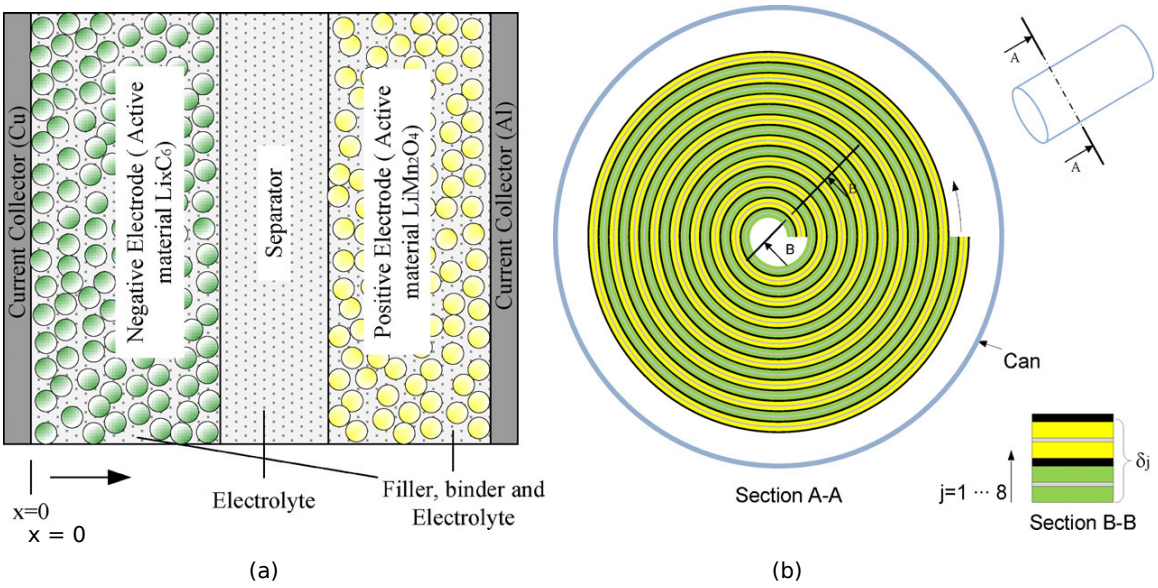


Figure 2.11: Internal physical cylindrical cell: (a) Layer structure and (b) cell schematic [6].

There are several thermal models studied in the literature. [44] [6] [27] [52] [53] study a cylindrical battery using detailed mathematical and numerical models accounting for the layers' thermal characteristics. Their results are very detailed, with layer temperature information at multiple locations; it also produces low errors when specific boundaries are set. Still, the proposed models consume a huge amount of computational power because they have to account for each layer at a determined point as the heat generation, thermal resistance, and thermal capacitance change with the radius of the cell. They also require very detailed information about cell structure, material properties, and cell assembly, which is not easily well informed by the cell manufacturer.

Simpler cell models presented the model with four elements: Heat generation being at the very center of the cell. All layers thermal characteristics summed up into one layer, resulting in a single thermal resistance and single thermal capacitance. The case characteristic with a second thermal resistance and capacitance for the

model. The ambient temperature [54] [55] [56]. The models resulted in a reasonable computational effort and good error margins. Even though the literature offers online parameter estimation to further reduce errors, it is not on the scope of this thesis. However, it is good to have a model capable of evolving to online parameter estimation in future work.

Figure 2.12 shows a representation of the thermal physics happening on the cell in (a) and its second thermal model in a schematic type representation in (b). The heat conduction occurs from the core to the surface through the thermal resistance ($R_{ti}$) and thermal capacitance ($C_{ti}$) [57]. These two parameters represent the entire layer stack thermal characteristics and are not given in the battery cell datasheet; thus, they need to be estimated. The cell surface exchanges its heat with the ambient in a convection manner through the case and ambient thermal resistance ($R_{ts}$), and thermal capacitance ($C_{ts}$). Finally, the heat generation ($Q$) is considered a concentrated source in the middle, and it is power loss of the battery generated by the ECM resistances.

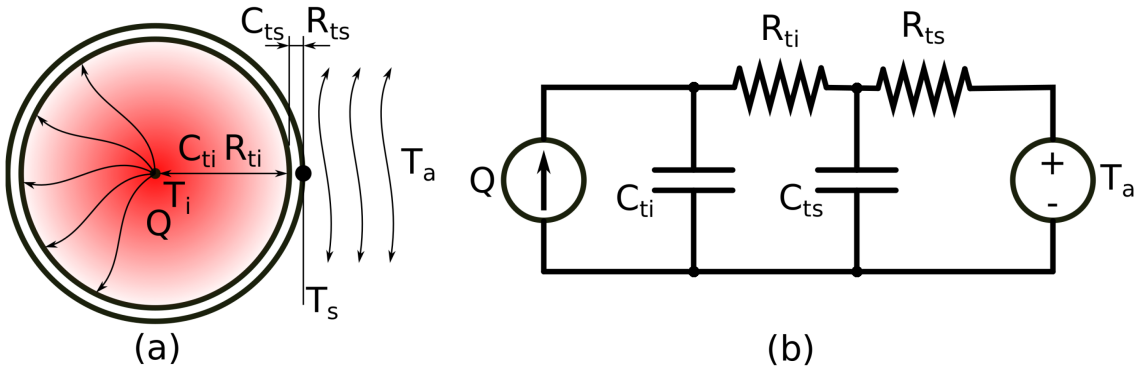


Figure 2.12: (a) Cylindrical cell radial view. (b) Second order thermal model.

The power loss gives the heat generation, and it is dependent on the battery internal resistance and current, as shown in Equation 2.2. The resistances are dependent

on the SoC, $I_{bat}$ and $T_a$, thus the heat generation is also a function of these inputs. Moreover, the ECM must provide the power loss for each element, where $I_{R1C}$ is the current going through the short transient response resistor, and $I_{R2C}$ is the current going through the long transient response resistor.

$$Q = I_{bat}^2 R_{0C} + I_{R1C}^2 R_{1C} + I_{R2C}^2 R_{2C} \tag{2.2}$$

With the heat generation being provided by the ECM, it is possible to couple both models. Analyzing the heat balance on the core of the cell, we derive Equation 2.3, where the rate heat flows into this point is equal to the heat generated ($Q$) minus the rate heat flows away from the point. A similar analysis is performed on the cell's surface, though there is no heat being generated at this point, thus resulting in Equation 2.4

$$C_{ti}\frac{dT_i}{dt} = Q - \frac{T_i - T_s}{R_{ti}} \tag{2.3}$$

$$C_{ts}\frac{dT_s}{dt} = \frac{T_s - T_a}{R_{ts}} - \frac{T_i - T_s}{R_{ti}} \tag{2.4}$$

In order to determine thermal resistances $R_{ti}$, $R_{ts}$, $C_{ti}$ and $C_{ts}$, the Parameter Estimator from Matlab using non-linear least squares is used. The coupled electrical-thermal model is used for this estimation [58], with the the ECM operating with its elements varying with SoC, $I_{bat}$ and $T_a$. The experimental data for the parameter estimator to be used is the same used in the charging techniques for both CC-CV and CT-CV, at $T_a$ of 0°C, 20°C, and 50°C. Also, the current used was in the range from 150 mA to 4.0 A.

### 2.3.4 Error Analysis

The thermal-electrical model will be compared with the experimental results, with Root Mean Square Error (RMSE) (Equation 2.5), Mean Absolute Error (MAE) (Equation 2.8) and Squarred Correlation Coefficient ($R^2$), where $V_{batn}$ is voltage experimental value and $\hat{v}_{batn}$ is the simulated voltage value. The MAE is used to have an idea of the mean errors between model and experimental, while the RMSE is used to detect large and non-frequent errors along the simulation results.

$$V_{RMSE} = \sqrt{\frac{1}{n}\sum_{j=J}^{n}\left(V_{batn} - \hat{v}_{batn}\right)^2} \tag{2.5}$$

$$V_{MAE} = \frac{1}{n}\sum_{j=1}^{n}\left|V_{batn} - \hat{v}_{batn}\right| \tag{2.6}$$

$$T_{S-RMSE} = \sqrt{\frac{1}{n}\sum_{j=J}^{n}\left(T_{sn} - \hat{T}_{sn}\right)^2} \tag{2.7}$$

$$T_{S-MAE} = \frac{1}{n}\sum_{j=1}^{n}\left|T_{sn} - \hat{T}_{sn}\right| \tag{2.8}$$

The thermal-electrical model is acquired using this methodology and used as a complementary study for this charging technique. The experimental results from the charging methods are to be used and to validate the charge model acquired.

## 2.4 Charging Methodology

The proposed charging methodology CT-CV performance is accessed by performing charging and discharging tests at various environmental conditions. The BUT on which tests are to be performed are described in Chapter 2.3, and the sensor assembly

is shown in Chapter 2.2.4. The battery is mounted in a pressure holder, where all the battery surface area is exposed to the ambient to ensure similar heat exchange in all points of the cell surface.

To check the BUTs' initial condition, they are to be primed before testing. The priming is composed of one cycle using CC-CV with standard charging parameters, shown in Table 2.3. The discharging is to be performed with 600 mA to the specific cut-off voltage. The prime is necessary to check the cells' real capacity and the temperature rise during the charge as well as to calibrate the SoC algorithm.

### 2.4.1 CC-CV

The CC-CV charging methodology is used as a benchmark for the CT-CV performance check. Also, the temperature setpoint for the PID controller of the CT-CV is set to the maximum $T_s$ acquired during the CC-CV charge. Each of the BUT is to be tested in three $T_a$: 0°C, 20°C, and 50°C.

Figure 2.13 shows the full test flowchart. The test starts with the BAS being set to the desired ambient temperature, followed by one hour rest time, in order to achieve temperature equilibrium between the cell core and ambient. The next step is loading the charging standard charging parameters shown in Table 2.3 for the desired BUT.

The prime starts with it being charged from unknown SoC with standard CC-CV until the end of the charge, followed by a rest period of 15 minutes. The discharge is performed with a lower current to ensure full discharge of the cell, avoiding ohmic losses when high discharge current is applied.

Succeeding the prime test and its rest, the CC-CV charging method to be analyzed is performed. The maximum $T_s$ acquired during this charging phase is used as a reference for the CT-CV testing for the same $T_a$. The CC-CV charging test ends

with a 15 minutes rest time, followed by a discharge.

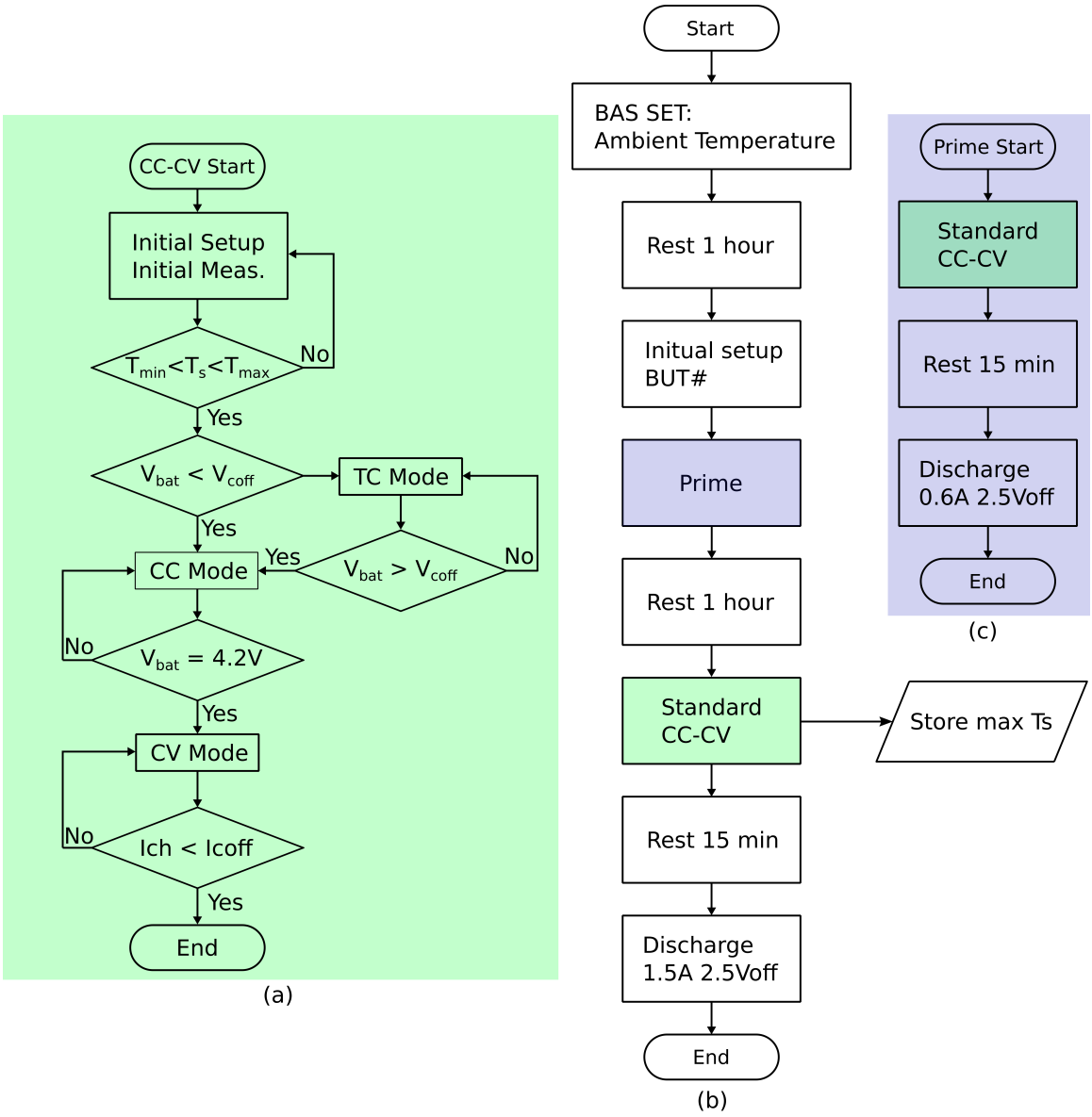


Figure 2.13: CC-CV charging method test: (a) charging flowchart, (b) Test flowchart, (c) Prime flowchart.

$$CE(T_a) = \frac{C_{disc}}{C_{ch}} \tag{2.9}$$

By performing the test flowchart shown in Figure 2.13, it is possible to study the

CE of this charging method for 0°C, 20°C, and 50°C ambient temperature by dividing the total discharge capacity ($C_{disc}$) by the total charge capacity ($C_{ch}$), as shown in Equation 2.9. Also, a comparison of temperature rise can be made between both charging methods.

The charge time to SoC 20%, 40%, 60%, 80% and 100% will be measured in order to compare both charging methods optimal SoC range. CC-CV has a linear increase of SoC due to constant current applied. Once it shifts to CV, the current has an exponential decay, which can be seen also in the SoC. Meanwhile, the CT-CV will have a variable current depending on the PID controller and $T_s$.

### 2.4.2 CT-CV

The CT-CV charging methodology is based on controlling the $T_s$ of the cell by varying the heat generation through charging current, as reviewed in Chapter 1.5.7, and Chapter 2.3.3. The CT-CV charging methodology is more complex than CC-CV charging methodology due to the addition of a temperature sensor for control and the tuning of the PID controller to achieve optimal charging time. However, the implementation is easier than most of the technologies presented in Chapter 1.5, since the temperature sensing can be implemented cost-effectively. This is presented in Chapter 2.2.4 and the controller is straightforward and widely used for temperature control in the industry.

PID controllers provide good performance in various systems and can be operated simply and directly. There are many techniques for tuning PID controller gains, and most of them are based on developing a mathematical model for the combined final control element, process, and measurement. However, this system's mathematical model comprehends many non-linear elements with too many variables influencing the system response, like temperature, current, and SoC. Thus, the Ziegler-Nichols

heuristic method is chosen for tuning the temperature controller used in the CT-CV.

The method relies on the open-loop response of the $T_s$. The S-shaped curve similar to the one showed in Figure 2.14 is used to define the closed-loop gains ($K_p$, $K_i$, and $K_d$). The inflection point A is found, and its tangent line is plotted to determine the delay time (L) and the time constant (T). Finally, the gains are calculated through Equations 2.10, 2.11 and 2.12.

$$K_p = 0.5\frac{T}{L} \tag{2.10}$$

$$K_i = 2L \tag{2.11}$$

$$K_d = 0.5L \tag{2.12}$$

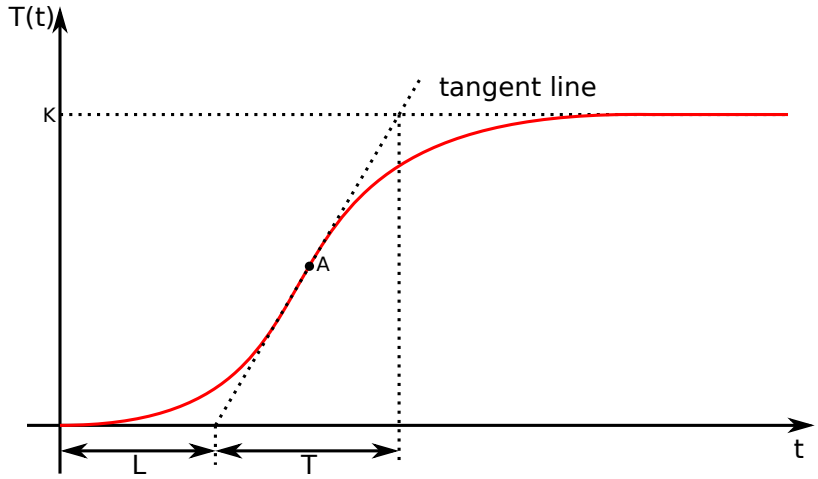


Figure 2.14: Life cycle test flowchart.

Additionally to the Ziegler-Nichols method, fine-tuning of the controller is to be performed, where trial and error tests will be necessary to achieve the best system response. Specifically, the gains will change as shown in the Table 2.4, which relates the closed-loop gains $K_p$, $K_i$ and $K_d$ to their influence on the system response. In addition, the gains are specific for each BUT, and they are acquired at $T_a$ of 20°C;

yet, they will be used for 0°C and 50°C tests.

Table 2.4: Overview of PID gains influence on the system response.

| Gain | Rise Time | Overshoot | Settling Time | Stead-state error |
|---|---|---|---|---|
| $K_p$ | decrease | increase | NRC* | decrease |
| $K_i$ | decrease | increase | increase | decrease |
| $K_d$ | NRC* | decrease | decrease | no change |

*NRC: not relevant change.

Figure 2.15 shows the flowchart to be used to achieve the best PID tune for the CT-CV charging algorithm, where the overshoot should not go over 2°C above the reference, and the steady-state error should be zero or below the reference. Additionally, a trade-off between rising time and charge time is expected, since they will reflect in the charge current, where a faster rise time will reflect in lower currents afterward to reduce the heat generation and control $T_s$ on the desired setpoint. Hence, the fine-tune task will analyze the charge current and $T_s$ profiles, where fine tweaks on $K_p$, $K_i$, and $K_d$ will be performed. The fine tweaks will be done taking into consideration the information in Table 2.4 and will have the goal to adjust the average current magnitude above the CC-CV charge methodology.

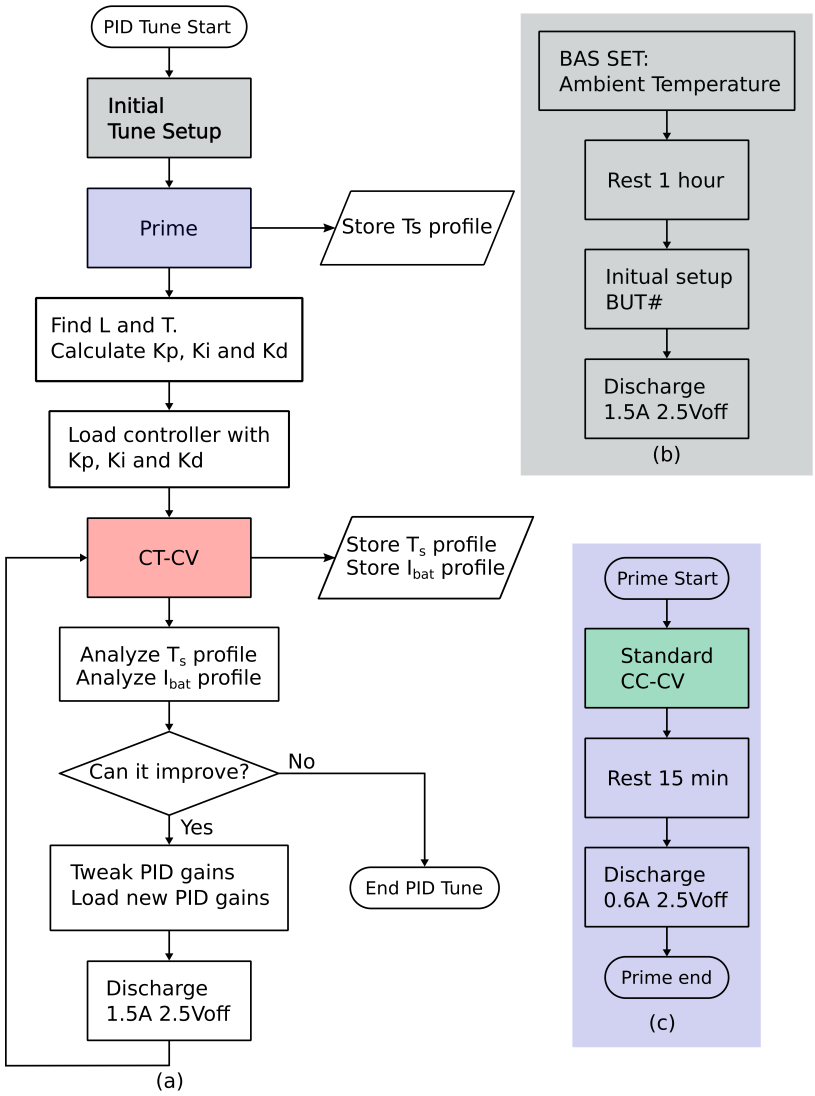


Figure 2.15: (a) PID controller tune flowchart, (b) Initial tune setup settings, and (c) prime for CT-CV charging test.

After fine tuning the PID controller gains $K_p$, $K_i$ and $K_d$, the CT-CV charging methodology will be tested similarly to the tests performed in CC-CV charge methodology, presented in Chapter 2.4.1. The CT-CV test flowchart is presented in Figure 2.16. The BAS will be set to desired $T_a$, and a rest period of one hour will occur to ensure equal temperature for all elements inside the chamber. After resting, the initial setup of the BUT is loaded, and the setpoint for CT-CV is the maximum $T_s$

acquired by the CC-CV charging of this specific BUT and $T_a$. After these procedures, the cell is primed and rested for another hour to be ready for the CT-CV charging.

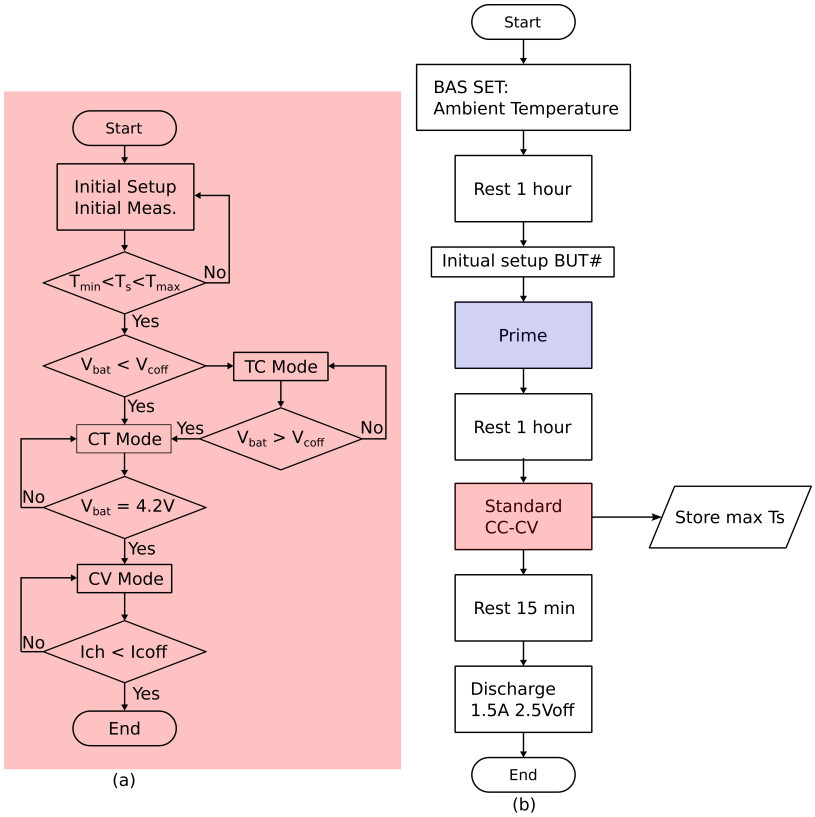


Figure 2.16: CT-CV charging method test: (a) charging flowchart, (b) Test flowchart.

Figure 2.17 shows in detail the CT-CV charging controller, where the error is calculated by subtracting the measured $T_a$ from the setpoint, as shown in Equation 2.13. The $n$ represents the time stamp where each measurement is taken, and it is set to 1 second. After calculating the error it is possible to find each component of the PID controller by following Equations 2.14, 2.15, and 2.16. The charging current will be set as the sum of these components, like Equation 2.17, and it will be limited by the maximum allowed charging current ($I_{max}$), which is determined by manufacturer as the fast charge current presented in Table 2.3. Succeeding the charging, there is a

short rest period followed by the discharge of the cell, and end of test.

$$errorTs(n) = Ts_{ref} - Ts(n) \tag{2.13}$$

$$Ip(n) = K_p errorTs(n) \tag{2.14}$$

$$Ii(n) = I_i(n-1) + K_i errorTs(n) \tag{2.15}$$

$$Id(n) = K_p(errorTs(n) - errorTs(n-1)) \tag{2.16}$$

$$Ich(n) = Ip(n) + Ii(n) + Id(n) \tag{2.17}$$

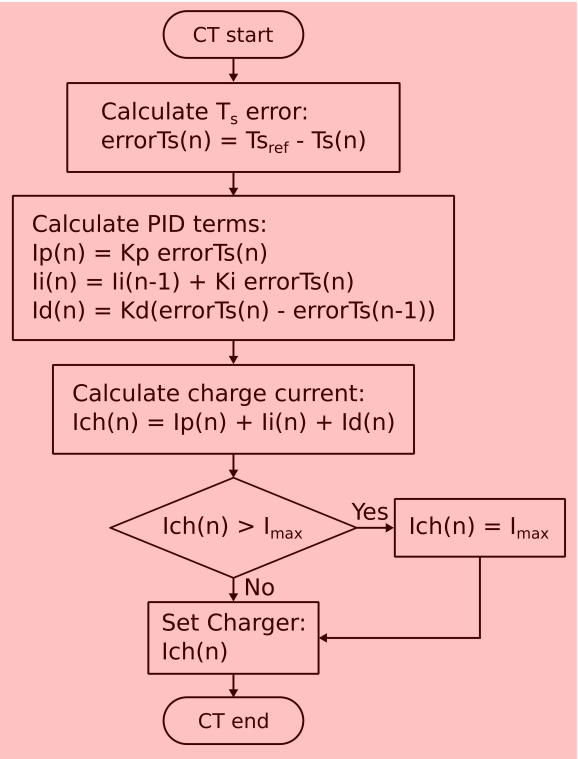


Figure 2.17: Detailed PID controller components calculations.

After performing the CT-CV charging test over different $T_a$ and with all the BUTs, it is possible to evaluate the charging methodology performance with CE, and the charging time to SoC 20%, 40%, 60%, 80% and 100%. Also, it is necessary to check

the $T_s$ response and ensure the cells are not going over the temperature reference.

The last test to be done with the CT-CV is the aging test to be performed at room temperature with BUT1, and it will be done at the same time as the CC-CV aging test.

### 2.4.3 Aging Methodology

The life cycle assessment will be done using the in-house designed BAS at room temperature. Two new BUT1 (INR18650HG2) will be tested. First, one cell will go for 1080 hours into cycling as shown in Figure 2.13 with CC-CV method. Second, the CT-CV charging methodology will be tested, with the cycling of the charge presented in Figure 2.16.

As the BAS can log all the data for all tests, it is possible to analyze the maximum surface's temperature for each cycle deeply. The average temperature for each cycle will be calculated and compared to the maximum surface temperature, resulting in the surface temperature rise. Thus, the assessment of the evolution of temperature will be possible along each cycle. Moreover, the charge time from 0% SoC to CV phase will be saved for each cycle.

## 2.5 Conclusion

This chapter presented the most important battery terminologies used in the literature and how they related to the battery behavior observed. After introducing these terms and giving a brief explanation of them, the chapter explained the BAS with information on how to build it with hardware and software implementation details. Moreover, the system's insights were detailed for the reader to build it if necessary, and introduce other testing routines if necessary. Subsequently, the thermal-electrical

model of the battery was reviewed. The thermal-electrical model chosen was explained in detail as well as the parameters extraction techniques necessary for the charging phase. At the end of the chapter, the CC-CV and CT-CV charging methodologies were explained, and flowcharts and implementation details were presented; also, the main testing was explained, like coulombic efficiency, charging time, and aging tests.

# Chapter 3

# Experimental Results

This chapter presents the test results discussed in Chapter 2. First the CT-CV PID controller tune results are presented. Second, both charging methodologies are compared. Third, the coulumbic efficiency details and results are shown. Forth, the aging results are presented, with the cycle life and capacity fade results. Finally, the results of the thermal-electrical model parameters are shown, and the CT-CV charging methodology is simulated and presented as well.

## 3.1 CT-CV PID Controller Results

The PID tune is shown first in the chapter in order to have the parameters established before showing the results for CT-CV charging methodology. Also, the tests are ordered chronologically.

The tuning procedure is presented in Chapter 2.4.2, where the values of the proportional, integrative, and derivative gain were achieved through the Ziegler-Nichols heuristic method. Subsequently, a fine-tune with the trial and error test procedure was performed. Table 3.1 shows the values for each gain considered for fine-tuning.

Table 3.1: PID gains considered for the controller fine tuning.

| | **PID1** | **PID2** | **PID3** |
|---|---|---|---|
| **P Gain** | 2.5 | 2 | 2 |
| **I Gain** | 0.001 | 0.01 | 0.02 |
| **D Gain** | 25 | 5 | 2.5 |

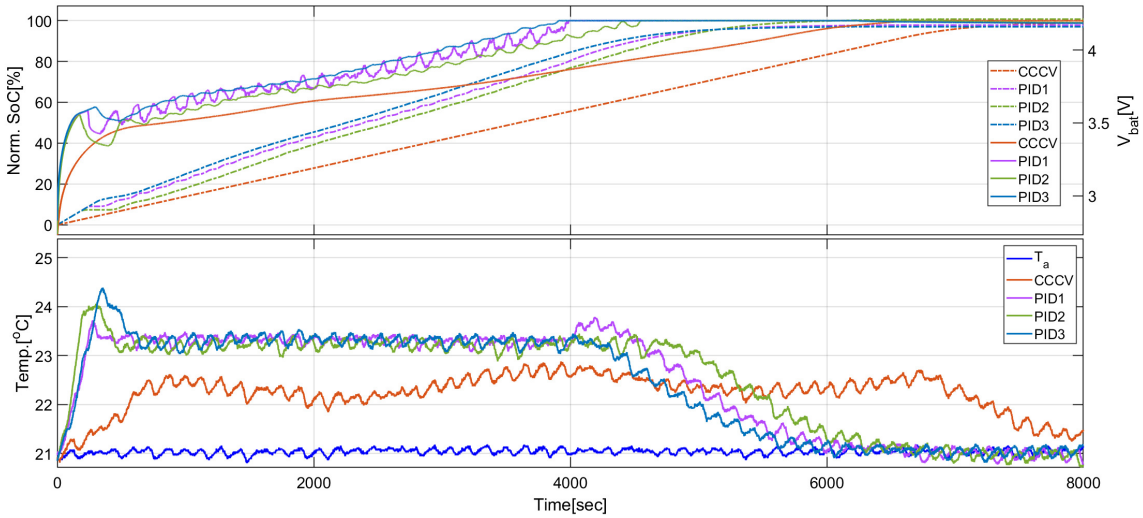


Figure 3.1: LG18650HG2 CT-CV tuning results. First graph represents the normalized SoC on the left y-axis, and battery voltage in the right y-axis. Second graph is $T_s$ and $T_a$ for PID tunes.

Figure 3.1 shows the SoC, battery voltage and $T_s$ responses. These curves were used for the fine-tuning analysis, and it represents each PID tune from Table 3.1. In addition, the curve acquired with CC-CV charging methodology is shown for comparison.

The SoC profile, shown in dashed lines in the upper graph, shows how the tunes are performing along with the battery charging, and its slope inclination indicates the charging current values. For example, in the first 500 seconds, the $T_s$ error between the setpoint and the surface temperature measurement is large, so the controller

allows maximum charging current to be used. The high current leads to a steeper slope on SoC. After this steeper slope, a flat region is present, and this is due to the PID controller handling the overshoot by controlling the charging current, which results in the cell decreasing its temperature.

Observing the SoC results, it becomes evident that the PID3 tune has the best result. The curve rises to higher SoC faster than PID1 and PID2. It can be observed at the beginning of the charge that PID3 has a steeper slope for a longer duration than other tunes. Also, the flat region is not present, and instead, a slower slope is found due to non-zero charging current. The SoC was normalized with a capacity of 3 Ah, in order to compare the charging times with the same reference.

The battery voltage ($V_{bat}[V]$) results shown in solid lines in the upper graph from Figure 3.1 are also used to analyze the PID gains. The tune performance can be analyzed with $V_{bat}$, more specifically on the transition time between charging modes: CT to CV. The optimal system response is when $V_{bat}$ reaches the cut-off voltage of 4.2 V at higher SoC, as it can be observed with tune PID3. Even though PID2 and PID3 have similar transition time, it can be observed that the PID3 transition happens at higher SoC than PID2. Moreover, the PID2 tune produces oscillation on $V_{bat}$, which is related to the high current oscillation produced by the PID controller.

Furthermore, $V_{bat}$ shows an elevated peak voltage from 0 to 500 seconds for all PID tunes. The high current produces this voltage spike at the beginning of the CT mode, where the PID controller sets the charger with a maximum charging current. Thus, the PID3 has shown the best performance when analyzing $V_{bat}$ curves, where the voltage did not oscillate too much and reached the cut-off voltage at higher SoC than other PID tunes.

The surface temperature profiles presented in the lower graph of Figure 3.1 are used to validate the tune performance. With these profiles, it is possible to analyze

the rise time, overshoot, and steady-state error for each tune. PID1 presents the minimum overshoot and has the same steady-state error of all other tunes. However, it has an uncontrolled temperature rise at the end of the charge, which can be related to the higher current at the end of the CT phase. The high current is taken as the starting current for the CV phase. The current decays exponentially to maintain the voltage constant at 4.2 V. Moreover, PID2 does not present an overshoot at the end of the charge, as $T_s$ is maintained at a low steady-state error, with only 0.8°C overshoot at the beginning of CT mode. However, the charging time had a worse performance than PID1 and PID3, which is related to the average charging current.

Moreover, PID3 presented the best results of charging time, when analyzing SoC profile and $V_{bat}$ profile. However, it can be observed that PID3 $T_s$ profile has higher overshoot than PID1 and PID2, with overshoot of 1.2°C above the setpoint. The cause of this is the controller allowing the charger to have the maximum charge current for a longer period of time at beginning of charge. Even though the overshoot is higher, it is still under the allowed overshoot presented in Chapter 2.

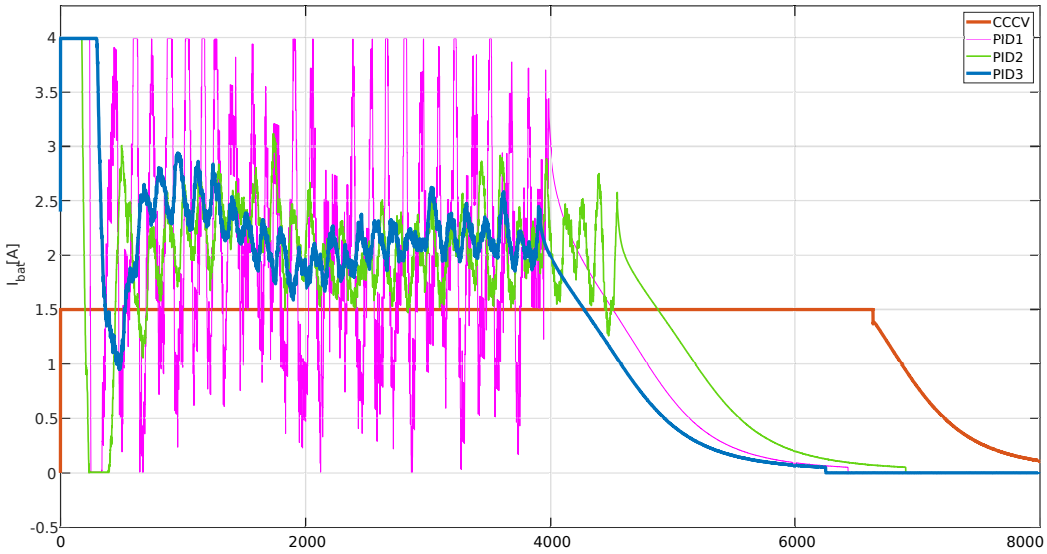


Figure 3.2: LG18650HG2 CT-CV charging current accordingly with PID tune.

The charging current results from PID tunes are shown in Figure 3.2. The small integrative and high derivative gains bring the system uncontrollable, as seen in PID1, where the oscillation peaked to the peak amplitude of 4 A. Once the integrative term is increased, and the derivative term decreases, the system starts to be controllable with a lower peak to peak charging, as seen in PID2. The observed improvement from PID1 to PID2 is not satisfactory; due to the period, the current was zero to decrease $T_s$. Zero current periods produce the flat curves in the SoC curve and increasing charging time. Hence, PID3 increased the gains once again, as observed in Table. 3.1, and this was the best tune for the PID controller.

In summary, the PID3 tune produced an overshoot of 1.2°C, a steady-state error of 0.4°C; it also presented faster charging times for the entire SoC range when compared to the other PID tunes tested. Furthermore, various PID tunes were tested at different temperatures and for BUT1, BUT2, and BUT3, and as a result, PID3 presented the best performance overall scenarios. Thus, the controller tuned with parameters PID3 is to be a general PID tune for all the subsequent CT-CV charging methodology over different ambient temperatures and with batteries.

Figures 3.3, 3.4 and 3.5 present current calculated for each term: proportional, integrative, and derivative, and also the final PID controller current used for CT-CV with PID3 tune for BUT1 . The controller charging current, which is the sum of all calculated terms, is presented along with the real charge current (i.e., 4 A limited current). Furthermore, the sampled surface temperature and the controller setpoint for each ambient temperature is shown for the controller analysis.

It can be observed from the integral term that it reduces the settling time and minimizes the steady-state surface temperature error. However, it produces a current peak produced by the PID, and it is one of the causes of overshoot. Meanwhile, the proportional current term provides a fast response to transients, as it is a direct

result of the error multiplied by the proportional gain. It starts with a non-zero value and decreases accordingly with the error amplitude. Its results are negative when the surface temperature is higher than the setpoint, which can be seen during the overshoot. Finally, the derivative current term helps reduce the overshoot, since it becomes negative before the overshoot happens. Additionally, the derivative term is essential to decrease the settling time. So, the final charging current is the sum result of all the calculated terms, and its optimal tune will have the best trade-off between rise-time, settling-time, overshoot, and steady-state error.

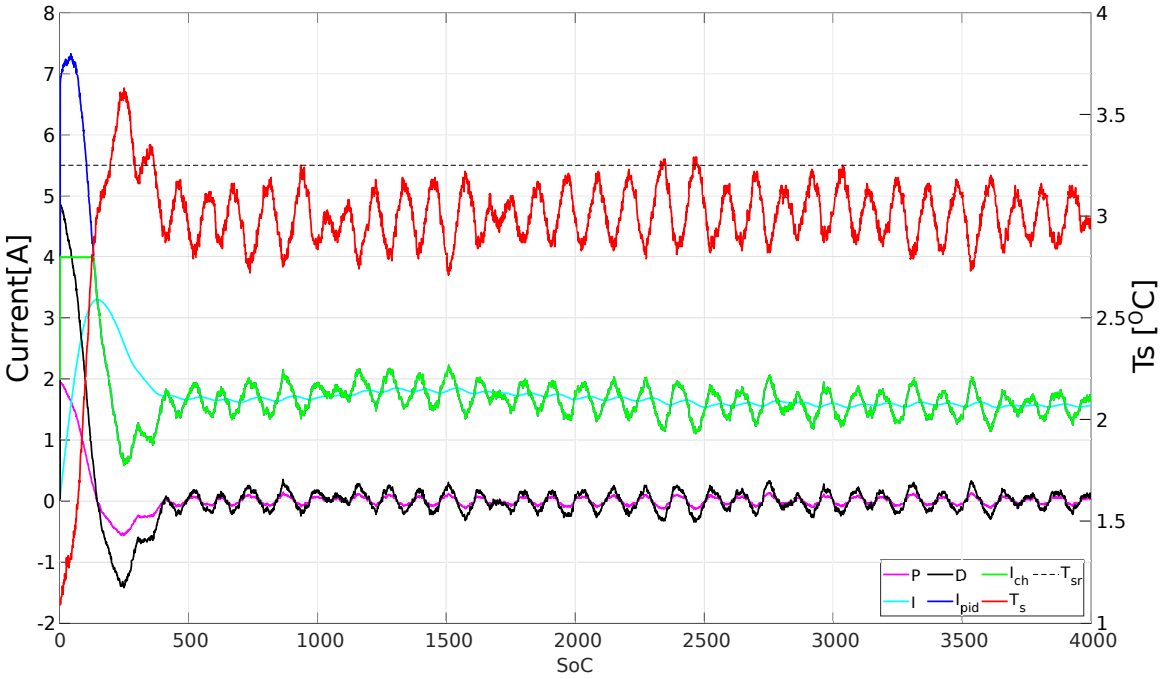


Figure 3.3: LG18650HG2 at 0°C PID controller gains profiles. $T_{sr}$ the reference temperature and control target in steady-state.

At 0°C the $T_s$ rise time and settling time is very fast and happens around approximately 600 seconds. The integrative current term starts at zero and increases to its peak, where it has a higher peak than other terms. Meanwhile, the proportional and derivative terms start with higher values and decrease as the error is reduced. It can also be observed that proportional and derivative terms introduce the oscillation seem

in the charging current. The temperature chamber cooling system causes this oscillation. Finally, the steady-state current is slightly below 2 A, and the steady-state surface temperature error is very close to the reference.

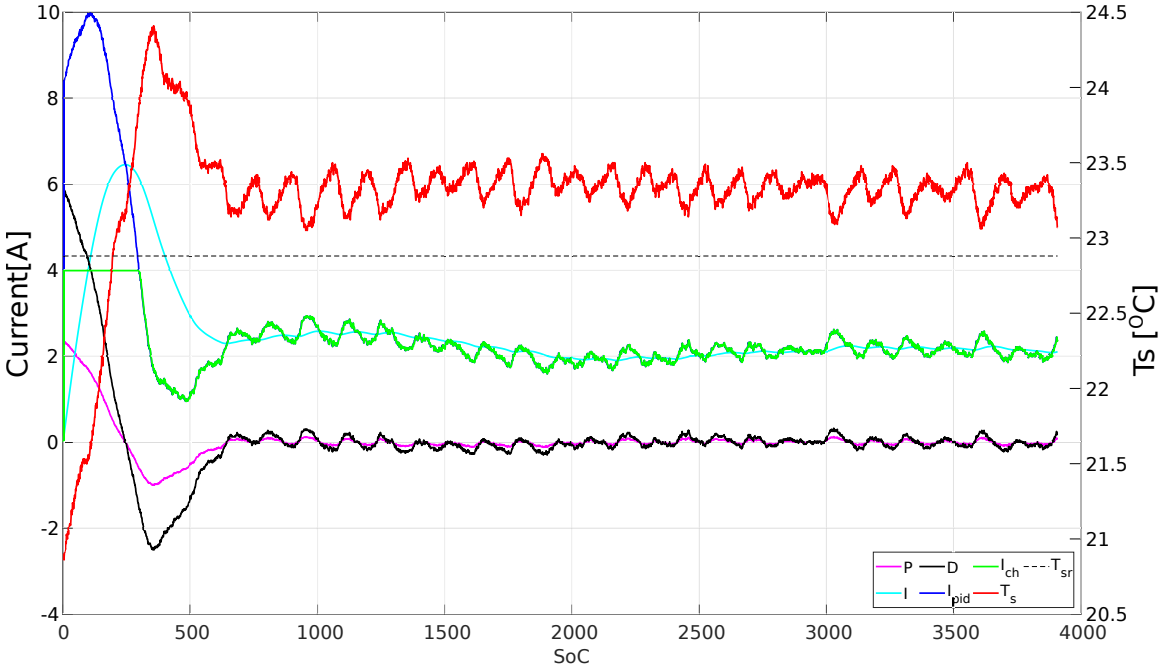


Figure 3.4: LG18650HG2 at 20°C PID controller gains profiles. $T_{sr}$ the reference temperature and control target in steady-state.

Similar oscillation is seen on the surface temperature, and currents at 0°C can be observed at 20°C. However, the oscillation amplitude is lower, since the temperature chamber needs less cooling effort to maintain the temperature. At 20°C, the surface temperature takes more than 500 seconds to achieve zero steady-state error. Also, it is noticed a higher overshoot at 20°C, while the derivative term higher effort to reduce it, as it can be observed on the negative portion of the derivative current term. The steady-state current is very close to 2 A, producing a steady-state error of less than 0.5°C.

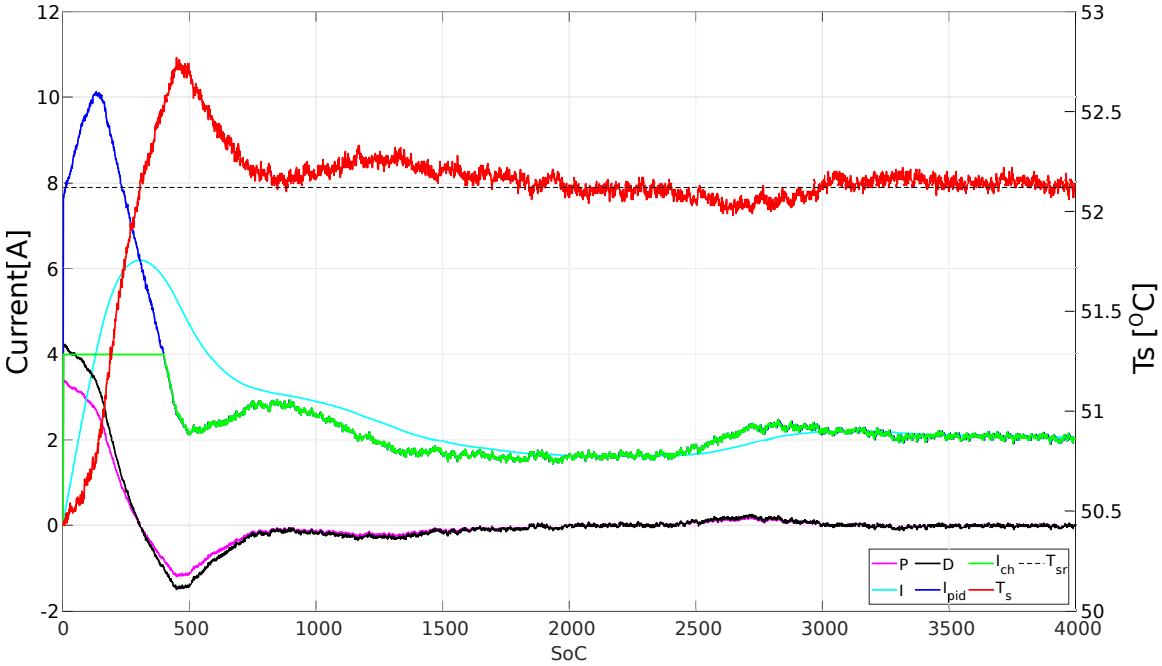


Figure 3.5: LG18650HG2 at 50°C PID controller gains profiles. $T_{sr}$ the reference temperature and control target in steady-state.

At 50°C, no oscillation caused by the cooling system of the temperature chamber is observed, as it is not needed. The transient response takes approximately 800 seconds to achieve the steady-state. It can be observed that the proportional and derivative terms were similar to each other during the transient and steady-state. The overshoot is slightly above 0.5°C. It can be seen the average current being above 2 A for most of the charging time.

In summary, the PID response for 0°C, 20°C and 50°C for BUT1 using PID3 tune is excellent. Also, similar results were obtained with BUT2 and BUT3 using the same scenario. The ambient temperature increase resulted in more extended surface temperature settling time, which resulted in a longer period of time with fast charging current characteristics, reduced overall charging time, and partial charging time to determined SoC. This is expected since the lower temperatures produce higher internal resistances, as seem in Chapter 2. Finally, this PID3 tune will be used

in the following CT-CV charging methodology tests to be compared with CC-CV methodology.

## 3.2 Charging Methodologies

The battery tests have to be performed with the same environmental conditions to compare different charging methodologies; otherwise the results can be influenced. As discussed in Chapter 2, the charging tests are performed with a thermal chamber, which maintains the ambient temperature $T_a$ constant at 0°C, 20°C or 50°C. Moreover, the charging currents and voltages are limited by the manufacturing datasheet, where fast charging specifications are used as maximum limits for CT-CV method, and standard charging specifications are used as limits CC-CV method. However, the main point is that CC-CV will produce a $T_s$ rise, and its maximum value will be used as limitation for the $T_s$ rise during CT-CV method.

During the CT-CV tests, the variable charging current produces an irregular SoC curve with different slopes. First, with a steeper slope is observed, due to higher current allowed to reduce $T_s$ rise time. It is followed by a slightly flatter slope representing the lower current to compensate $T_s$ overshoot. After reaching $T_s$ steady-state setpoint, the current does not change significantly, resulting in a slightly steep slope until it reaches the CV phase.

The CT-CV method results in a more considerable voltage increase compared to the CC-CV method during the initial charge. This voltage spike is related to the higher current at the early charging stage, which produces a voltage buildup due to the battery's internal resistance. After $T_s$ reaches the steady-state setpoint, the charge current drops allowing the battery voltage to relax and decrease.

The CC-CV and CT-CV methodologies results found in this work are presented

with the figures with the same standard and sizes, showing battery voltage $V_{bat}$: [V], battery current: $I_{bat}$ [A], SoC: [%], ambient temperature ($T_a$), and surface temperature ($T_s$): Temp.[$^oC$]. All figures have the same x-axis time scale of 10,000 seconds, so it is easier for a visual comparison. The SoC calculation is being based on the maximum capacity measured during the charge, and it is done separately for each method.

### 3.2.1 Scenario 1: BUT1 INR18650HG2

The scenario is composed of testing one BUT1: INR18650HG2 at different $T_a$. The results are used to study the behavior of the proposed charging technique with the conventional CC-CV method.

**Case 1: Ambient temperature: 0°C results**

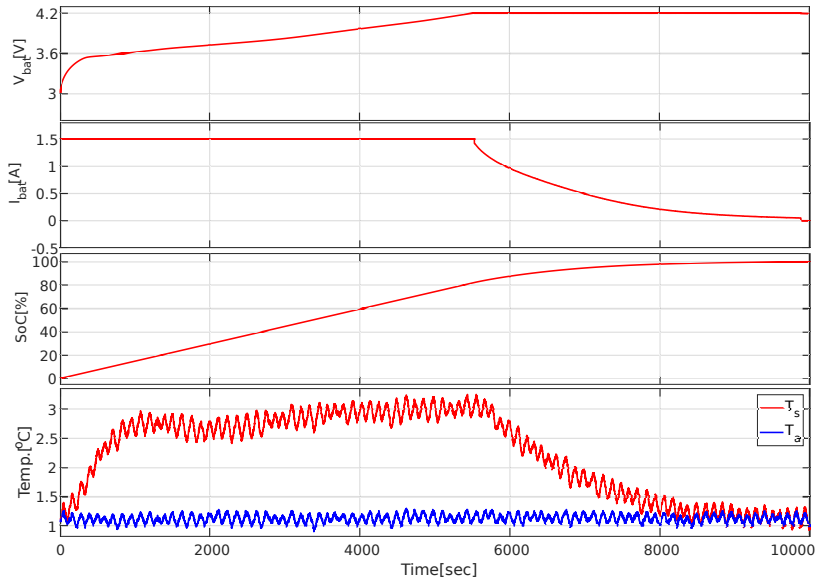


Figure 3.6: CC-CV LG18650HG2 at 0°C battery voltage, current, SoC, surface and ambient temperature profiles.

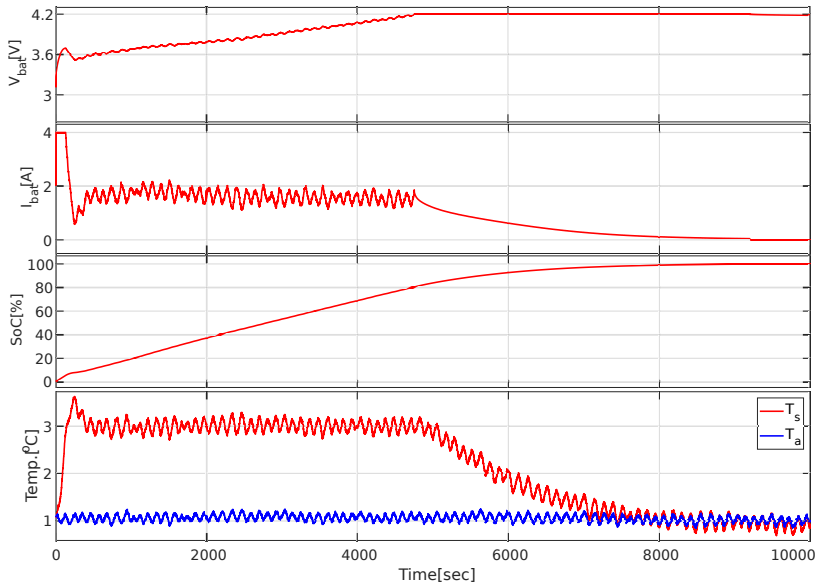


Figure 3.7: CT-CV LG18650HG2 at 0°C battery voltage, current, SoC, surface and ambient temperature profiles.

CC-CV test results for BUT1 at 0°C are shown in Figure 3.6. The constant current of 1.5 A produces a variable $T_s$ curve during the entire charging phase, where the maximum $T_s$ is 3.3°C, and it is measured at approximately 5500 seconds.

Figure 3.7 shows the CT-CV test results for BUT1 at 0°C. The maximum $T_s$ of 3.3°C measured in CC-CV test is used as set point. The rise-time is achieved in less than 150 seconds, with an overshoot of 0.6°C. Moreover, the settling time is around 350 seconds, and -0.2°C steady-state error is present.

Table 3.2 shows the charging time results in seconds for various SoC points, and also for the time it reaches the CV phase. The superiority in charging time of CT-CV over CC-CV for BUT1 is evident, with charging improvements over 7% for the entire SoC range, and peak improvement of 15% from 0% to 60% SoC range.

Table 3.2: LG18650HG2 at 00°C charging times for specific SoC values and for CV, with its respective charging time improvement.

| **SoC** | **20%** | **40%** | **60%** | **80%** | **CV** | **100%** |
|---|---|---|---|---|---|---|
| **CC-CV [sec]** | 1343 | 2688 | 4033 | 5379 | 5497 | 9887 |
| **CT-CV [sec]** | 1038 | 2171 | 3430 | 4721 | 4757 | 9206 |
| **Improvement** | 23% | 19% | 15% | 12% | 13% | 7% |

**Case 2: Ambient temperature: 20°C results**

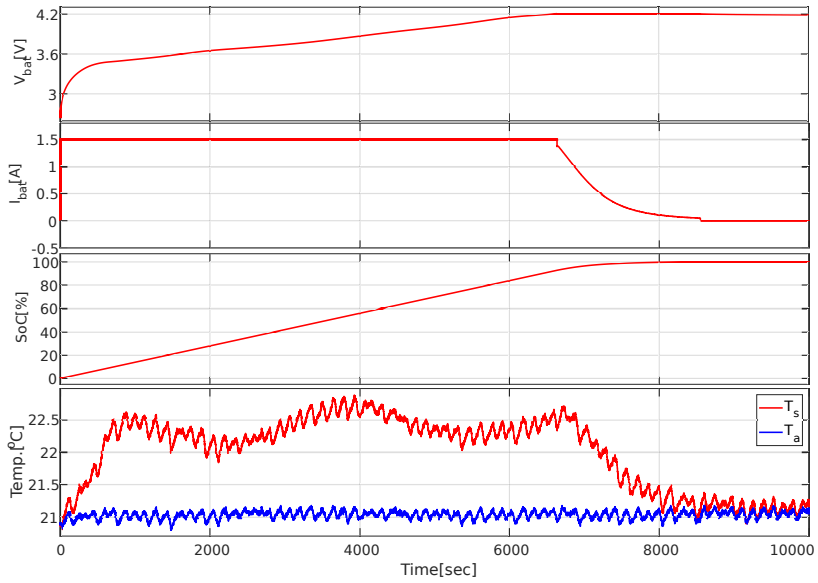


Figure 3.8: CC-CV LG18650HG2 at 20°C battery voltage, current, SoC, surface and ambient temperature profiles.

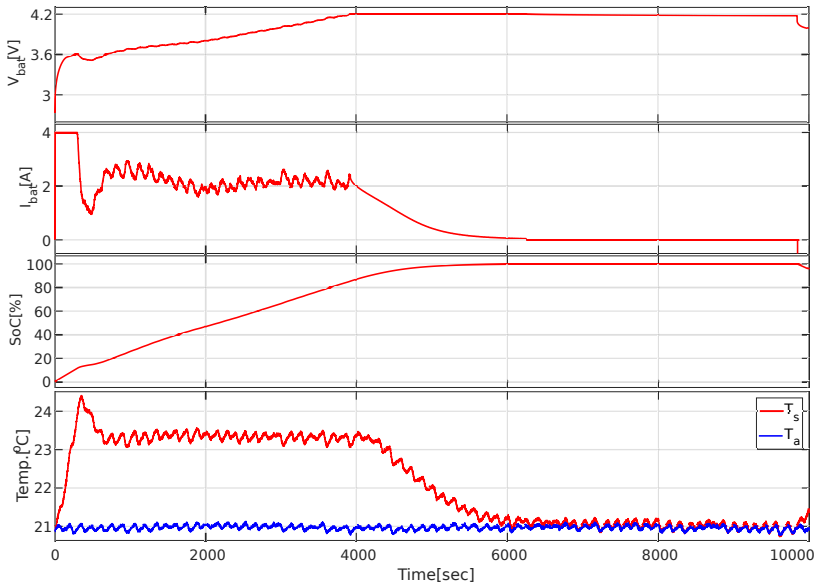


Figure 3.9: CT-CV LG18650HG2 at 20°C battery voltage, current, SoC, surface and ambient temperature profiles.

CC-CV test results for BUT1 at 20°C are shown in Figure 3.8. The constant current of 1.5 A produces a variable $T_s$ curve during the entire charging phase, where the maximum $T_s$ is 22.9°C, and it is measured at approximately 4000 seconds.

Figure 3.9 shows the CT-CV test results for BUT1 at 20°C. The maximum $T_s$ of 22.9°C measured in CC-CV test is used as set point. The rise-time is achieved in less than 500 seconds, with an overshoot of 1.1°C. Moreover, the settling time is around 300 seconds, and 0.4°C steady-state error is present.

Table 3.3 shows the charging time results in seconds for various SoC points, and also for the time it reaches the CV phase. The superiority in charging time of CT-CV over CC-CV for BUT1 is evident, with charging improvements over 27% for the entire SoC range and peak improvement of 36% from 0% to 80% SoC range.

Table 3.3: LG18650HG2 at 20°C charging times for specific SoC values and for CV, with its respective charging time improvement.

| **SoC** | **20%** | **40%** | **60%** | **80%** | **CV** | **100%** |
|---|---|---|---|---|---|---|
| **CC-CV [sec]** | 1430 | 2860 | 4290 | 5720 | 6591 | 8567 |
| **CT-CV [sec]** | 774 | 1636 | 2687 | 3643 | 3906 | 6265 |
| **Improvement** | 46% | 43% | 37% | 36% | 41% | 27% |

**Case 3: Ambient temperature: 50°C results**

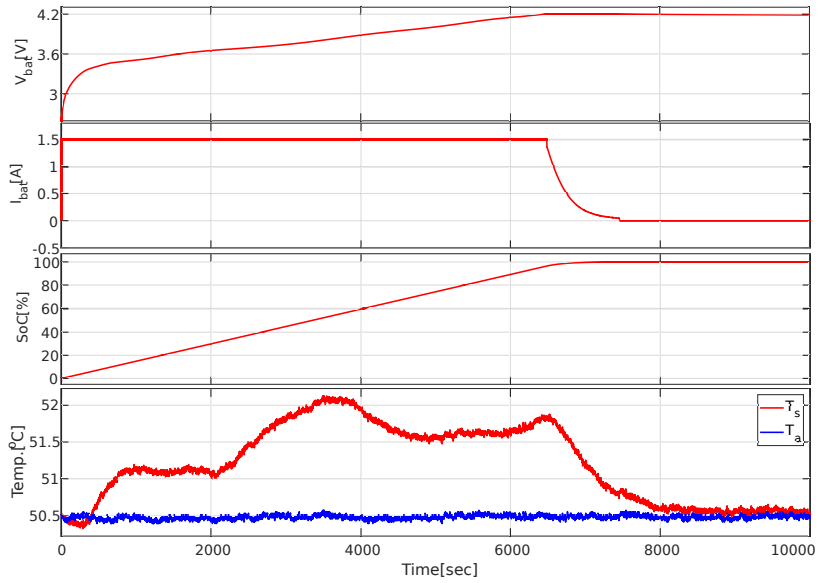


Figure 3.10: CC-CV LG18650HG2 at 50°C battery voltage, current, SoC, surface and ambient temperature profiles.

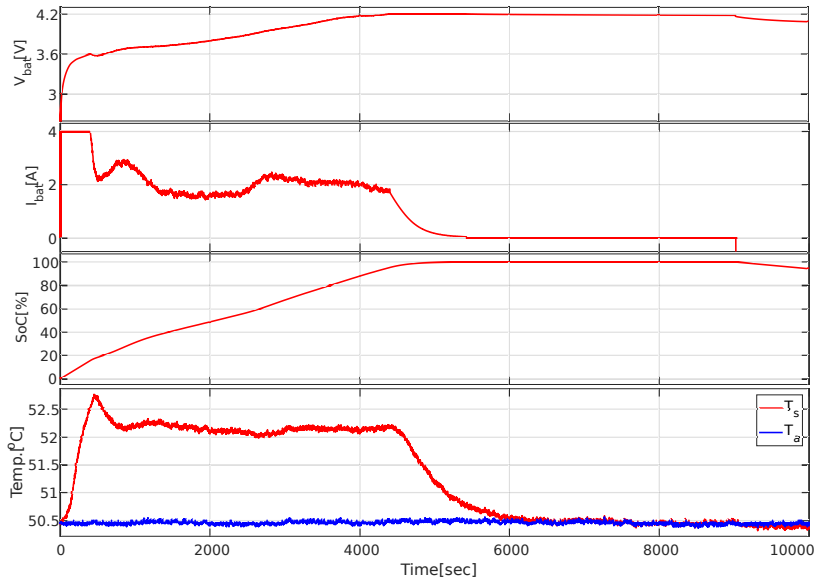


Figure 3.11: CT-CV LG18650HG2 at 50°C battery voltage, current, SoC, surface and ambient temperature profiles.

CC-CV test results for BUT1 at 50°C are shown in Figure 3.10. The constant current of 1.5 A produces a variable $T_s$ curve during the entire charging phase, where the maximum $T_s$ is 52.1°C, and it is measured at approximately 3750 seconds. It is observed the change from endothermic to exothermic during the first 150 seconds, where the $T_s$ drops below $T_a$.

Figure 3.11 shows the CT-CV test results for BUT2 at 50°C. The maximum $T_s$ of 52.1°C measured in CC-CV test is used as set point. The rise-time is achieved in less than 500 seconds, with an overshoot of 0.64°C. Moreover, the settling time is around 600 seconds and a zero steady-state error.

Table 3.4 shows the charging time results in seconds for various SoC points, and also for the time it reaches the CV phase. The superiority in charging time of CT-CV over CC-CV for BUT1 is evident, with charging improvements over 27% for the entire SoC range and peak improvement of 46% from 0% to 40% SoC range.

Table 3.4: LG18650HG2 at 50°C charging times for specific SoC values and for CV, with its respective charging time improvement.

| **SoC** | **20%** | **40%** | **60%** | **80%** | **CV** | **100%** |
|---|---|---|---|---|---|---|
| **CC-CV [sec]** | 1344 | 2689 | 4034 | 5379 | 6462 | 7459 |
| **CT-CV [sec]** | 575 | 1448 | 2666 | 3603 | 4388 | 5428 |
| **Improvement** | 57% | 46% | 34% | 33% | 32% | 27% |

### 3.2.2 Scenario 2: BUT2 INR18650HE4

The scenario is composed of testing one BUT2: INR18650HE4 at different $T_a$. The results are used to study the behavior of the proposed charging technique with the conventional CC-CV method.

**Case 1: Ambient temperature: 0°C results**

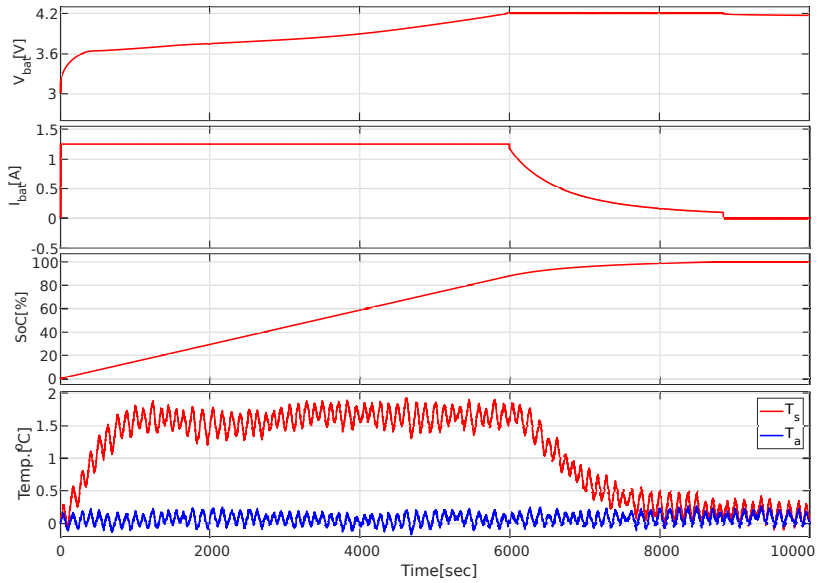


Figure 3.12: CC-CV LG18650HE4 at 0°C battery voltage, current, SoC, surface and ambient temperature profiles.

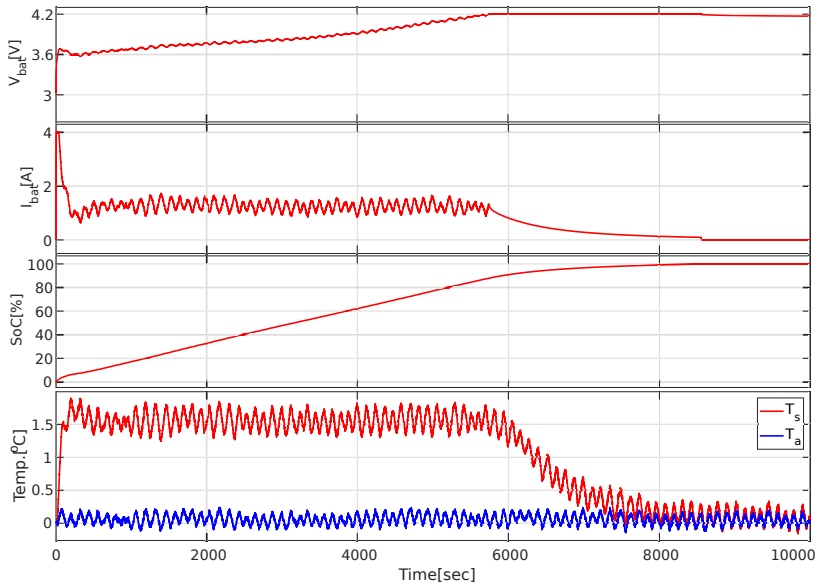


Figure 3.13: CT-CV LG18650HE4 at 0°C battery voltage, current, SoC, surface and ambient temperature profiles.

CC-CV method test results for BUT2 at 0°C are shown in Figure 3.12. The constant current of 1.25 A produces a $T_s$ rise, which takes approximately 1200 seconds to achieve maximum temperature of 1.9°C.

Figure 3.13 shows the CT-CV method test results for BUT2 at 0°C. The PID controller sets the charging current, where the 1.9°C maximum $T_s$ reached in CC-CV method is used as setpoint. The rise-time achieves in less than 150 seconds, with an overshoot of approximately 0.3°C. The settling time is around 250 seconds, and -0.4°C steady-state error is found.

Table 3.5 shows the charging time results in seconds for various SoC points, and also for the time it reaches the CV phase. The charging time improved in all points, with peak improvement being of 11%, and overall improvement during the entire range being 3%.

Table 3.5: LG18650HE4 at 0°C charging times for specific SoC values and for CV, with its respective charging time improvement.

| **SoC** | **20%** | **40%** | **60%** | **80%** | **CV** | **100%** |
|---|---|---|---|---|---|---|
| **CC-CV [sec]** | 1362 | 2724 | 4086 | 5449 | 5970 | 8852 |
| **CT-CV [sec]** | 1207 | 2481 | 3849 | 5197 | 5740 | 8574 |
| **Improvement** | 11% | 9% | 6% | 5% | 4% | 3% |

**Case 2: Ambient temperature: 20°C results**

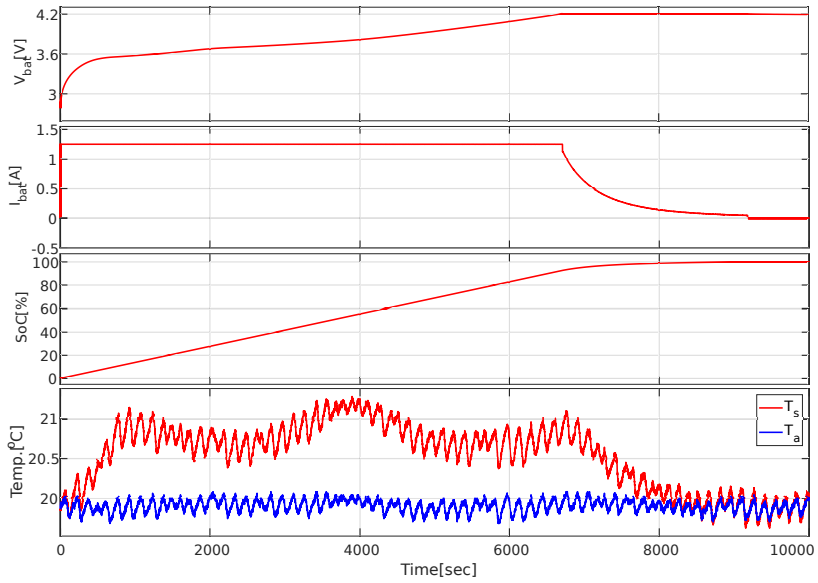


Figure 3.14: CC-CV LG18650HE4 at 20°C battery voltage, current, SoC, surface and ambient temperature profiles.

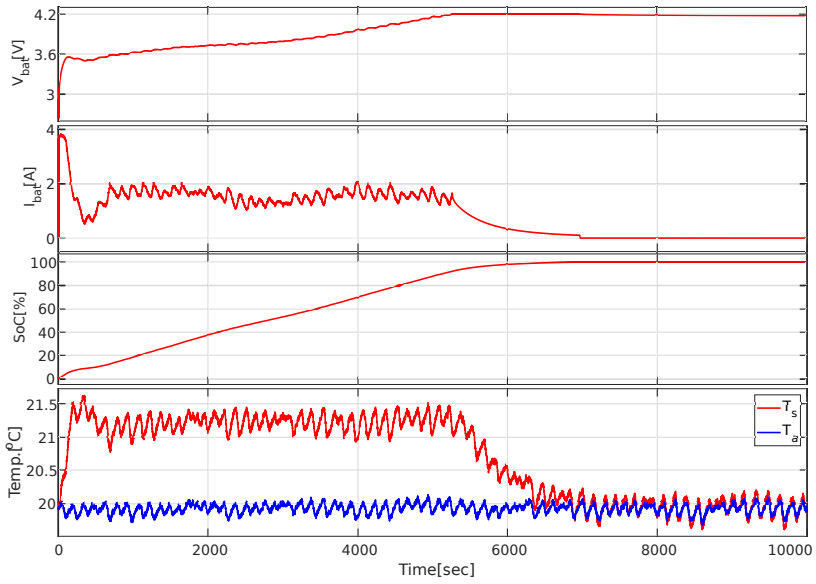


Figure 3.15: CT-CV LG18650HE4 at 20°C battery voltage, current, SoC, surface and ambient temperature profiles.

CC-CV method test results for BUT2 at 20°C are shown in Figure 3.14. The constant current of 1.25 A produces a $T_s$ rise, which takes approximately 1000 seconds to achieve maximum temperature of 21.3°C.

Figure 3.15 shows the CT-CV method test results for BUT2 at 20°C. The PID controller sets the charging current, where the 21.3°C maximum $T_s$ reached when CC-CV method is used as the setpoint. The rise-time achieved is less than 150 seconds, with an overshoot of approximately 0.4°C. Additionally, the settling time is around 500 seconds, with zero steady-state error.

Table 3.6 shows the charging time results in seconds for various SoC points, and also the time it reaches the CV phase. Also, the charging time improved in all points, with excellent results for the entire CT phase, where the improvements were higher than 20% for the entire SoC range.

Table 3.6: LG18650HE4 at 20°C charging times for specific SoC values and for CV, with its respective charging time improvement.

| **SoC** | **20%** | **40%** | **60%** | **80%** | **CV** | **100%** |
|---|---|---|---|---|---|---|
| **CC-CV [sec]** | 1447 | 2894 | 4342 | 5789 | 6684 | 9199 |
| **CT-CV [sec]** | 1078 | 2140 | 3447 | 4552 | 5258 | 6969 |
| **Improvement** | 26% | 26% | 21% | 21% | 21% | 24% |

**Case 3: Ambient temperature: 50°C results**

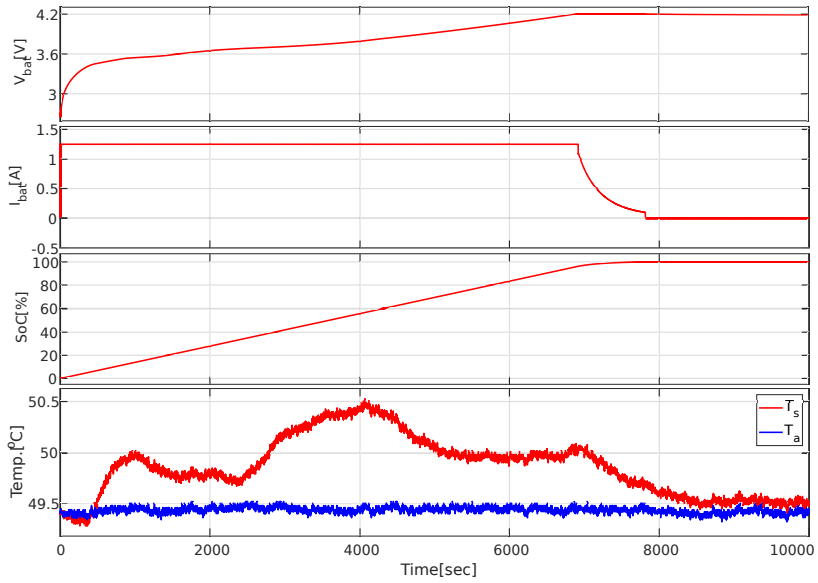


Figure 3.16: CC-CV LG18650HE4 at 50°C battery voltage, current, SoC, surface and ambient temperature profiles.

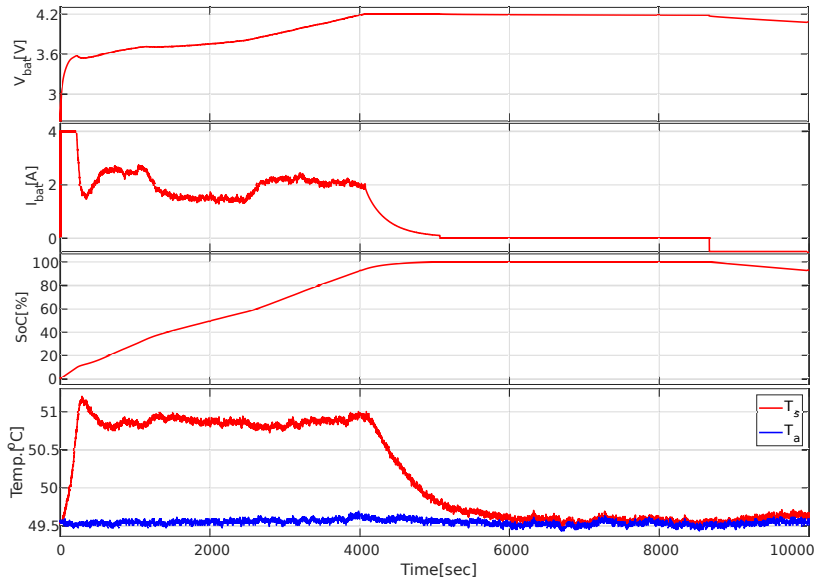


Figure 3.17: CT-CV LG18650HE4 at 50°C battery voltage, current, SoC, surface and ambient temperature profiles.

CC-CV test results for BUT2 at 50°C are shown in Figure 3.16. The constant current of 1.25 A produces a variable $T_s$ curve during the entire charging phase, where the maximum $T_s$ is 50.5°C, and it is measured at approximately 4100 seconds. A change from endothermic to exothermic heat exchange is observed during the first 250 seconds, where the $T_s$ drops below $T_a$.

Figure 3.17 shows the CT-CV test results for BUT2 at 50°C. The maximum $T_s$ of 50.5°C measured in CC-CV test is used as set point. The rise-time is achieved in less than 175 seconds, with an overshoot of 0.34°C. Moreover, the settling time is around 250 seconds and the steady-state error is 0.33°C.

Table 3.7 shows the charging time results in seconds for various SoC points, and also for the time it reaches the CV phase. The superiority in charging time of CT-CV over CC-CV for BUT2 is evident, with charging improvements over 35% for the entire SoC range and peak improvement of 50% from 0% to 40% SoC range. In addition, the higher $T_a$ increased the duration of the CC and CT phases, which resulted in a

shorter time for CV phase.

Table 3.7: LG18650HE4 at 50°C charging times for specific SoC values and for CV, with its respective charging time improvement.

| **SoC** | **20%** | **40%** | **60%** | **80%** | **CV** | **100%** |
|---|---|---|---|---|---|---|
| **CC-CV [sec]** | 1437 | 2875 | 4313 | 5752 | 6893 | 7819 |
| **CT-CV [sec]** | 654 | 1433 | 2626 | 3454 | 4064 | 5073 |
| **Improvement** | 54% | 50% | 39% | 40% | 41% | 35% |

### 3.2.3 Scenario 3: BUT3 SAMSUNGQ30

The scenario is composed of testing one BUT3: SAMSUNGQ30 at different $T_a$. The results are used to study the behavior of the proposed charging technique with the conventional CC-CV method.

**Case 1: Ambient temperature: 0°C results**

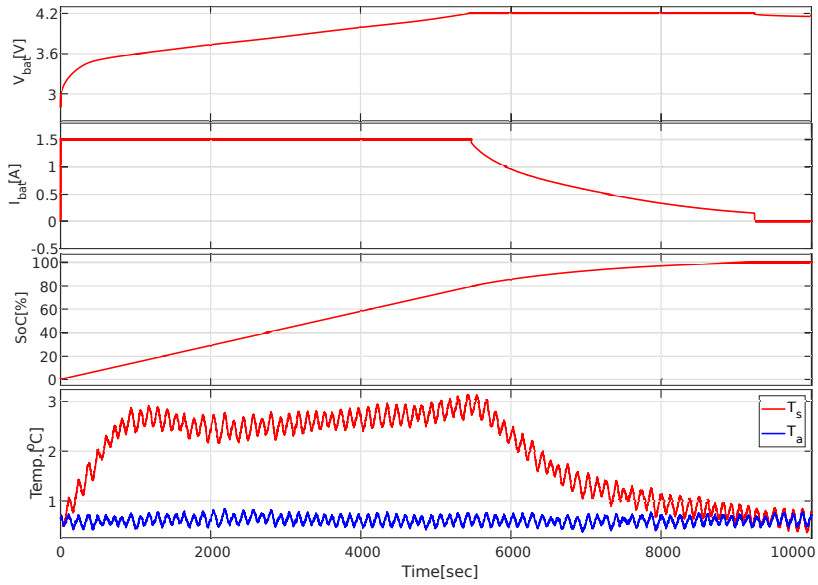


Figure 3.18: CC-CV Samsung 30Q at 0°C battery voltage, current, SoC, surface and ambient temperature profiles.

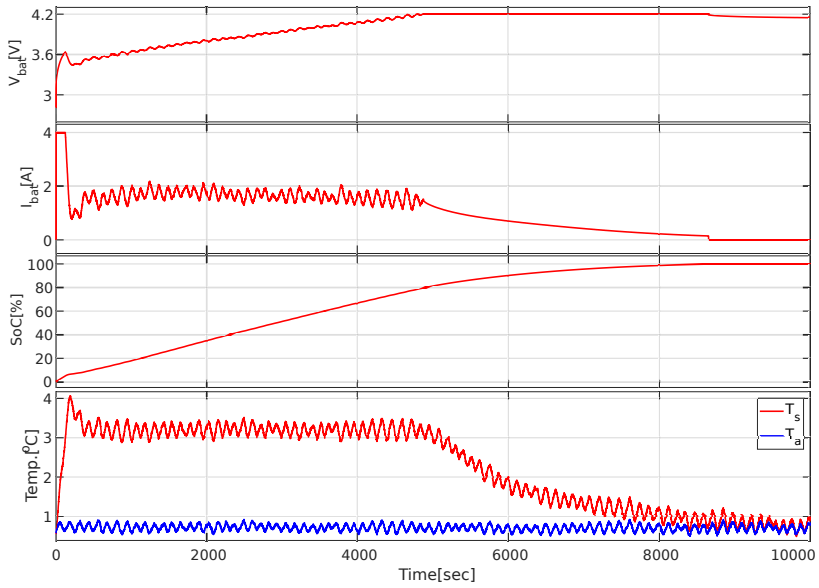


Figure 3.19: CT-CV Samsung 30Q at 0°C battery voltage, current, SoC, surface and ambient temperature profiles.

CC-CV method test results for BUT3 at 0°C are shown in Figure 3.18. The constant current of 1.5 A produces a $T_s$ rise, which takes approximately 1000 seconds to achieve thermal equilibrium. In addition, the maximum temperature is found by the end of the CC phase, and it is approximately 3°C. At the end of the CV phase $T_s$ is at equilibrium with $T_a$.

Figure 3.19 shows the CT-CV method test results for BUT3 at 0°C. The PID controller sets the charging current, where the 3°C maximum $T_s$ reached when CC-CV method is used as setpoint. The rise-time achieved is less than 200 seconds, with an overshoot of approximately 1°C. Furthermore, the settling time is around 400 seconds, and the steady-state error is less than 0.1°C.

Table 3.8 shows the charging time results in seconds for various SoC points, and also the time it reaches the CV phase. The CC phase ended and transitioned to CV phase before 80% SoC in both charging methodologies. That is related to the increased internal resistance of the battery at low temperatures, causing a higher

voltage increase during charge, thus higher battery voltage.

The CT-CV method had an overall charging improvement, where, from 0% to 60%, the charging improvement is greater than 14%, while maintaining the same $T_s$ rise for both charging methodologies.

Table 3.8: Samsung 30Q at 0°C charging times for specific SoC values and for CV, with its respective charging time improvement.

| **SoC** | **20%** | **40%** | **60%** | **80%** | **CV** | **100%** |
|---|---|---|---|---|---|---|
| **CC-CV [sec]** | 1373 | 2747 | 4121 | 5496 | 5445 | 9245 |
| **CT-CV [sec]** | 1137 | 2305 | 3558 | 4897 | 4788 | 8659 |
| **Improvement** | 17% | 16% | 14% | 11% | 12% | 6% |

**Case 2: Ambient temperature: 20°C results**

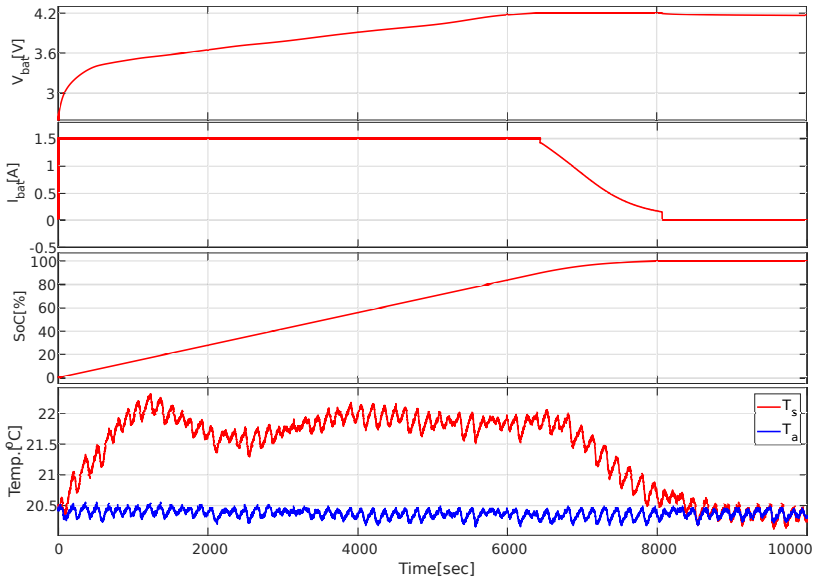


Figure 3.20: CC-CV Samsung 30Q at 20°C battery voltage, current, SoC, surface and ambient temperature profiles.

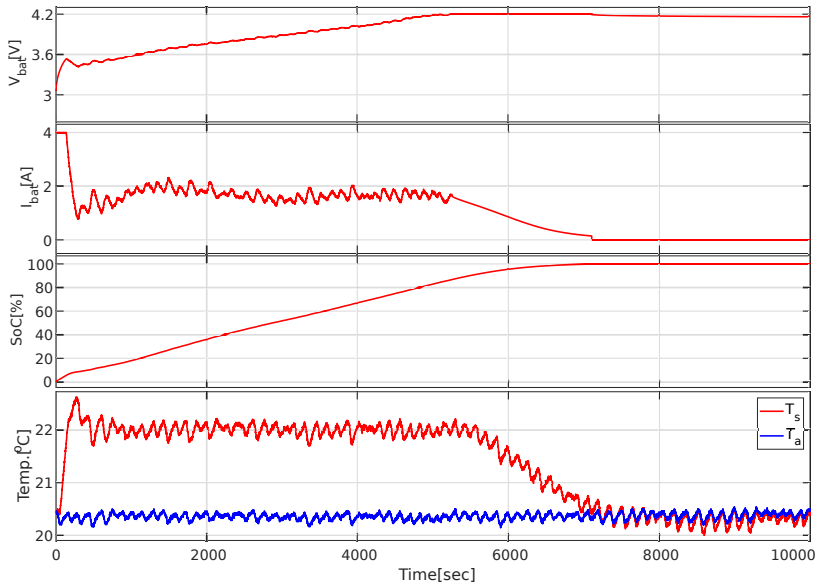


Figure 3.21: CT-CV Samsung 30Q at 20°C battery voltage, current, SoC, surface and ambient temperature profiles.

CC-CV method test results for BUT3 at 20°C are shown in Figure 3.20. The constant current of 1.5 A produces a $T_s$ rise, which takes approximately 1000 seconds to achieve maximum temperature of 22.3°C.

Figure 3.21 shows the CT-CV method test results for BUT3 at 20°C. The PID controller sets the charging current, where the 22.3°C maximum $T_s$ reached when CC-CV method is used as setpoint. The rise-time achieved is less than 150 seconds, with an overshoot of approximately 0.5°C. Also, the settling time is around 250 seconds, and the steady-state error is -0.3°C, where the negative value means the steady-state $T_s$ is lower than reference.

Table 3.9 shows the charging time results in seconds for various SoC points, and also the time it reaches the CV phase. It is observed the transition from CC to CV phase after SoC 80% for both charging methods. Also, the charging time improved in all points, with excellent results for the entire CT phase, where the improvements were higher than 16%.

Table 3.9: Samsung 30Q at 20°C charging times for specific SoC values and for CV, with its respective charging time improvement.

| **SoC** | **20%** | **40%** | **60%** | **80%** | **CV** | **100%** |
|---|---|---|---|---|---|---|
| **CC-CV [sec]** | 1433 | 2866 | 4299 | 5733 | 6369 | 8070 |
| **CT-CV [sec]** | 1126 | 2236 | 3561 | 4814 | 5230 | 7109 |
| **Improvement** | 21% | 22% | 17% | 16% | 18% | 12% |

**Case 3: Ambient temperature: 50°C results**

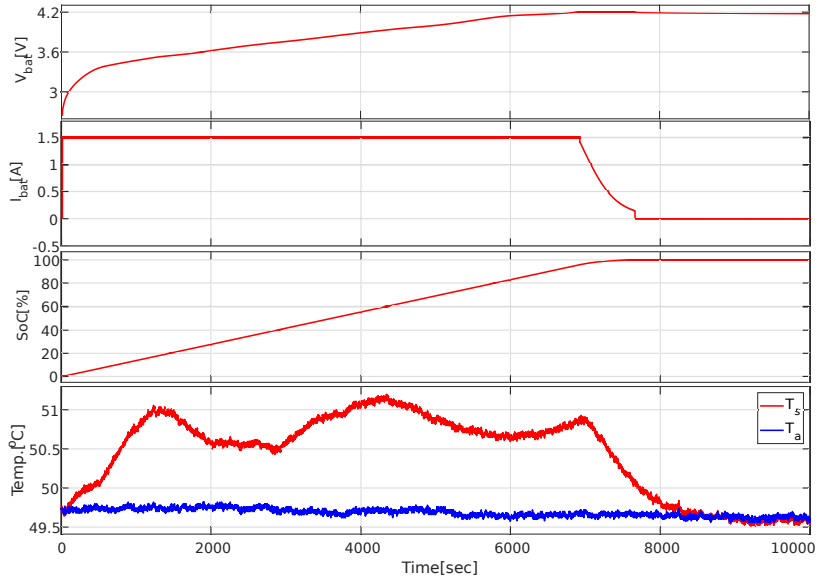


Figure 3.22: CC-CV Samsung 30Q at 50°C battery voltage, current, SoC, surface and ambient temperature profiles.

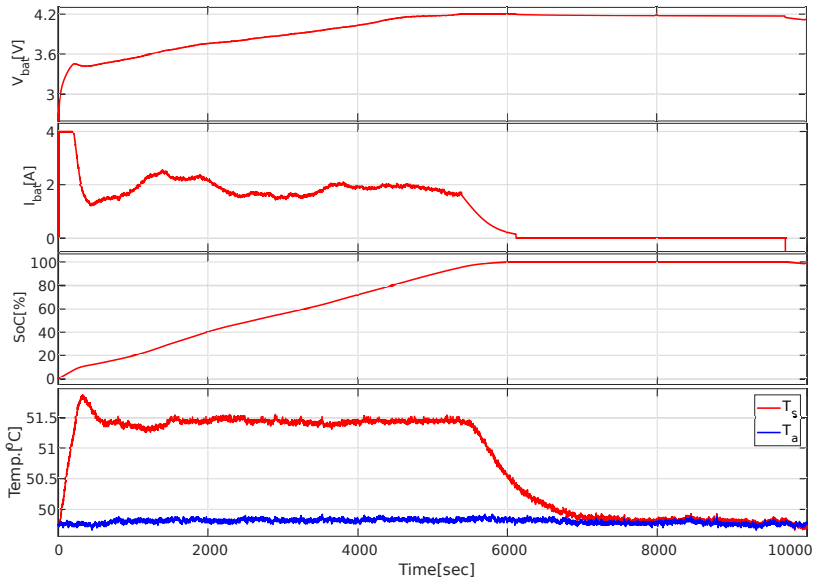


Figure 3.23: CT-CV Samsung 30Q at 50°C battery voltage, current, SoC, surface and ambient temperature profiles.

CC-CV test results for BUT3 at 50°C are shown in Figure 3.22. The constant current of 1.5 A produces a variable $T_s$ curve during the entire charging phase, where the maximum $T_s$ is 51.2°C, and it is measured at approximately 4200 seconds.

Figure 3.23 shows the CT-CV test results for BUT3 at 50°C. The maximum $T_s$ of 51.2°C is measured in CC-CV test is used as set point. The rise-time is achieved in less than 150 seconds, with an overshoot of 0.42°C. In addition, the settling time is around 250 seconds and the steady-state error is 0.24°C.

Table 3.10 shows the charging time results in seconds for various SoC points, and also the time it reaches the CV phase. It is evident superiority in charging time of CT-CV over CC-CV, with charging improvements over 20% for the entire SoC range. In addition, the higher $T_a$ increased the duration of the CC and CT phases, which resulted in a shorter time for CV phase.

Table 3.10: Samsung 30Q at 50°C charging times for specific SoC values and for CV, with its respective charging time improvement.

| **SoC** | **20%** | **40%** | **60%** | **80%** | **CV** | **100%** |
|---|---|---|---|---|---|---|
| **CC-CV [sec]** | 1454 | 2897 | 4340 | 5783 | 6896 | 7669 |
| **CT-CV [sec]** | 1020 | 1990 | 3295 | 4458 | 5361 | 6129 |
| **Improvement** | 30% | 31% | 24% | 23% | 22% | 20% |

### 3.2.4 Summary of Charging Results

All BUTs presented insufficient improvement at 0°C with the full charge improvement ranging from 3% to 7%. Meanwhile, the BUTs results at 20°C had excellent results ranging from 12% to 27% faster when fully charging the battery. Finally, the superiority of CT-CV charging over CC-CV was found at 50°C, where the full charge time improved from 20% to 35%.

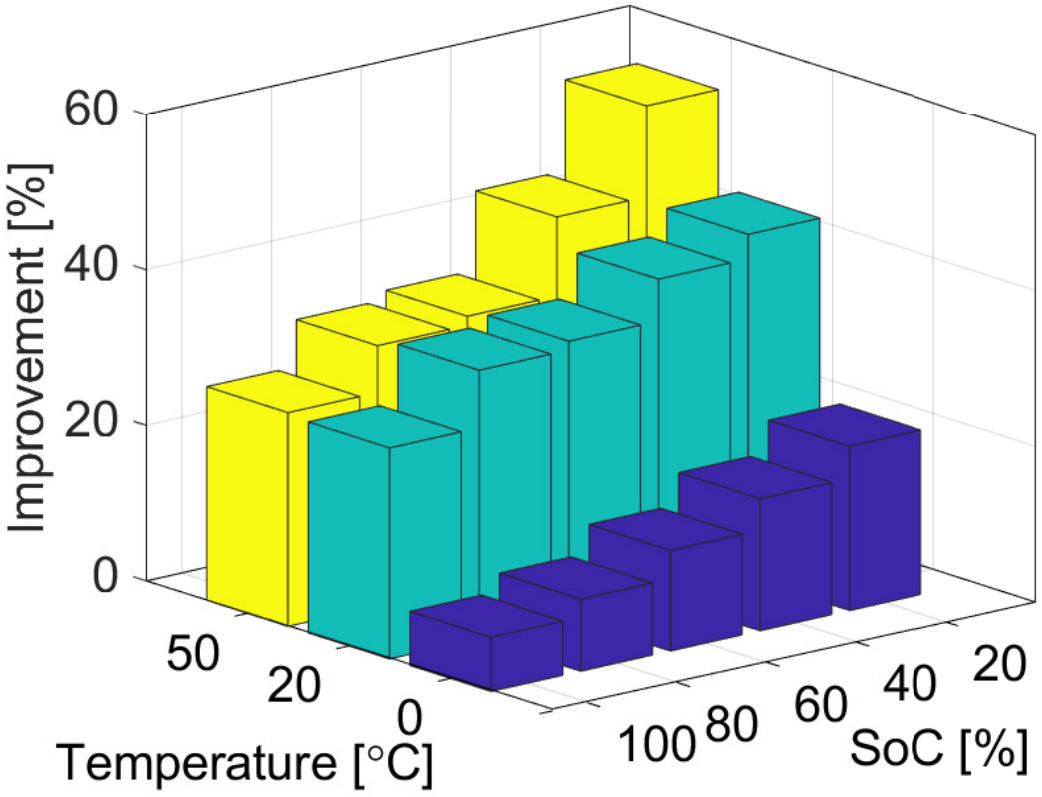


Figure 3.24: LG18650HG2 charging time improvement results for different SoC and $T_a$.

Figure 3.24 shows the charging improvements altogether for different SoC stages and $T_a$ for BUT1. It is evident that the excellent improvement at the specific point of 20% SoC and 50°C, with peak improvement of approximately 60%. Moreover, the charging performance on 20°C and 50°C is very similar overall. However, there is a considerable drop in charge performance at 50°C.

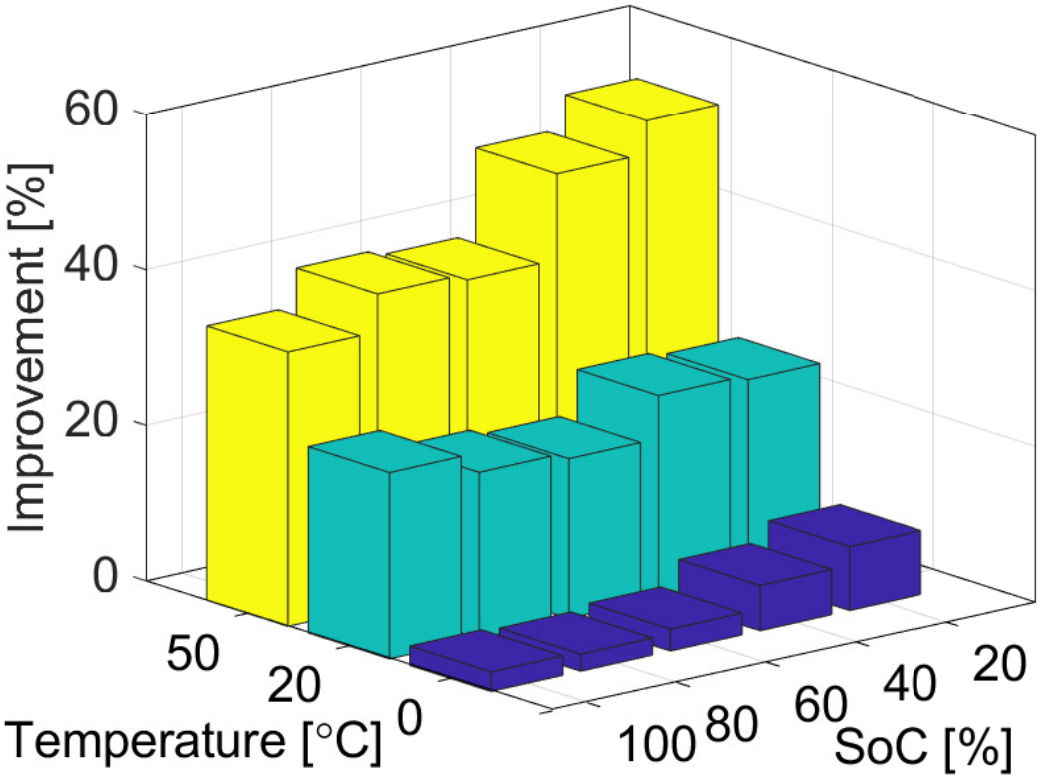


Figure 3.25: LG18650HG2 charging time improvement results for different SoC and $T_a$.

Figure 3.25 presents the charging performance for BUT2. A performance enhancement is observed with increase of $T_a$, where it has an average improvement of 5% at 0°C, 20% at 20°C and 40% charge time improvement at 50°C. Also, the improvement kept an average value near 20% for the entire SoC range when tested at $T_a$ of 20°C.

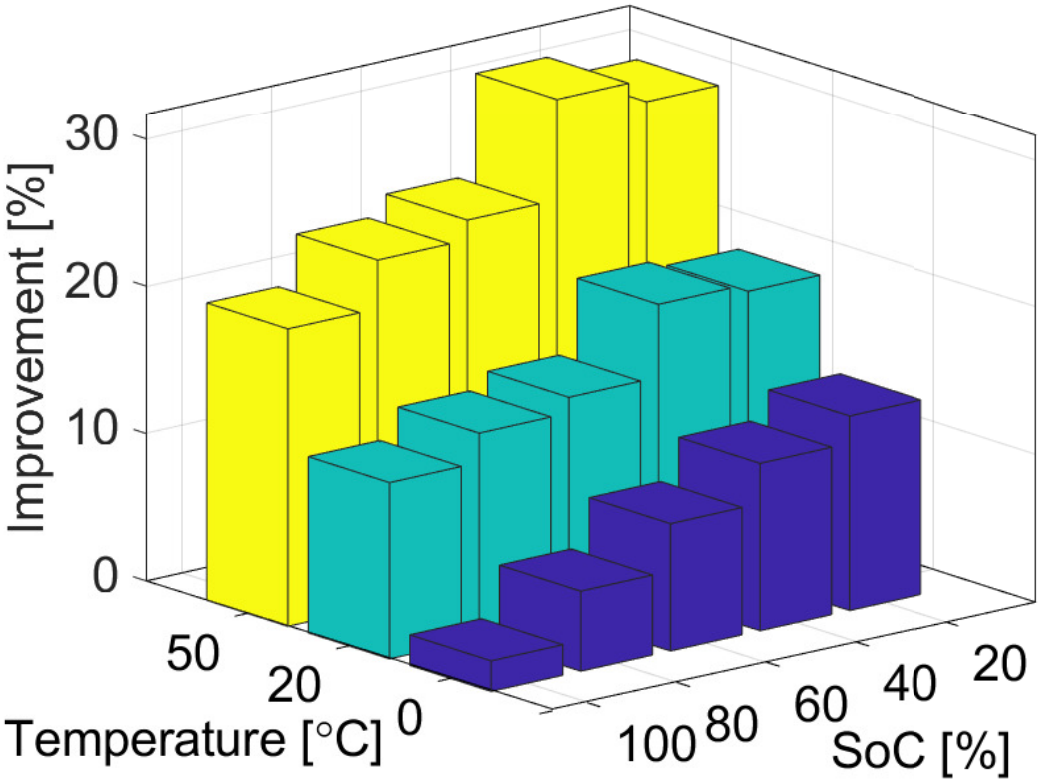


Figure 3.26: SAMSUNGQ30 charging time improvement results for different SoC and $T_a$.

BUT3 has not presented charge improvement greater than 30% at any point, as shown in Figure 3.26. Also, BUT3 does not present as good results as BUT1, which has similar specifications. However, it still had better performance when compared to the CC-CV technique.

So, CT-CV charging technique has proven to have a faster charge rate when compared to CC-CV, while maintaining the same $T_s$ rise for BUT1, BUT2 and BUT3, at different $T_a$ of 0°C, 20°C and 50°C.

## 3.3 Coulombic Efficiency Results

In order to access the coulombic efficiency (CE) performance of the CT-CV charging technique, the battery discharge is performed at constant current after each test performed in Chapter 3.2. The discharge rate is 3 A, and $V_{bat}[V]$, $I_{bat}[V]$, SoC, $T_a$ and $T_s$ profiles can be seen in Figures 3.27, 3.28, and Figure 3.29. In order to not overheat the battery, the discharge rate was reduced to 0.5 A at $T_a$ 50°C.

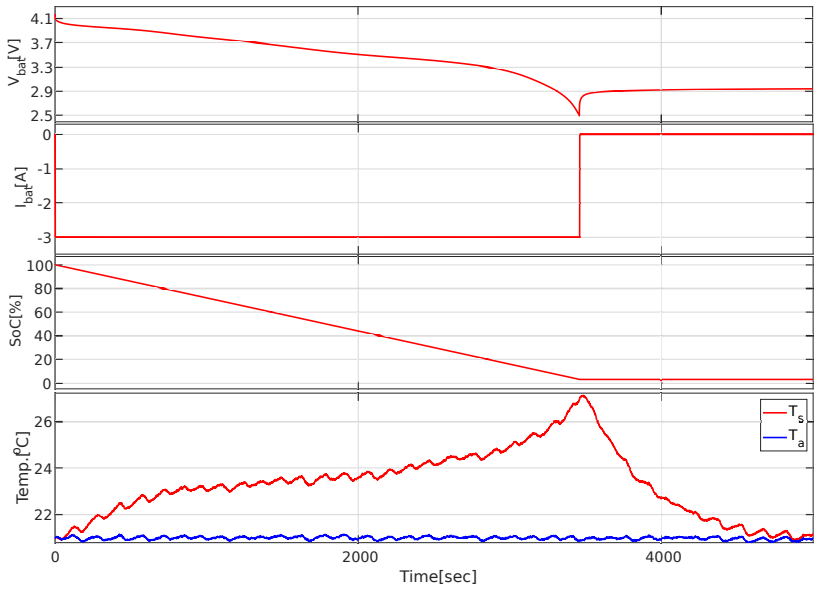


Figure 3.27: LG18650HG2 discharge profiles.

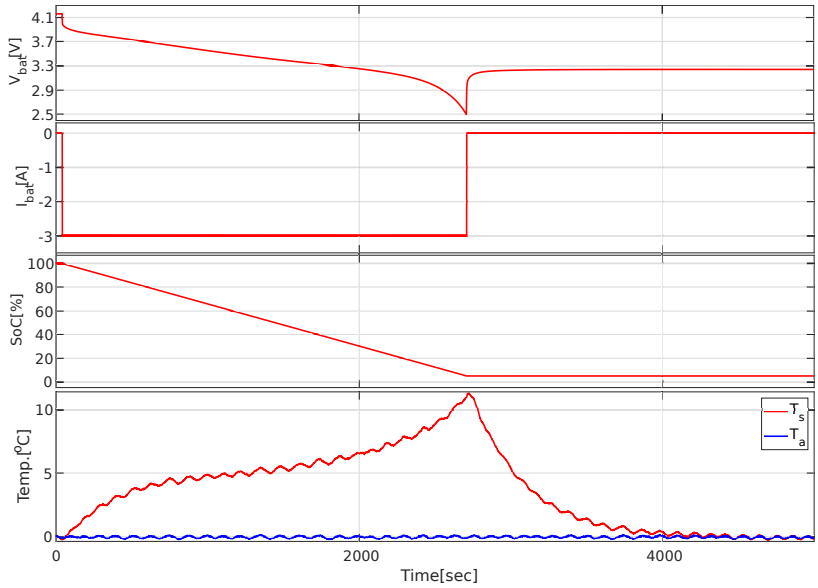


Figure 3.28: LG18650HE4 discharge profiles.

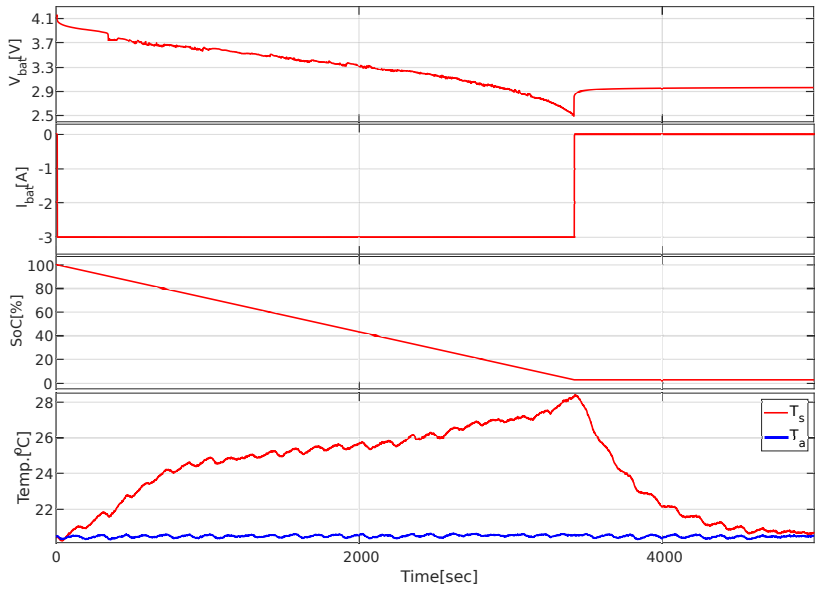


Figure 3.29: SAMSUNGQ30 discharge profiles.

All the BUTs have similar profiles for 0°C with a high $T_s$ rise, where a 11°C gradient is found between $T_a$ and $T_s$. These results are expected due to the higher internal resistances at lower SoC, and lower temperatures. For 20°C, the $T_s$ gradient with $T_a$ is around 8°C, and the peak is also present at the end of SoC.

The lower discharge current at 50°C resulted in minimum $T_s$ as expected. However, it can be observed that the $T_s$ dropping the temperature below $T_a$, as it can be seen in Figure 3.30, Figure 3.31 and Figure 3.32. This characteristic is also observed during CC-CV charging test at 50°C with BUT1 and BUT2, as it can be seen in Figures 3.10, and Figure 3.16, respectively. In general, the chemical reaction produces reversible entropy changes, which is exothermic during discharge, and endothermic during charge [55]. However, as studied in [56] the entropy change heat can be endothermic during charge, depending on the SoC range.

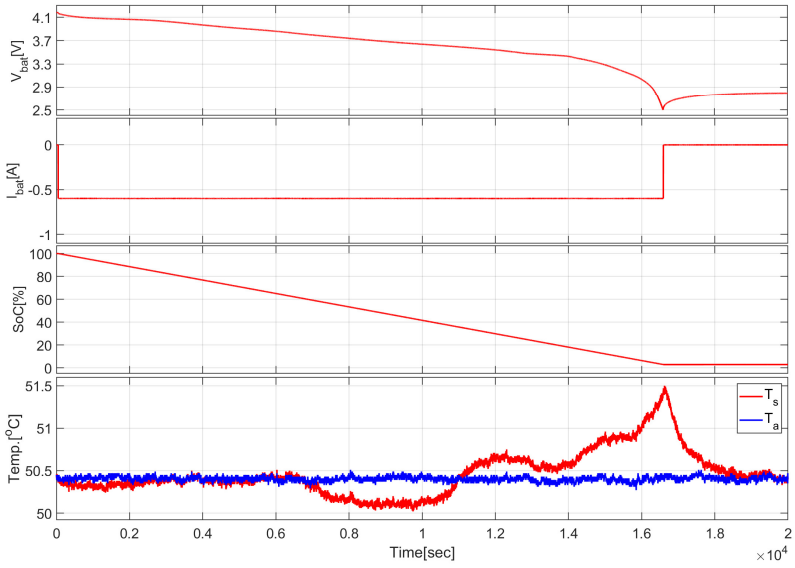


Figure 3.30: LG18650HG2 discharge profiles.

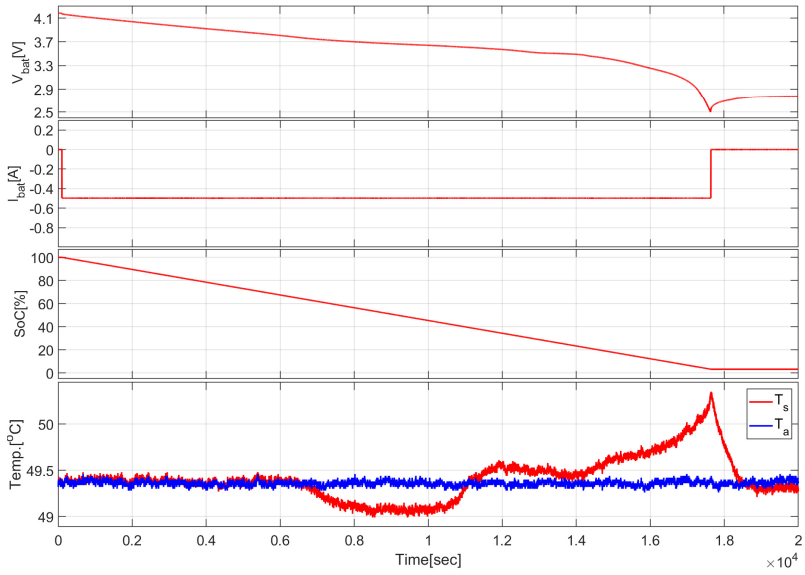


Figure 3.31: LG18650HE4 discharge profiles.

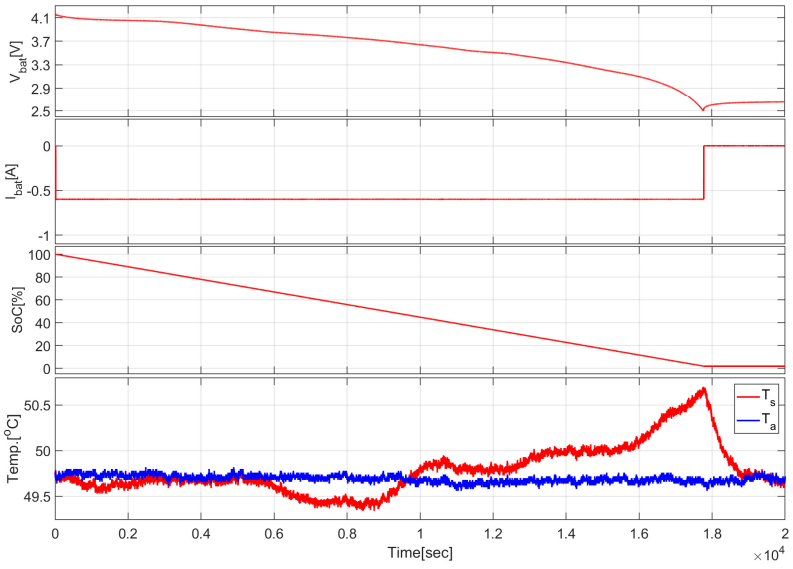


Figure 3.32: SAMSUNGQ30 discharge profiles.

Table 3.11 shows the results for the capacity measured during charge and discharge for BUT1 at various $T_a$. A variable CE is observed accordingly with the $T_a$. The variance on CE is from approximately -2% to 1%, where negative range means the CT-CV was better than CC-CV technique.

Table 3.11: LG18650HG2 measured charge and discharge capacity for various $T_a$, and respective CE results.

| | **Charge [Ah]** | **Discharge [Ah]** | **CE** | **Ta** |
|---|---|---|---|---|
| **CC-CV** | 2.8023 | 2.6748 | 95.45% | **0°C** |
| **CT-CV** | 2.7611 | 2.6658 | 96.55% | **0°C** |
| **CC-CV** | 2.9794 | 2.8817 | 96.72% | **20°C** |
| **CT-CV** | 2.9093 | 2.8232 | 97.04% | **20°C** |
| **CC-CV** | 2.8019 | 2.7747 | 99.03% | **50°C** |
| **CT-CV** | 2.8352 | 2.7497 | 96.98% | **50°C** |

Table 3.12 shows the results for the capacity measured during charge and discharge for BUT2 at various $T_a$. A variable CE is observed accordingly with the $T_a$. The variance on CE is from approximately -0.6% to 3.5%, where negative range means the CT-CV was better than CC-CV technique.

Table 3.12: LG18650HE4 measured charge and discharge capacity for various $T_a$, and respective CE results.

| | **Charge [Ah]** | **Discharge [Ah]** | **CE** | **Ta** |
|---|---|---|---|---|
| **CC-CV** | 2.3654 | 2.2217 | 93.9% | **0°C** |
| **CT-CV** | 2.3342 | 2.2757 | 97.5% | **0°C** |
| **CC-CV** | 2.5132 | 2.4665 | 98.1% | **20°C** |
| **CT-CV** | 2.5109 | 2.4474 | 97.5% | **20°C** |
| **CC-CV** | 2.4966 | 2.4243 | 97.1% | **50°C** |
| **CT-CV** | 2.5039 | 2.4205 | 96.7% | **50°C** |

Table 3.13 shows the results for the capacity measured during charge and discharge for BUT2 at various $T_a$. A variable CE is observed accordingly with the $T_a$. The

variance on CE is from approximately -0.9% to 1.7%, where negative range means the CT-CV was better than CC-CV technique.

Table 3.13: SAMSUNGQ30 measured charge and discharge capacity for various $T_a$, and respective CE results.

| | **Charge [Ah]** | **Discharge [Ah]** | **CE** | **Ta** |
|---|---|---|---|---|
| **CC-CV** | 2.8620 | 2.7658 | 96.6% | **0°C** |
| **CT-CV** | 2.8566 | 2.8091 | 98.3% | **0°C** |
| **CC-CV** | 2.9859 | 2.9132 | 97.6% | **20°C** |
| **CT-CV** | 2.9169 | 2.8407 | 97.4% | **20°C** |
| **CC-CV** | 3.0062 | 2.9507 | 98.2% | **50°C** |
| **CT-CV** | 3.0340 | 2.9517 | 97.3% | **50°C** |

### 3.3.1 Summary of Coulombic Efficiency

The CE tests performed has shown variable performance, where CT-CV technique did not present considerable improvement over CC-CV, and in some cases it presented worse results when compared to CC-CV method. Due to the narrow improvement range it can be considered that CT-CV and CC-CV techniques have similar CE performance.

## 3.4 Aging

The cycle life results for BUT1 (LG18650HG2) at room temperature is presented in Figure 3.33. The CT-CV and CC-CV capacity degradation over several cycles are shown, where similar decay for both methodologies can be observed. In addition, each charge methodology was tested for 1080 hour, and it resulted in 228 cycles for

CC-CV and 308 cycles for CT-CV, an improvement of approximately 25% in charging time for CT-CV method.

Since the test was running in an open area with no ambient temperature control, the CT-CV cycle life results for charging time and capacity are expected to vary since the PID controller adjusts the current based on the measured $T_s$. So if the ambient temperature is the same or close to the fixed reference, the charging current will be zero or minimum.

Moreover, the curve fitting tool from Matlab workbench was used to access the best fitting equation to model the capacity fade with cycle life. A good fitting was observed for both exponential and power functions and their equations as function of the cycle number are given from Equation 3.1, Equation 3.2, Equation 3.3, and Equation 3.4.

$$CTCV_{EXP}(n) = 0.2317e^{(-5.3X10-3n)} + 2.449e^{(-3.5X10^{-5}n)} \tag{3.1}$$

$$CCCV_{EXP}(n) = 0.1214e^{(-2.3X10-2n)} + 2.637e^{(-1.6X10^{-4}n)} \tag{3.2}$$

$$CTCV_{power}(n) = 2.793^{-0.017n} \tag{3.3}$$

$$CCCV_{power}(n) = 2.849^{-0.019n} \tag{3.4}$$

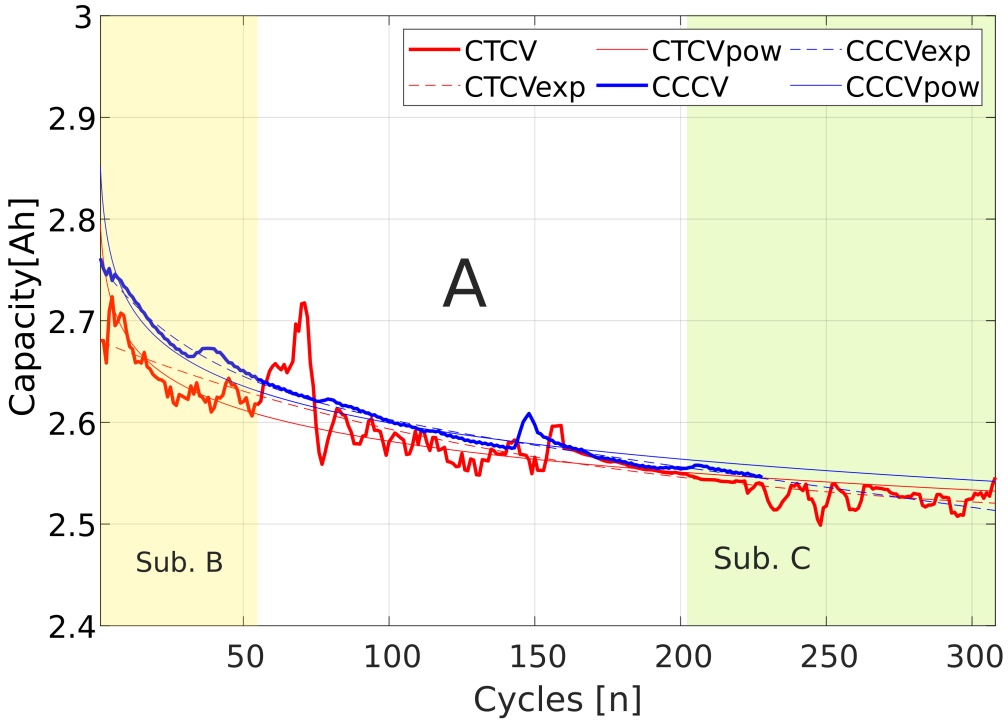


Figure 3.33: Experimental BUT1 (LG18650HG2) capacity fade for CC-CV and CT-CV charging methods. Exponential and power functions curves.

Figure 3.34 shows the subsection B of Figure 3.33. It is observed less than 0.05 Ah of capacity difference at the beginning of the cycle life test. Also, from the curve fitting, we can relate the power function to give a better result at the beginning of the charge, since it predicts a higher capacity in cycle number 1, closer to the nominal 3 Ah capacity from the datasheet.

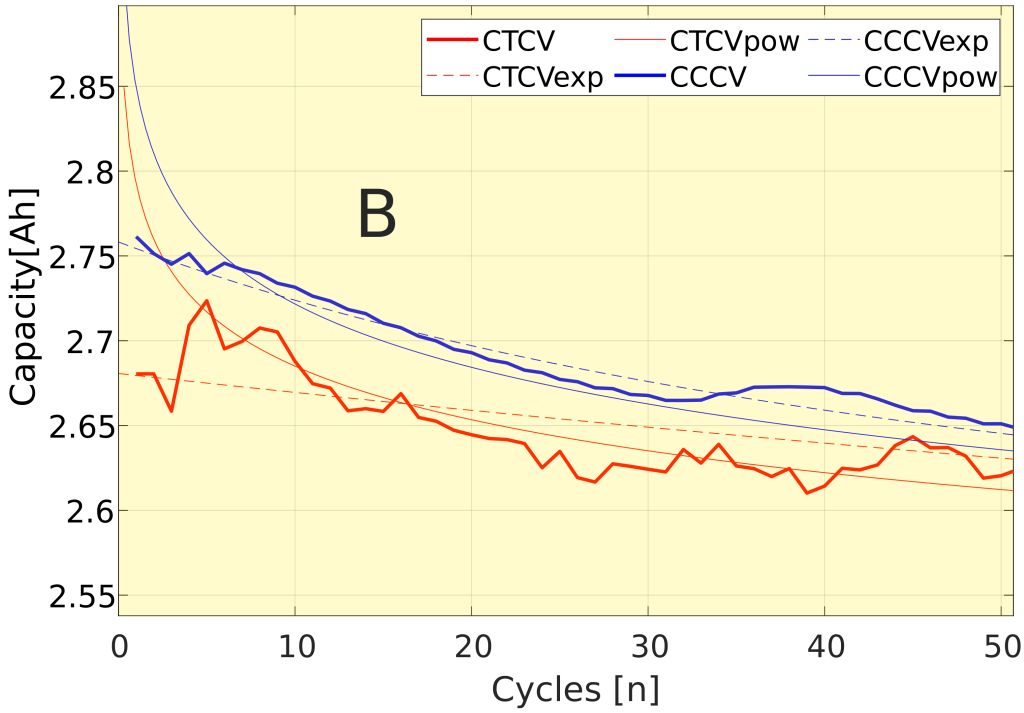


Figure 3.34: Experimental BUT1 (LG18650HG2) capacity fade for CC-CV and CT-CV charging methods first tested cycles. Exponential and power functions curves.

Figure 3.35 presents the subsection C of Figure 3.33. It can be observed that an oscillation of capacity on the CT-CV methodology of 0.04 Ah, while CC-CV kept the capacity fade at a constant fade, with minimum oscillation. The reason for the oscillation is the adaptive charging current for produced by the PID controller. In addition, the exponential curve fitting predicts the capacity fade of CC-CV being higher than CT-CV after cycle 277. Meanwhile, the power function predicts a similar capacity fade for both charging methodologies.

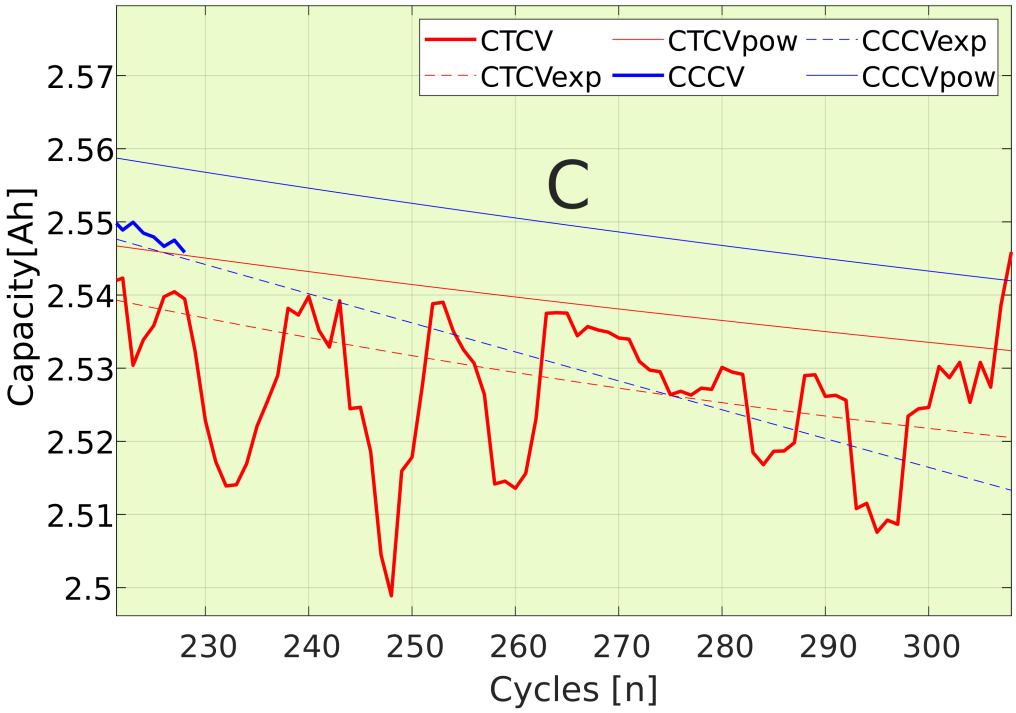


Figure 3.35: Experimental BUT1 (LG18650HG2) capacity fade for CC-CV and CT-CV charging methods last tested cycles. Exponential and power functions curves.

The evolution assessment of the average ambient temperature per cycle, maximum surface temperature per cycle, surface temperature rise, and time to charge to CV phase is presented for CC-CV in Figure 3.36, and for CT-CV Figure 3.37.

The CC-CV surface temperature evolution is constant shown in graph C of Figure 3.36. However, the ambient temperature is being influenced by the heat generated, so the gradient between charging methodologies is having low variation along with the cycle life. Meanwhile, the decay of charging time for the CV phase can be related to the capacity fade. With the internal resistances growth, the same current results in a higher voltage drop, resulting in a higher battery voltage.

Meanwhile, the behavior of CT-CV methodology over the evolution of surface temperature is controlled, as it can be observed in graph B of Figure 3.37. For the

first 75 cycles, the reference was set by the CC-CV maximum temperature, which was 29°C. Moreover, the ambient temperature increased considerably, and a reference adjustment to 31°C was needed; to increase the charging current for the PID controller. Also, the effects of the ambient temperature variation can be observed in the charge time to CV phase in graph D as well, where the PID had minimum or zero current, as it can be observed between cycles 50 to 75. Also, the ambient temperature decreased from cycles 160 to 220. However, the PID reference was not adjusted and remained 31°C. Thus, the surface temperature rise was approximately 6°C, and the charge time reduced considerably.

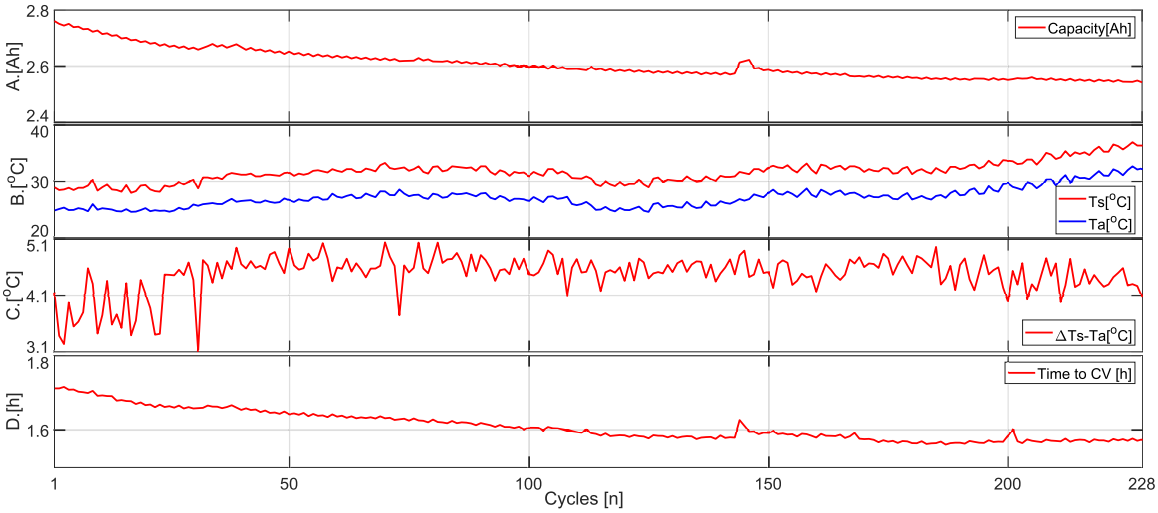


Figure 3.36: CC-CV life cycle assessment for A. Capacity fade, B. Surface and ambient temperature, C. Surface temperature rise, and D. Charge time to reach CV phase.

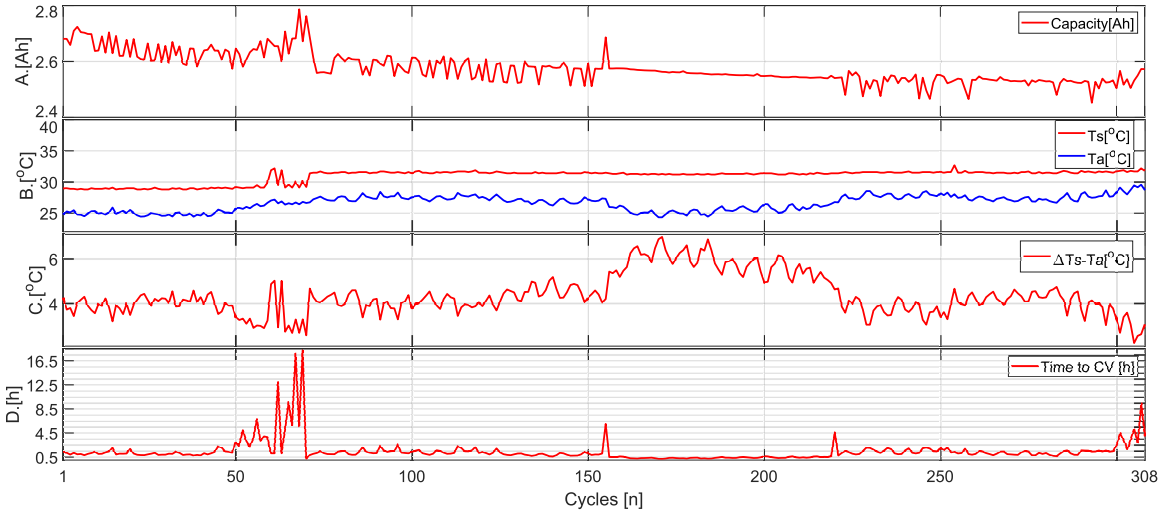


Figure 3.37: CT-CV life cycle assessment for A. Capacity fade, B. Surface and ambient temperature, C. Surface temperature rise, and D. Charge time to reach CV phase.

### 3.4.1 Summary of Aging

It can be observed from the life cycle assessment that both CC-CV and CT-CV produced similar capacity fade for the number of cycles tested. Furthermore, the CT-CV will result in less capacity fade after cycle 227, when predicting the capacity fade with a power function. Also, from the evolution per cycle study, the importance of the ambient temperature control for the CT-CV methodology can be observed.

## 3.5 Thermal-electrical Model Results

The thermal-electrical model results are presented in this section only for BUT1 due to extensive testing time. Also, its parameters are acquired as described in Chapter 2.3. The ECM is modeled for $T_a$: 0°C, 20°C and 50°C, and for current: 150 mA, 1.5 A and 4 A. The thermal model is coupled to ECM, and the second-order thermal model parameters are estimated with the CT-CV results. In the end, the CT-CV charging input current is used as input for the model, and the voltage and surface

temperature is compared to the experimental results.

The SoC is calculated with the nominal capacity of the battery, which for BUT1 is 3 Ah. The capacity changes accordingly with the scenario the battery is running on. Where the ambient temperature and different charge currents change the measured capacity, it is necessary to normalize the model's capacity at nominal value from the manufacturer datasheet. So, with normalized capacity, the parameters can use SoC as input directly for all tests.

### 3.5.1 Electrical Circuit Model Results

Figure 3.38 shows the ECM model implemented in MATLAB 2019b. Simulink and Simscape tools were used to create the parameters models: $V_{ocv}$, $R_{series}$, first transient network ($R_{trans1}$, $C_{trans1}$), and the second transient network ($R_{trans2}$, $C_{trans2}$). The parameters were created in Simscape, where they were hard coded with LUT functions.

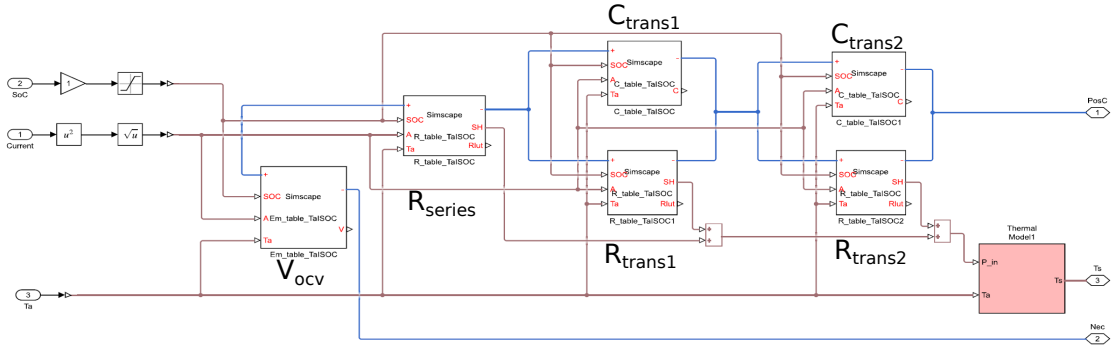


Figure 3.38: Complete Simulink/Simscape thermal-electrical model.

The first element of the ECM is the voltage source $V_{ocv}$, which is function of SoC and $T_a$. The maximum voltage is achieved at 100% SoC, and it is constant for all charging currents. It is observed that a small voltage variation with to $T_a$ change a lower SoC. However, as expected there is a large voltage variation is along the range

of SoC, with larger variation on 100% to 90% and 20% to 0% SoC. Figure 3.39 shows the output voltages of $V_{ocv}$ parameter values, with interpolated results.

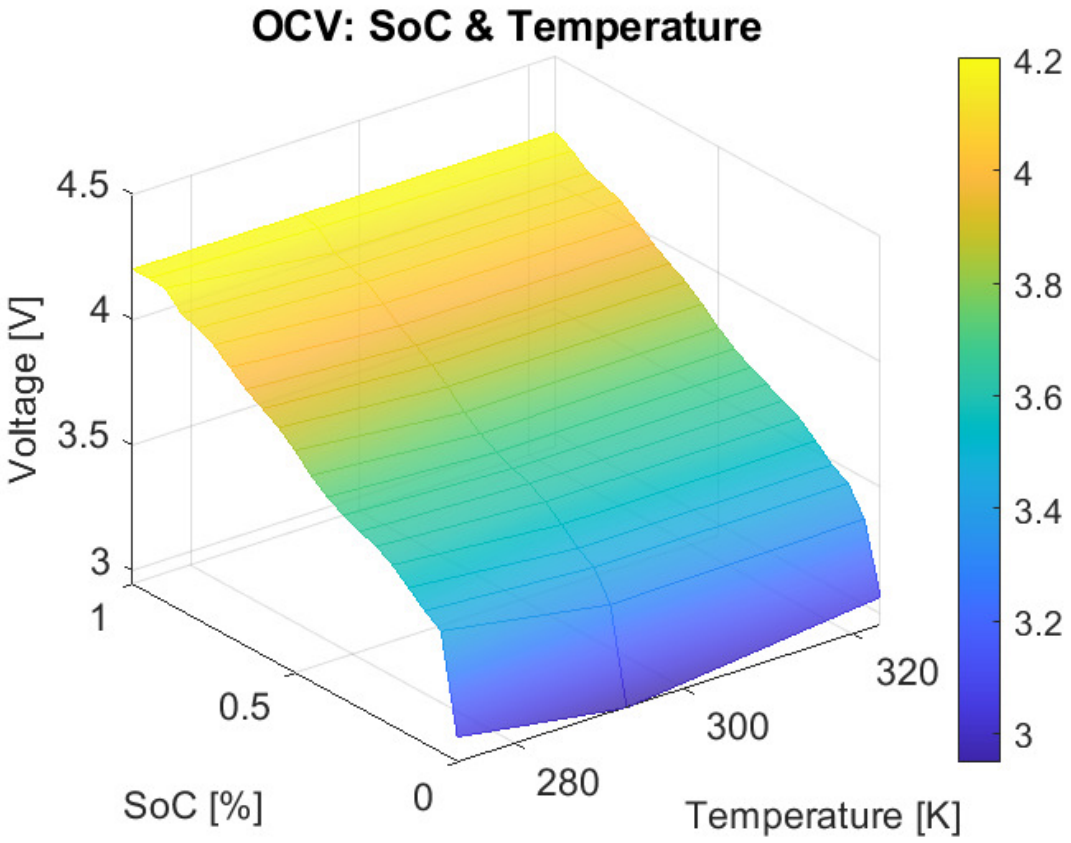


Figure 3.39: LG18650HG2 OCV-SoC.

The results for $R_{series}$, $R_{trans1}$, $C_{trans1}$, $R_{trans2}$, $C_{trans2}$ are presented in a graph format, where each parameter needs 6 graphs to show the entire range of operation, due to the 3 inputs necessary for the function. So, the left column shows the parameter results for SoC and $I_{bat}$ under different $T_a$, and the right column shows the parameter results for SoC and $T_a$ under different $I_{bat}$.

Figure 3.40 presents the results for $R_{series}$ with the variation of SoC, $I_{bat}$ and $T_a$. The SoC variation has a large impact on $R_{series}$ values, where higher resistance values are found near 100% and 0% SoC. Despite the fact that current and temperature have

a small impact on $R_{series}$ values, when compared to SoC, they still change the $R_{series}$ with high level of non-linearity.

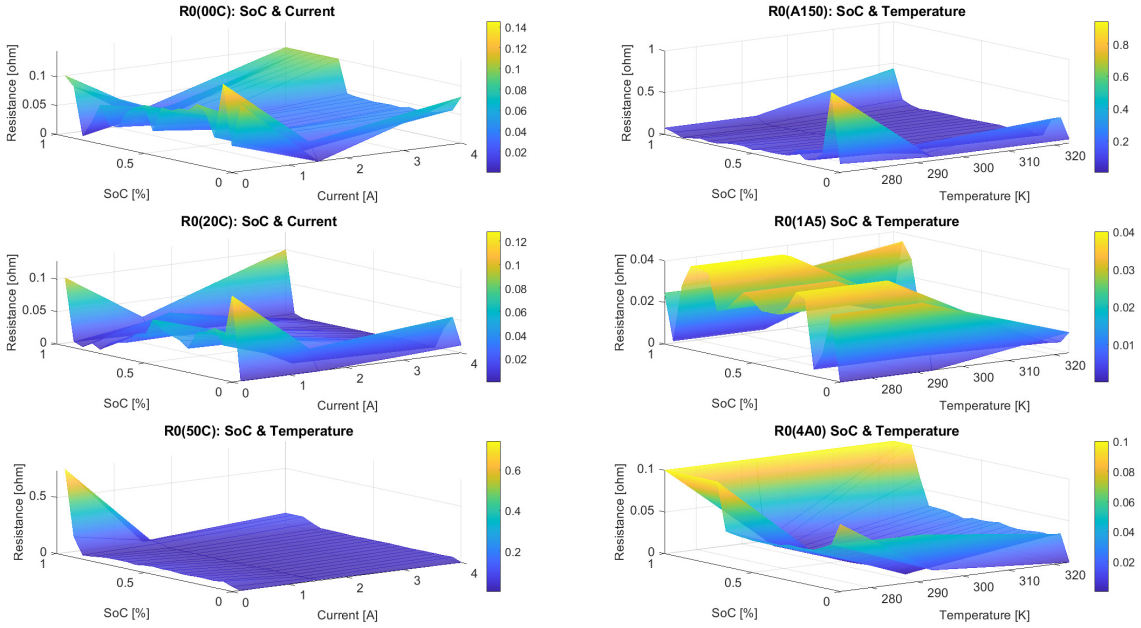


Figure 3.40: LG18650HG2: $R_{series}$ parameter results with variation of temperature and current.

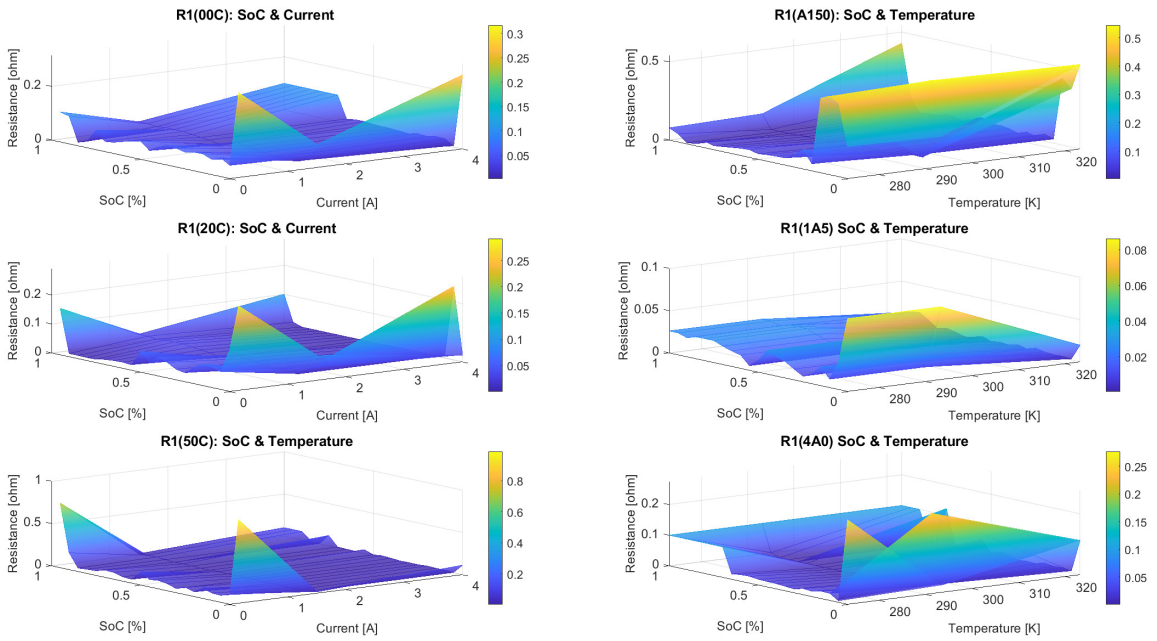


Figure 3.41: LG18650HG2 R1 parameter results with variation of temperature and current.

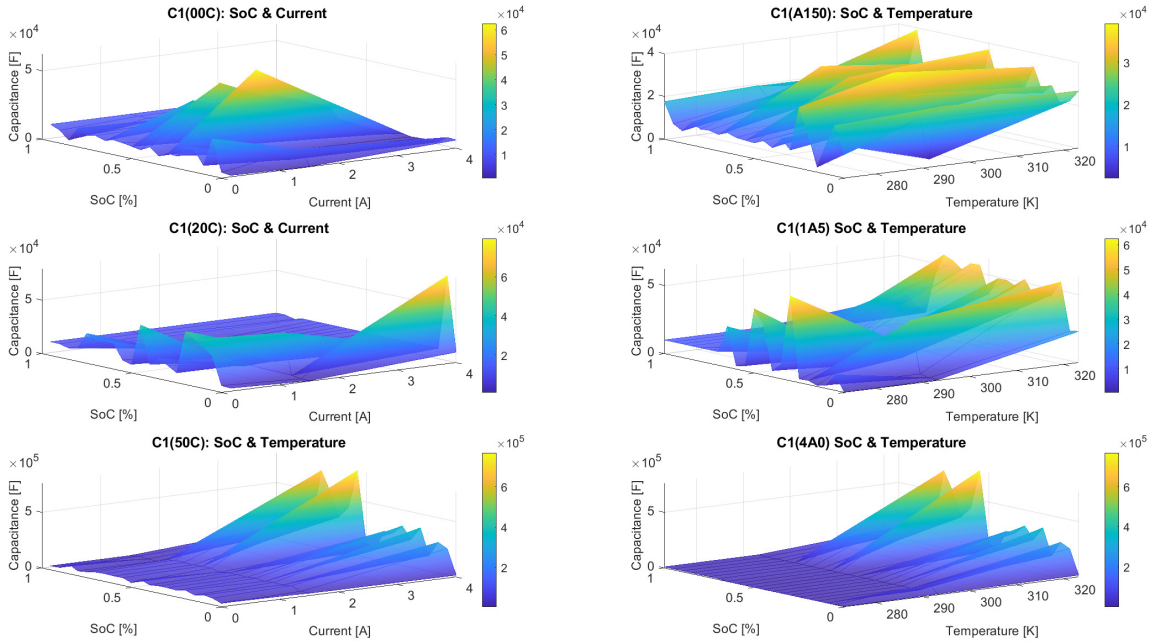


Figure 3.42: LG18650HG2 C1 parameter results with variation of temperature and current.

The first transient network has variable response with SoC, $I_{bat}$, and $T_a$. The

RC time constant changes over the entire range of SoC, where $R_{trans1}$ has higher values in both ends of SoC, meanwhile, $C_{trans1}$ variation is spread all over the SoC range. Furthermore, in most cases, the RC time constant changes with the increase of current due to an increase of both $R_{trans1}$ and $C_{trans1}$. Also, the increase in ambient temperature increases the values of $R_{trans1}$ and $C_{trans1}$, leading to an increase of RC time constant. It is observed that the first transient network increases its RC time constant in both ends of SoC range, with increase of $I_{bat}$, and $\mathrm{T}_a$.

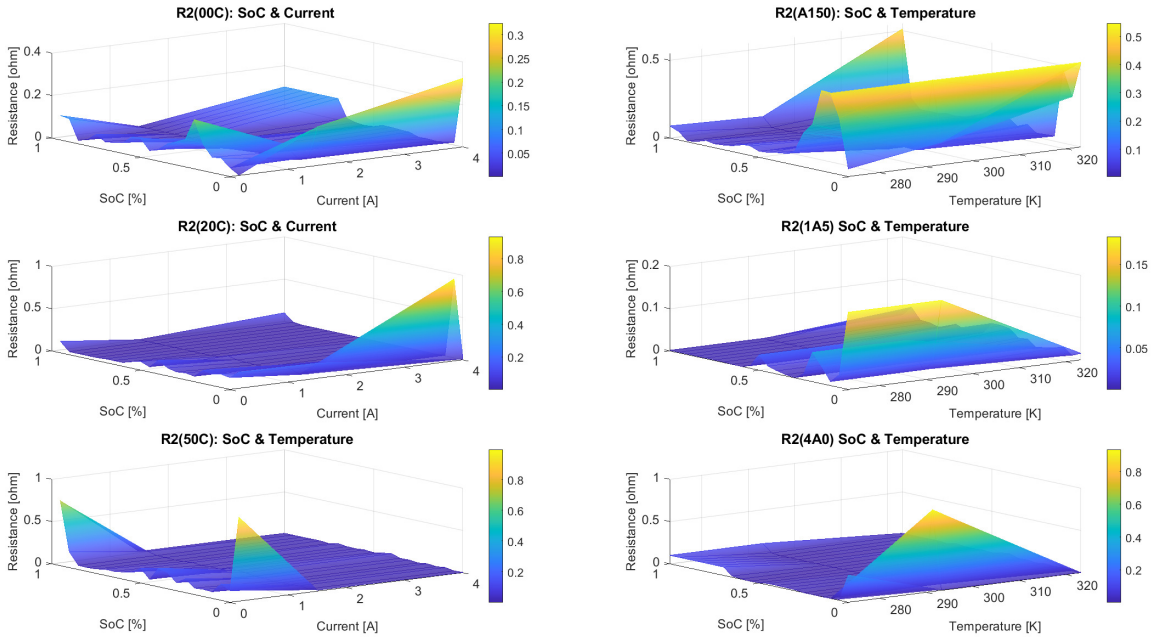


Figure 3.43: LG18650HG2 R2 parameter results with variation of temperature and current.

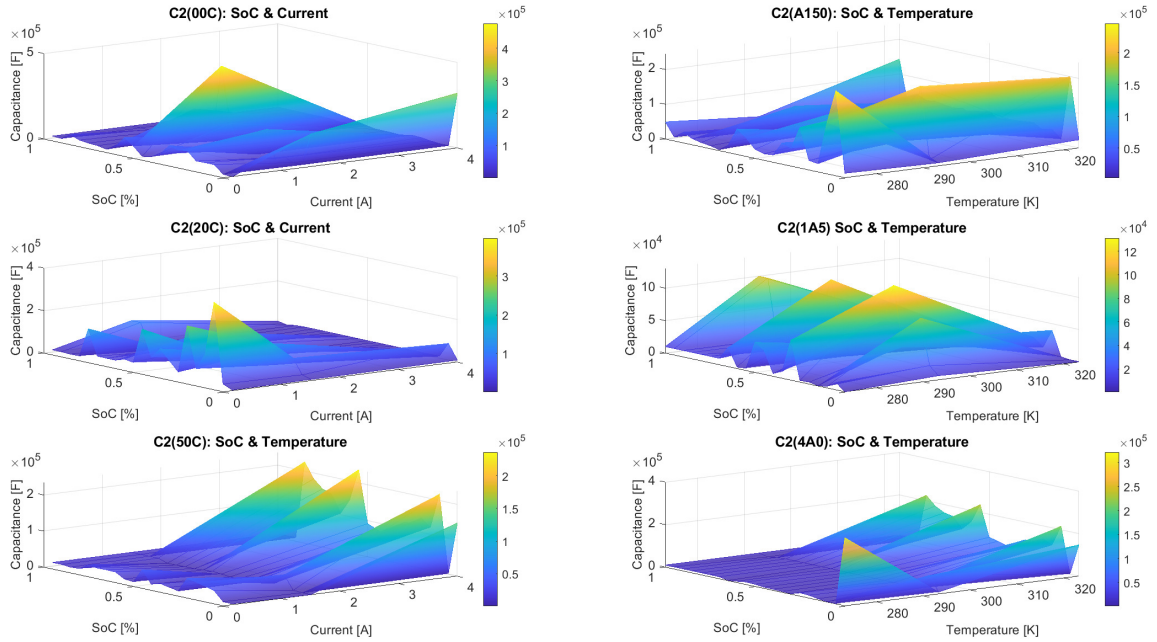


Figure 3.44: LG18650HG2 C2 parameter results with variation of temperature and current.

The second transient network changes with SoC, $I_{bat}$, and $T_a$. In addition, similarly to the first transient network, the RC time constant changes in both ends of SoC, due to increase of $R_{trans2}$. The RC time constant grows with the increase of $I_{bat}$ as both $R_{trans2}$ and $C_{trans2}$ increases. However, at 20°C the RC time constant diminishes with the increase of $I_{bat}$, due to decrease of $C_{trans2}$. Furthermore, the RC time constant increases with the rise of $T_a$, due to increase of both $R_{trans2}$ and $C_{trans2}$, although, at $I_{bat}$ of 1.5 A the RC time constant is maximum on 20°C. So, generally the second transient network increases with the rise of $I_{bat}$, and $T_a$, unless it is at specific points of 20°C and 1.5 A, respectively.

So, with the parameters results presented for $V_{ocv}$, $R_{series}$, first transient network, and second transient network, for $T_a$: 0°C, 20°C and 50°C, and for current: 150 mA, 1.5 A and 4 A, it is possible to have a model capable of operating at any $T_a$ and charging current. The LUT uses interpolation to predict the values between these

ranges, and it uses extrapolation methods to predict the values outside the mentioned ranges.

The ECM parameters in this chapter are embedded in a Simulink and Simscape project. The resistances have an output for the power loss, which is used in the second-order thermal model to simulate the coupled thermal-electrical model's thermal behavior.

### 3.5.2 Thermal Model Parameters

The second-order thermal model uses the ECM parameter results presented in Chapter 3.5.1. Also, fixed physical parameters intrinsic of the battery and its material formation are presented in Table 3.14, and they can be found in the datasheet. The heat produced at the very inner point of the cylindrical battery is transferred through the thickness, represented by its radius. The parameter estimation tool uses $T_s$ as input. The $T_s$ at 20°C acquired on CT-CV is used for harvesting the parameters for the thermal model.

Table 3.14: Fixed dimensions and physical specification used in the thermal model.

| | |
|---|---|
| **Cell diameter** | 1.8 cm |
| **Cell length** | 65 cm |
| **Case thickness** | 0.3 mm |
| **Jelly thickness** | 0.9 cm |
| **Cell mass** | 49 g |

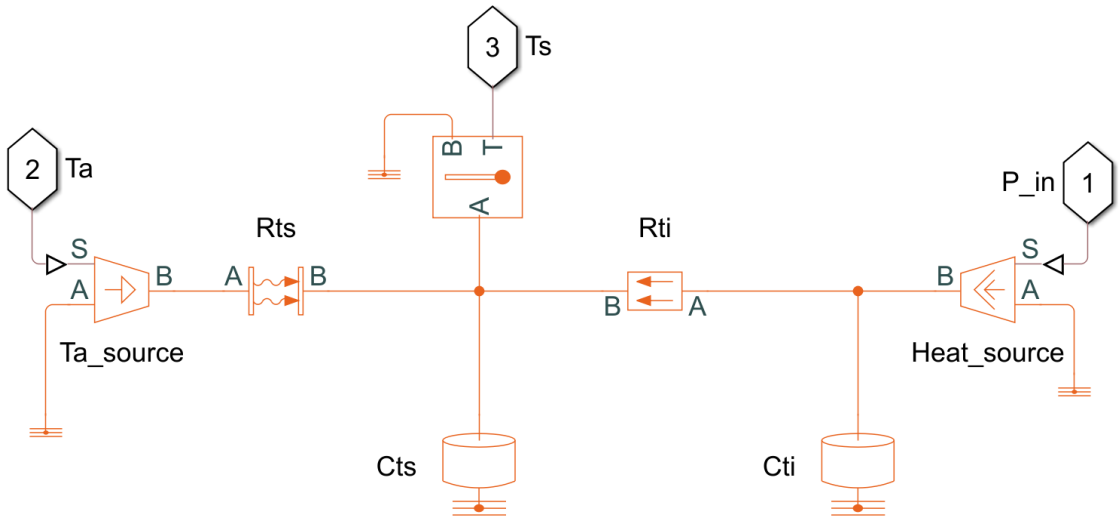


Figure 3.45: Simulink/Simscape thermal model.

Figure 3.45 shows the Simscape thermal model implemented for the battery BUT1 (LG18650HG2). The heat source is the result of power loss from ECM. The heat flows from the jelly to the case in a conduction manner, where it is stored in the heat capacity element ($C_{ti}$), and transferred to the case via thermal resistance ($R_{ti}$). The jelly parameters $C_{ti}$, and $R_{ti}$ are estimated using the same method used for ECM parameter estimation, and they are shown in Table 3.15. The heat transfer continues to flow from the jelly to the ambient through the case in a convection manner. The estimated thermal capacity ($C_{ts}$), and thermal resistance ($R_{ts}$) parameters are shown in Table 3.16.

Table 3.15: Jelly parameters.

| | |
|---|---|
| **thermal Conductivity ($R_{ti}$)** | 2.4 W/(m2K) |
| **Thickness ($R_{ti}$)** | 9 mm |
| **Area ($R_{ti}$)** | 368 cm2 |
| **Specific heat ($C_{ti}$)** | 1054 (J/kg/K) |
| **Mass ($C_{ti}$)** | 42.3 g |

Table 3.16: Case parameters.

| | |
|---|---|
| **Heat transfer coefficient** | 2.62 $W/(m^2K)$ |
| **Thickness** | 0.3 mm |
| **Area** | 368 cm2 |
| **Specific heat** | 1386 (J/kg/K) |
| **Mass** | 6.7 g |

The thermal parameter estimation results are very close to the results obtained in [47], [49], and [57]. They are very dependent on cell chemistry and layer stack materials. So, with the ECM parameters, and thermal model parameters estimated, it is possible to perform the charging simulation with CT-CV current input.

### 3.5.3 Coupled Thermoelectrical Model Results

The final model predicts the battery voltage and the surface temperature of BUT1 at different ambient temperatures and charging currents. The model is formed with two models, the first model is the ECM composed by the parameters presented in Chapter 3.5.1, and the second model is the thermal model composed by the parameters presented in Chapter 3.5.2.

Furthermore, these two models are coupled, where the ECM outputs the heat generated by its internal resistance, and it is used as input for the thermal model. Figure 3.38, and Figure 3.45 represent both models implemented in Simscape. Also, the coupled model uses CT-CV charging current, SoC, and $T_a$ as input.

Figure 3.46 show experimental and simulation results for CT-CV charging methodology with $T_a$ of 0°C. The battery voltage is presented on the left side, and a small error is observed throughout the entire test. Moreover, it is observed the model predicting the voltage spike due to the high current at the beginning of charging. Also, the CV phase has the current decreasing exponentially, which brings complexity for the model prediction, although it is observed good predictions during this phase. The battery voltage errors are calculated with RMSE of 26.6 mV, MAE of 17.6 mV, and correlation $R^2$ of 0.99.

The $T_s$ experimental and simulated results for 0°C are presented in the right side of Figure 3.46. The coupled model can predict the $T_s$ with some restrictions, like the observed errors during steady state, due to variable heat generation produced by ECM. Meanwhile, the transient response results are reasonable, with small errors for maximum temperature predictions. The $T_s$ errors are calculated with RMSE of 0.34°C, MAE of 0.24°C, and correlation $R^2$ of 0.85.

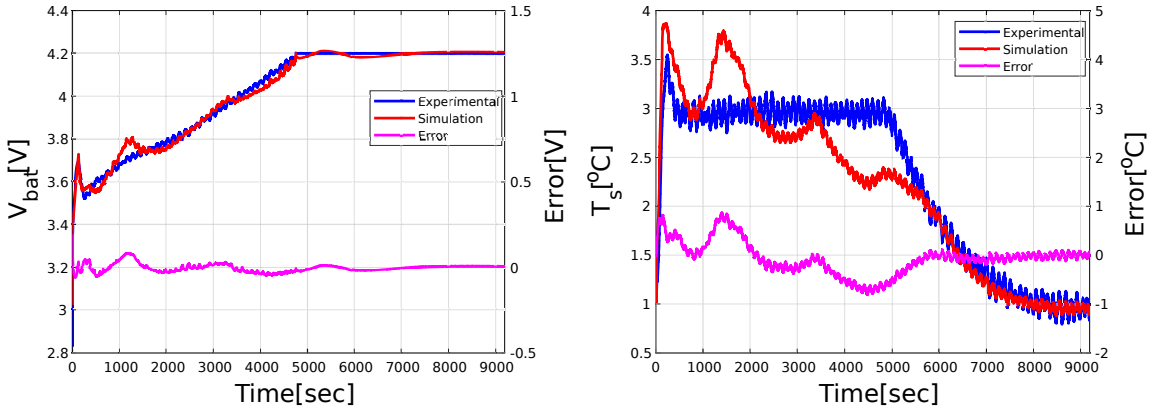


Figure 3.46: 0°C: Experimental and simulation results for battery voltage on the left, and $T_s$ on the right.

Figure 3.47 shows the experimental and simulation results for CT-CV charging methodology with $T_a$ of 20°C. The battery voltage results are presented in the left graph. With the battery voltage simulation, excellent results can be observed following the experimental results very close during the entire test. Moreover, even during the beginning of the CT phase, the model can predict the battery voltage. Also, during the CV phase, the error is maintained close to zero. The battery voltage errors are calculated with RMSE of 26.1 mV, MAE of 13.2 mV, and correlation $R^2$ of 0.99.

The coupled model was able to have excellent prediction of $T_s$ for $T_a$ of 20°C, as it can be observed in Figure 3.47 on the right graph. The $T_s$ rise and fall responses followed very close to the experimental results, while the maximum temperature has small errors. The steady-state error was better than 20°C responses, although peaks are being produced by the resistances' variation with SoC. The $T_s$ errors are calculated with RMSE of 0.27°C, MAE of 0.18°C, and correlation $R^2$ of 0.90.

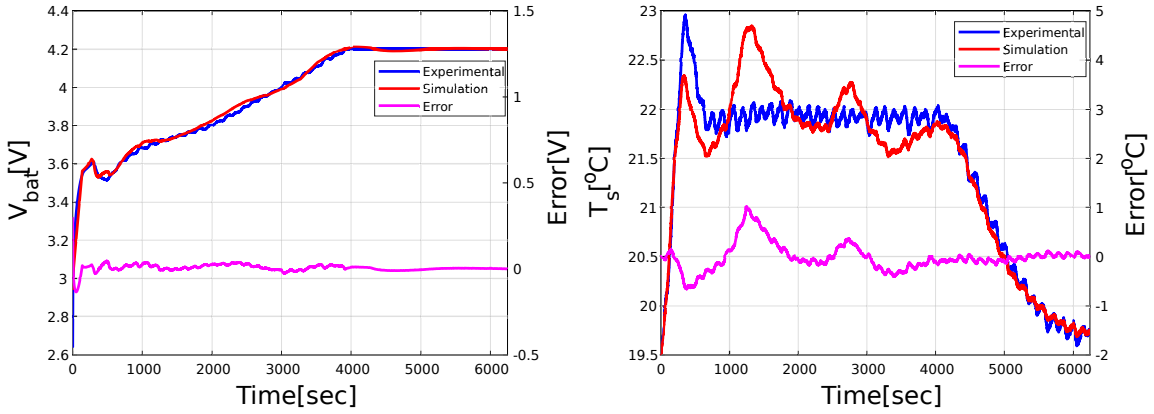


Figure 3.47: 20°C: Experimental and simulation results for battery voltage on the left, and $T_s$ on the right.

Figure 3.48 shows the experimental and simulation results for CT-CV charging methodology with $T_a$ of 50°C in the left graph. The model is capable of predicting the battery voltage for the entire SoC range, although at CV phase the errors are higher, the predictions are excellent. The battery voltage errors are calculated with RMSE of 29.1 mV, MAE of 16.9 mV, and correlation $R^2$ of 0.99.

The coupled model presented excellent simulation results for $T_s$ at 50°C, as it can be seen in Figure 3.48 in the right graph. The $T_s$ rise follow the experimental results closely, with good prediction of maximum temperature. The steady state response has small errors along SoC range. The $T_s$ errors are calculated with RMSE of 0.24°C, MAE of 0.21°C, and correlation $R^2$ of 0.83.

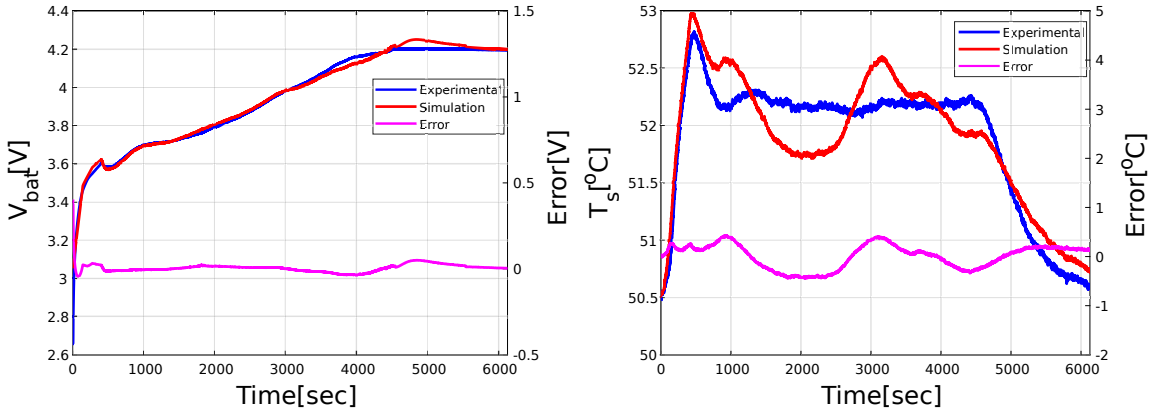


Figure 3.48: 50°C: Experimental and simulation results for battery voltage on the left, and $T_s$ on the right.

Table 3.17 summarizes the error analysis for battery voltage response for BUT1 at different temperatures tested. The RMSE, MAE, and $R^2$ presented excellent results for the battery voltage, with errors not exceeding 30 mV compared to experimental results.

Table 3.17: Battery Voltage error analysis between experimental and simulation.

| **RMSE(0°C)** | **RMSE(20°C)** | **RMSE(50°C)** |
|---|---|---|
| 0.0266 | 0.0261 | 0.0291 |
| **MAE(0°C)** | **MAE(20°C)** | **MAE(50°C)** |
| 0.0176 | 0.0132 | 0.0169 |
| **$R^2$(0°C)** | **$R^2$(20°C)** | **$R^2$(50°C)** |
| 0.9886 | 0.9934 | 0.9903 |

Table 3.18 summarizes the error analysis for $T_s$ response for BUT1 at different temperatures tested. It can be observed that the correlation $R^2$ has satisfactory results due to the big variance on the model output. The internal resistances change with SoC produces a variable heat generation, which results in the variance observed. The results are excellent, where maximum surface temperature and temperature rise,

and fall can be predicted for the three study cases. Furthermore, the temperature error never exceeded 1°C, and the error analysis shows less than 0.4°C error for both RMSE and MAE.

Table 3.18: Surface temperature estimation error analysis between experimental and simulation.

| **RMSE(0°C)** | **RMSE(20°C)** | **RMSE(50°C)** |
|---|---|---|
| 0.3383 | 0.2751 | 0.2428 |
| **MAE(0°C)** | **MAE(20°C)** | **MAE(50°C)** |
| 0.2433 | 0.1849 | 0.2113 |
| **$R^2$(0°C)** | **$R^2$(20°C)** | **$R^2$(50°C)** |
| 0.8547 | 0.9004 | 0.8273 |

## 3.6 Conclusion

The CT-CV charging was first implemented by tuning the controller, and it was followed by charge and discharge tests for 0°C, 20°C, and 50°C. Moreover, the CC-CV method was implemented and tested at the same temperatures. Both methodologies were compared for three different BUTs and temperatures. Finally, the superiority of CT-CV charging methodology over CC-CV was observed, as it charged fast in all tests while maintaining the same $T_s$ rise as CC-CV tests. Also, the coulombic efficiency results did not present any significant difference between the two methods, and they can be considered to have the same efficiency.

The coupled thermal-electrical model could predict the battery voltage response during the CT-CV charging with excellent results for various $T_a$. The parameter estimation for various currents and $T_a$ was essential for the model to predict the battery voltage for the tests performed with CT-CV method. Furthermore, the $T_s$

results were satisfactory, with mostly transient responses having good results, and with maximum temperature being estimated with small errors. Although the steady-state response did not present excellent results, it is considered satisfactory due to errors not being more significant than 1°C at any point.

# Chapter 4

# Conclusions

## 4.1 Conclusion

The CT-CV charging methodology has been assessed in this thesis with analytical, simulation, and experimental investigation. The results show that the CT-CV charge time improved from 3%-27% over 0-100% SoC range, and up to 50% over 0-60% SoC range. Also, the higher ambient temperature produced excellent results for CT-CV charging time. The CE results are similar for both charge methods, which indicated the losses on CT-CV were comparable to CC-CV.

The CT-CV charge method has presented excellent results for the aging tests, where up to cycle 280, the CT-CV showed a similar capacity fade as the CC-CV. The aging estimation analysis shows an expected capacity fade improvement after cycle 280 over the conventional method. Moreover, the battery life cycle assessment proved that the CT-CV charge method can maintain the surface temperature constant throughout the cycles.

The thermal-electrical model has presented positive results for the battery voltage estimation, where a maximum error of 30 mV was observed. Lastly, the surface

temperature also presented good results, with a maximum error of 1°C.

In conclusion, the results show that it is possible to achieve a fast-charging time under different ambient temperatures with different Li-ion batteries while maintaining a similar surface temperature rise to the conventional CC-CV charging method.

## 4.2 Contributions

- A thorough study of the EV and their elements was conducted in the first chapter. Understanding its characteristics, constructions, and topology is critical for the improvement of the EV in general.

- A review was conducted on the battery construction, battery aging mechanism, and charging methodologies.

- The BAS capable of logging and controlling equipment with a refreshing time of 200 ms and capable of running with reliability for more than 1080 hours non-stop was presented and detailed in Chapter 2.

- A simpler CT-CV charging algorithm was developed when compared to [36], where the feed-forward term on the controller was swapped by fine-tuning the PID controller gains.

- A comparative study was done of CT-CV and CC-CV with respect to charge time, coulombic efficiency, and aging tests. Furthermore, the comparative results were presented for the manufacturer LG Chem and part numbers: INR18650-HG2, INR18650HE4, and manufacturer Samsung SDI INR18650-30Q. The charging time and columbic efficiency results were presented for an ambient temperature of 0°C, 20°C, and 50°C.

- A charging methodology with charge time improvement ranging from 3% at lower temperatures and 50% at higher temperatures was presented, with similar capacity fade to the conventional CC-CV method.

## 4.3 Future Works

- The design on an adaptive CT-CV temperature control, where it adjusts the temperature according to the ambient temperature.

- The study of the aging of both CC-CV and CT-CV using the impedance evolution over cycles. In addition, the complete life cycle assessment, from cycle number 1 to EoL, would be significant for comparing the efficacy of CT-CV over CC-CV.

- The validation of the CT-CV charge methodology in a battery pack, using fewer temperature sensors for the pack, instead of using one temperature sensor for each cell.

- The literature review and design of an advanced battery model that can predict the inner temperature, surface temperature, the battery voltage for the charge/discharge, and rest periods.

# Bibliography

[1] S.-T. Myung, Y. Hitoshi, and Y.-K. Sun, "Electrochemical behavior and passivation of current collectors in lithium-ion batteries," *Journal of Materials Chemistry*, vol. 21, no. 27, pp. 9891–9911, 2011.

[2] T. R. Jow, S. A. Delp, J. L. Allen, J.-P. Jones, and M. C. Smart, "Factors limiting li+ charge transfer kinetics in li-ion batteries," *Journal of The Electrochemical Society*, vol. 165, no. 2, p. A361, 2018.

[3] B. C. Group *et al.*, "Batteries for electric cars. challenges, opportunities, and the outlook to 2020," *BCG Report*, 2010.

[4] C. R. Birkl, M. R. Roberts, E. McTurk, P. G. Bruce, and D. A. Howey, "Degradation diagnostics for lithium ion cells," *Journal of Power Sources*, vol. 341, pp. 373–386, 2017.

[5] S. Panchal, M. Mathew, R. Fraser, and M. Fowler, "Electrochemical thermal modeling and experimental measurements of 18650 cylindrical lithium-ion battery during discharge cycle for an ev," *Applied Thermal Engineering*, vol. 135, pp. 123–132, 2018.

[6] X. Lin, H. E. Perez, J. B. Siegel, A. G. Stefanopoulou, Y. Li, R. D. Anderson, Y. Ding, and M. P. Castanier, "Online parameterization of lumped thermal dy-

namics in cylindrical lithium ion batteries for core temperature estimation and health monitoring," *IEEE Transactions on Control Systems Technology*, vol. 21, no. 5, pp. 1745–1755, 2012.

[7] E. Grunditz, *Design and assessment of battery electric vehicle powertrain, with respect to performance, energy consumption and electric motor thermal capability.* Chalmers University of Technology, 2016.

[8] C. D. Anderson and J. Anderson, *Electric and hybrid cars: A history.* McFarland, 2010.

[9] C. Rolim, P. Baptista, T. Farias, and Ó. Rodrigues, "Electric vehicle adopters' motivation, utilization patterns and environmental impacts: A lisbon case study," in *2013 World Electric Vehicle Symposium and Exhibition (EVS27)*, pp. 1–11, IEEE, 2013.

[10] "U.s. energy facts explained." `https://www.eia.gov/energyexplained/us-energy-facts/`. Accessed: 2020-07-10.

[11] "Modern societies are dependent on reliable and secure supplies of electricity. electricity generation accounts for a third of all primary energy use in ireland.." `https://www.seai.ie/data-and-insights/seai-statistics/key-statistics/electricity/`. Accessed: 2020-07-09.

[12] "Australian electricity generation - fuel mix." `https://www.energy.gov.au/australian-electricity-generation-fuel-mix`. Accessed: 2020-07-12.

[13] T. Gustafsson and A. Johansson, "Comparison between battery electric vehicles and internal combustion engine vehicles fueled by electrofuels," *Chalmers Tekniska HöGskola: Göteborg, Sweden*, 2015.

[14] G. Saldaña, J. I. San Martin, I. Zamora, F. J. Asensio, and O. Oñederra, "Electric vehicle into the grid: Charging methodologies aimed at providing ancillary services considering battery degradation," *Energies*, vol. 12, no. 12, p. 2443, 2019.

[15] A. Poullikkas, "Sustainable options for electric vehicle technologies," *Renewable and Sustainable Energy Reviews*, vol. 41, pp. 1277–1287, 2015.

[16] K. Jonasson, *Analysing hybrid drive system topologies*. Citeseer, 2002.

[17] M. Gruenig, M. Witte, D. Marcellino, J. Selig, and H. van Essen, "An overview of electric vehicles on the market and in development," *CE Delft, Delft, Tech. Rep., April*, 2011.

[18] F. Un-Noor, S. Padmanaban, L. Mihet-Popa, M. N. Mollah, and E. Hossain, "A comprehensive study of key electric vehicle (ev) components, technologies, challenges, impacts, and future direction of development," *Energies*, vol. 10, no. 8, p. 1217, 2017.

[19] F. Baronti, R. Di Rienzo, N. Papazafiropulos, R. Roncella, and R. Saletti, "Investigation of series-parallel connections of multi-module batteries for electrified vehicles," in *2014 IEEE International Electric Vehicle Conference (IEVC)*, pp. 1–7, IEEE, 2014.

[20] M. Lelie, T. Braun, M. Knips, H. Nordmann, F. Ringbeck, H. Zappen, and D. U. Sauer, "Battery management system hardware concepts: an overview," *Applied Sciences*, vol. 8, no. 4, p. 534, 2018.

[21] K. Jalkanen, J. Karppinen, L. Skogström, T. Laurila, M. Nisula, and K. Vuorilehto, "Cycle aging of commercial nmc/graphite pouch cells at different temperatures," *Applied Energy*, vol. 154, pp. 160–172, 2015.

[22] X.-G. Yang and C.-Y. Wang, "Understanding the trilemma of fast charging, energy density and cycle life of lithium-ion batteries," *Journal of Power Sources*, vol. 402, pp. 489–498, 2018.

[23] X.-G. Yang, G. Zhang, S. Ge, and C.-Y. Wang, "Fast charging of lithium-ion batteries at all temperatures," *Proceedings of the National Academy of Sciences*, vol. 115, no. 28, pp. 7266–7271, 2018.

[24] M. Ecker, P. S. Sabet, and D. U. Sauer, "Influence of operational condition on lithium plating for commercial lithium-ion batteries–electrochemical experiments and post-mortem-analysis," *Applied energy*, vol. 206, pp. 934–946, 2017.

[25] Y.-J. Lee, H.-Y. Choi, C.-W. Ha, J.-H. Yu, M.-J. Hwang, C.-H. Doh, and J.-H. Choi, "Cycle life modeling and the capacity fading mechanisms in a graphite/lini 0.6 co 0.2 mn 0.2 o 2 cell," *Journal of Applied Electrochemistry*, vol. 45, no. 5, pp. 419–426, 2015.

[26] M. Ecker, N. Nieto, S. Käbitz, J. Schmalstieg, H. Blanke, A. Warnecke, and D. U. Sauer, "Calendar and cycle life study of li (nimnco) o2-based 18650 lithium-ion batteries," *Journal of Power Sources*, vol. 248, pp. 839–851, 2014.

[27] J. W. Choi and D. Aurbach, "Promise and reality of post-lithium-ion batteries with high energy densities," *Nature Reviews Materials*, vol. 1, no. 4, pp. 1–16, 2016.

[28] S. Piller, M. Perrin, and A. Jossen, "Methods for state-of-charge determination and their applications," *Journal of power sources*, vol. 96, no. 1, pp. 113–120, 2001.

[29] W. Shen, T. T. Vo, and A. Kapoor, "Charging algorithms of lithium-ion batteries: An overview," in *2012 7th IEEE conference on industrial electronics and applications (ICIEA)*, pp. 1567–1572, IEEE, 2012.

[30] P. Keil and A. Jossen, "Charging protocols for lithium-ion batteries and their impact on cycle life—an experimental study with different 18650 high-power cells," *Journal of Energy Storage*, vol. 6, pp. 125–141, 2016.

[31] J.-W. Huang, Y.-H. Liu, S.-C. Wang, and Z.-Z. Yang, "Fuzzy-control-based five-step li-ion battery charger," in *2009 International Conference on Power Electronics and Drive Systems (PEDS)*, pp. 1547–1551, IEEE, 2009.

[32] L.-R. Dung and J.-H. Yen, "Ilp-based algorithm for lithium-ion battery charging profile," in *2010 IEEE International Symposium on Industrial Electronics*, pp. 2286–2291, IEEE, 2010.

[33] R. Chandrasekaran, "Quantification of bottlenecks to fast charging of lithium-ion-insertion cells for electric vehicles," *Journal of Power Sources*, vol. 271, pp. 622–632, 2014.

[34] D. Anseán, M. González, J. Viera, V. García, C. Blanco, and M. Valledor, "Fast charging technique for high power lithium iron phosphate batteries: A cycle life analysis," *Journal of Power Sources*, vol. 239, pp. 9–15, 2013.

[35] G. Sikha, P. Ramadass, B. Haran, R. E. White, and B. N. Popov, "Comparison of the capacity fade of sony us 18650 cells charged with different protocols," *Journal of power sources*, vol. 122, no. 1, pp. 67–76, 2003.

[36] R. C. Cope and Y. Podrazhansky, "The art of battery charging," in *Fourteenth Annual Battery Conference on Applications and Advances. Proceedings of the Conference (Cat. No. 99TH8371)*, pp. 233–235, IEEE, 1999.

[37] M. Chen and G. A. Rincon-Mora, "Accurate electrical battery model capable of predicting runtime and iv performance," *IEEE transactions on energy conversion*, vol. 21, no. 2, pp. 504–511, 2006.

[38] L.-R. Chen, S.-L. Wu, D.-T. Shieh, and T.-R. Chen, "Sinusoidal-ripple-current charging strategy and optimal charging frequency study for li-ion batteries," *IEEE Transactions on Industrial Electronics*, vol. 60, no. 1, pp. 88–97, 2012.

[39] A. Bessman, R. Soares, S. Vadivelu, O. Wallmark, P. Svens, H. Ekström, and G. Lindbergh, "Challenging sinusoidal ripple-current charging of lithium-ion batteries," *IEEE Transactions on Industrial Electronics*, vol. 65, no. 6, pp. 4750–4757, 2017.

[40] L. Patnaik, A. Praneeth, and S. S. Williamson, "A closed-loop constant-temperature constant-voltage charging technique to reduce charge time of lithium-ion batteries," *IEEE Transactions on Industrial Electronics*, vol. 66, no. 2, pp. 1059–1067, 2018.

[41] Y. Miao, P. Hynan, A. von Jouanne, and A. Yokochi, "Current li-ion battery technologies in electric vehicles and opportunities for advancements," *Energies*, vol. 12, no. 6, p. 1074, 2019.

[42] I. Baccouche, A. Mlayah, S. Jemmali, B. Manai, and N. E. B. Amara, "Implementation of a coulomb counting algorithm for soc estimation of li-ion battery for multimedia applications," in *2015 IEEE 12th International Multi-Conference on Systems, Signals & Devices (SSD15)*, pp. 1–6, IEEE, 2015.

[43] L. Saw, Y. Ye, and A. Tay, "Electrochemical–thermal analysis of 18650 lithium iron phosphate cell," *Energy Conversion and Management*, vol. 75, pp. 162–174, 2013.

[44] D. W. Dees, V. S. Battaglia, and A. Bélanger, "Electrochemical modeling of lithium polymer batteries," *Journal of power sources*, vol. 110, no. 2, pp. 310–320, 2002.

[45] R. Jackey, M. Saginaw, P. Sanghvi, J. Gazzarri, T. Huria, and M. Ceraolo, "Battery model parameter estimation using a layered technique: an example using a lithium iron phosphate cell," tech. rep., SAE Technical Paper, 2013.

[46] D. Rakhmatov, S. Vrudhula, and D. A. Wallach, "A model for battery lifetime analysis for organizing applications on a pocket computer," *IEEE Transactions on Very Large Scale Integration (VLSI) Systems*, vol. 11, no. 6, pp. 1019–1030, 2003.

[47] M. Nikdel *et al.*, "Various battery models for various simulation studies and applications," *Renewable and Sustainable Energy Reviews*, vol. 32, pp. 477–485, 2014.

[48] H. Zhang and M.-Y. Chow, "Comprehensive dynamic battery modeling for phev applications," in *iEEE PES General Meeting*, pp. 1–6, IEEE, 2010.

[49] C. Lin, Q. Yu, R. Xiong, *et al.*, "A study on the impact of open circuit voltage tests on state of charge estimation for lithium-ion batteries," *Applied Energy*, vol. 205, pp. 892–902, 2017.

[50] T. S. Bryden, B. Dimitrov, G. Hilton, C. P. de León, P. Bugryniec, S. Brown, D. Cumming, and A. Cruden, "Methodology to determine the heat capacity of lithium-ion cells," *Journal of Power Sources*, vol. 395, pp. 369–378, 2018.

[51] H. Rahimi-Eichi, U. Ojha, F. Baronti, and M.-Y. Chow, "Battery management system: An overview of its application in the smart grid and electric vehicles," *IEEE Industrial Electronics Magazine*, vol. 7, no. 2, pp. 4–16, 2013.

[52] F. Yang, D. Wang, Y. Zhao, K.-L. Tsui, and S. J. Bae, "A study of the relationship between coulombic efficiency and capacity degradation of commercial lithium-ion batteries," *Energy*, vol. 145, pp. 486–495, 2018.

[53] Q. Wang, X. Zhao, J. Ye, Q. Sun, P. Ping, and J. Sun, "Thermal response of lithium-ion battery during charging and discharging under adiabatic conditions," *Journal of Thermal Analysis and Calorimetry*, vol. 124, no. 1, pp. 417–428, 2016.

[54] X. Zhang, "Thermal analysis of a cylindrical lithium-ion battery," *Electrochimica Acta*, vol. 56, no. 3, pp. 1246–1255, 2011.

[55] C. Zhang, K. Li, and J. Deng, "Real-time estimation of battery internal temperature based on a simplified thermoelectric model," *Journal of Power Sources*, vol. 302, pp. 146–154, 2016.

[56] S.-C. Chen, Y.-Y. Wang, and C.-C. Wan, "Thermal analysis of spirally wound lithium batteries," *Journal of the Electrochemical Society*, vol. 153, no. 4, p. A637, 2006.

[57] K. Onda, T. Ohshima, M. Nakayama, K. Fukuda, and T. Araki, "Thermal behavior of small lithium-ion battery during rapid charge and discharge cycles," *Journal of Power sources*, vol. 158, no. 1, pp. 535–542, 2006.

[58] C. Forgez, D. V. Do, G. Friedrich, M. Morcrette, and C. Delacourt, "Thermal modeling of a cylindrical lifepo4/graphite lithium-ion battery," *Journal of Power Sources*, vol. 195, no. 9, pp. 2961–2968, 2010.